

See discussions, stats, and author profiles for this publication at: <https://www.researchgate.net/publication/225297730>

Recent Advances in the Use of TiO₂ Nanotube and Nanowire Arrays for Oxidative Photoelectrochemistry

ARTICLE *in* THE JOURNAL OF PHYSICAL CHEMISTRY C · APRIL 2009

Impact Factor: 4.77 · DOI: 10.1021/jp809385x

CITATIONS

490

READS

439

10 AUTHORS, INCLUDING:



Karthik Shankar

University of Alberta

84 PUBLICATIONS 9,863 CITATIONS

SEE PROFILE



James Ian Basham

National Institute of Standards and Techn...

17 PUBLICATIONS 1,037 CITATIONS

SEE PROFILE



Nageh K. Allam

Massachusetts Institute of Technology

96 PUBLICATIONS 1,760 CITATIONS

SEE PROFILE



Oomman Varghese

University of Houston

103 PUBLICATIONS 17,819 CITATIONS

SEE PROFILE

REVIEW ARTICLE

Recent Advances in the Use of TiO₂ Nanotube and Nanowire Arrays for Oxidative Photoelectrochemistry

Karthik Shankar,[†] James I. Basham,[†] Nageh K. Allam,[†] Oomman K. Varghese,[†] Gopal K. Mor,[†] Xinjian Feng,[†] Maggie Paulose,[†] Jason A. Seabold,[‡] Kyoung-Shin Choi,[‡] and Craig A. Grimes^{*,†}

Department of Electrical Engineering, and Materials Research Institute, 217 Materials Research Laboratory, The Pennsylvania State University, University Park, Pennsylvania, 16802, and Department of Chemistry, Purdue University, West Lafayette, Indiana 47907

Received: October 23, 2008; Revised Manuscript Received: December 31, 2008

In this article, we present recent advances that we have achieved toward improving the properties of anodically formed semiconducting TiO₂ nanotubes as well as nanowire arrays as electrodes for oxidative photoelectrochemistry. The morphology, crystallinity, composition, and illumination geometry of nanotube or nanowire arrays are critical factors in their performance as photoelectrodes. We discuss the key aspects relating to each factor and the advances achieved in improving each. With respect to the more fully investigated nanotube arrays, the ability to control the morphological parameters such as pore size, tube length, and wall thickness of the nanotube architecture has enabled high performance in applications such as water photoelectrolysis, photocatalysis, dye-sensitized solar cells, and heterojunction TiO₂–polymer hybrid solar cells. We begin by reviewing the photoelectrochemical performance of state-of-the-art nanotube arrays fabricated on planar substrates. We then present more recent results related to the growth of TiO₂ nanotube arrays on nonplanar substrates designed in such a way that reflected light normally lost to free space is instead directed to a different point on the device, in turn improving overall photoconversion efficiency. Insofar as the crystallinity of the nanotubes is concerned, the use of a high-temperature oxygen or air-ambient anneal to crystallize the nanotube arrays is disadvantageous, since it results in a thick barrier layer where recombination losses occur and also because it precludes compatibility with polymeric substrates. In this regard, we discovered a two-step fabrication process for synthesis of crystallized nanotube arrays at low-temperatures. The photoelectrochemical applications of TiO₂ are limited by its large electronic band gap. We briefly review the cationic and anionic doping approaches popularly used to modify the TiO₂ band gap. We consider the use of ternary oxide systems containing titania as both a structural support and corrosion-inhibitor, in particular fabrication and performance of n-type Ti–Fe–O nanotubes and p-type copper-rich Cu–Ti–O nanotubes, with a note on our recent synthesis of iron oxide nanotube arrays by anodic oxidation of iron. Fabrication and photoelectrochemical properties of CdS–TiO₂ and CdTe–TiO₂ nanotube array heterojunction photoelectrodes are discussed. The article concludes by examining low temperature synthesis, and resulting properties, of single crystal vertically oriented TiO₂ nanowire arrays on transparent conductive glass substrates; preliminary investigation of these nanowire array photoelectrodes for water photolysis reveals them to have low series resistance and provide excellent separation of photogenerated charges.

1. Introduction

During the past decade the reduction in size of functional architectures has been a dominating trend in many fields of science and technology. Structural size reduction down to the nanometer scale leads not only to a miniaturization of functional units but also to the development of new materials and systems with unique physical and chemical properties. The large oxidizing power of photogenerated holes in titania coupled with the low cost and relative physical and chemical stability of TiO₂

render it the semiconductor material of choice for many applications that exploit solar energy. These applications include dye-sensitized solar cells where sunlight is converted into electricity, water photoelectrolysis where solar energy is converted into a chemical fuel (hydrogen), photocatalytic conversion of CO₂ to hydrocarbon fuels, and as a photocatalyst where organic pollutants are degraded into more environmentally friendly chemical species. All of these applications require TiO₂ to be in contact with a solid, liquid, or gaseous electrolyte, consequently TiO₂ is a prime candidate for the development of nanoscale architectures. For optimal performance of TiO₂ in these aforementioned applications, a suitable architecture is one that is characterized by a large internal surface area, good electrical transport, low charge carrier recombination losses and

* To whom correspondence should be addressed. E-mail: cgrimes@engr.psu.edu.

[†] The Pennsylvania State University.

[‡] Purdue University.

Karthik Shankar received a bachelors of technology in metallurgical engineering and materials science in 2000 from the Indian Institute of Technology, Chennai, where he was the recipient of the prestigious Governor's Gold Medal for all-round excellence. Karthik Shankar was one of only 12 nationwide Eastman Kodak Research Fellows in 2003. He received his Ph.D. in electrical engineering in 2007 at Penn State University and is currently a Research Associate at the Penn State's Materials Research Institute. His present research focuses on application-specific growth of nanotubes and nanowires with precisely tailored morphological features, with an emphasis on the understanding and modeling of their growth mechanism.

James Basham received his B.S. in Applied Physics from Rensselaer Polytechnic Institute in 2007. He is now an Electrical Engineering Ph.D. student in Dr. Grimes' research group. His research interests include design and fabrication of liquid junction and solid state dye-sensitized solar cells.

Nageh K. Allam obtained his B.Sc. in Chemistry (1998) and M.Sc. in Electrochemistry of Materials (2003) both from Cairo University, Egypt. In 2005 he received a postgraduate fellowship from Ford Foundation to pursue his Ph.D. in Materials Science and Engineering at The Pennsylvania State University in the Grimes' research group. His current research is focused on the synthesis of efficient, environmentally benign materials for the solar generation of hydrogen by water photoelectrolysis.

Oomman K. Varghese received his Ph.D. Degree in Physics from Indian Institute of Technology (I.I.T.) Delhi, India in 2001. He is presently working as Chief Scientist at Sentech Corporation, Boalsburg PA, and as Visiting Scientist at Materials Research Institute, The Pennsylvania State University. His fields of interest are environmental sensing, dye sensitized solar cells, bulk heterojunction solar cells, photocatalytic conversion of carbon dioxide to hydrocarbons and water photoelectrolysis. His responsibilities include the development of high quality transparent titania nanotube arrays on FTO glass.

Gopal K. Mor received his Ph.D. (2002) in Physics from the Indian Institute of Technology Delhi, India. He then joined the Pennsylvania State University as Postdoctoral Scholar, becoming a Research Associate in 2008. His research interests include solar cells, photogeneration of H_2 and O_2 gases, electrochemical anodic oxidation process of valve materials, and gas sensors.

Xinjian Feng received his Ph.D. degree (2006) in chemistry from Institute of Chemistry, CAS, China, and then went to Department of Materials Science and Engineering, Fridrich-Alexander University, Germany as a Humboldt Fellow (2007). He is currently a research scholar at the Materials Research Institute of The Pennsylvania State University. His scientific interests are focused on synthesizing and assembling one-dimensional semiconducting materials using top-down (electrochemical anodization) and bottom-up (hydrothermal or solvothermal) routes, understanding their structure induced special surface/interfacial properties, as well as their applications in solar energy conversion.

Maggie Paulose received her Masters degrees in Physics from Cochin University of Science and Technology, Kerala, India in 1995 and in Solid State Materials from Indian Institute of Technology (I.I.T.) Delhi, India in 1996. She is currently a Research Associate at Materials Research Institute, The Pennsylvania State University. She is primarily responsible for the development of high quality transparent titania nanotube arrays on FTO glass and titania nanotube array flow-through membranes. Her fields of interest are dye-sensitized solar cells, bulk heterojunction solar cells, photocatalytic conversion of carbon dioxide to hydrocarbons, gas sensing and water photoelectrolysis.

intimate contact between the semiconductor and the electrolyte. Nanoparticulate electrodes are a commonly used architecture. Nanoparticulate electrodes consist of a several micrometer-thick film consisting of a random three-dimensional network of interconnected 15–20 nm particles. While these electrodes possess a high surface to volume ratio, the structural disorder at the contact between two crystalline particles leads to an enhanced scattering of free electrons, thus reducing the electron mobility.¹ Vertically oriented self-organized nanotube arrays formed by electrochemical anodization² constitute a competing architecture that is currently generating great interest due to the orthogonalization of charge separation and charge transport that is intrinsic to their structure.³ The nanotube array architecture, a depiction of which is shown in Figure 1, being ordered and strongly interconnected, eliminates randomization of the grain

Jason A. Seabold received his B.S. degree in Chemistry in 2006 from Bowling Green State University. He is currently a graduate student at Purdue University working in Prof. Kyoung-Shin Choi's laboratory. His research involves electrochemical synthesis and characterization of semiconductor electrodes and catalysts for use in photoelectrochemical cells.

Kyoung-Shin Choi is an Associate Professor at Purdue University in the Department of Chemistry. She received her B.S. degree (1993) and M.S. degree (1995) from Seoul National University, and obtained a Ph.D. degree (2000) at Michigan State University. She then spent two years at the University of California, Santa Barbara as a postdoctoral researcher, and joined the chemistry faculty at Purdue University as an assistant professor in 2002. Her current research interests include composition and morphology control of inorganic materials and polycrystalline electrodes for use in electrochemical and photoelectrochemical applications. She was a recipient of a 2006 Alfred P. Sloan Research Fellowship and the 2007 ExxonMobil Faculty Fellowship in Solid-State Chemistry.

Craig A. Grimes is a Professor of Electrical Engineering, and Materials Science and Engineering, at the Pennsylvania State University (University Park, PA). He received a Ph.D. degree from the University of Texas at Austin in 1990. His research interests include the solar production of hydrogen by water photoelectrolysis, photocatalytic reduction of CO_2 to hydrocarbon fuels, organic as well as inorganic heterojunction solar cells, propagation and control of electromagnetic energy, and remote query environmental sensors. He is co-author of *Light, Water, Hydrogen: The Solar Generation of Hydrogen by Water Photoelectrolysis* (Springer).

network and increases contact points for good electrical connection. Charge carrier recombination has been demonstrated to be significantly lower in dye-sensitized TiO_2 nanotube array based solar cells,^{4–6} where efficiencies greater than 6% have been achieved. The nanotube architecture has a large internal surface area and can be easily filled with liquid thus enabling intimate contact with electrolyte. Additionally, the morphological parameters of the architecture can be precisely controlled.^{7,8} Uniform titania nanotube arrays of various pore sizes (22 to 110 nm), lengths (200 nm to 1000 μm),⁹ and wall thicknesses (7 to 34 nm) are easily grown by tailoring the electrochemical conditions. The porosity of the ordered structure allows the incident photons to be more effectively absorbed than on a flat electrode,¹⁰ with anisotropic optical scattering occurring when the pore displacement period and the light wavelength have comparable values.¹¹ The porosity of anodically formed nanoporous titania has been used to fabricate electrochromic cells with a diffuse reflectance of 60%.¹² Polarized Micro-Raman spectroscopic measurements on the cross section of free-standing NT membranes reveal significant enhancement of the Raman intensity when the polarization of the incident laser beam is parallel to the nanotube axis, indicating an "antenna" effect attributed to the enhanced light scattering along the cylindrical nanotube structure.¹³ In another study, directional random lasing was demonstrated in a porous alumina membrane filled with hybrid polymer nanowires and TiO_2 nanoparticles.¹⁴

In 1991 Zwilling and co-workers¹⁵ reported the porous surface of titania films electrochemically formed in fluorinated electrolyte by titanium anodization. A decade later Grimes and co-workers² first reported formation of uniform titania nanotube arrays via anodic oxidation of titanium in an HF electrolyte. Over the last eight years, our group has been working to fabricate nanostructured semiconductor architectures,^{2,7,16–20} model their optical properties,^{21,22} and develop their applications in the fields of gas sensing,^{23–25} solar cells,^{6,26–29} photochemical hydrogen production,³⁰ self-cleaning photocatalysts,³¹ biomedical implants,³² drug delivery,^{33,34} and recently photocatalytic reduction of CO_2 to hydrocarbon fuels. Speaking generally, we have pursued the design, synthesis, and characterization of semiconducting metal oxide nanotube arrays that can be integrated into practical devices.

This article reviews the work which has mainly been developed in our laboratory and with collaborators on the use of TiO_2 based

semiconducting oxide nanotube arrays as photoanodes in oxidative photoelectrochemistry. Primary attention is given to recent developments on the use of visible light responsive ternary metal oxide nanotube arrays, heterojunctions formed by combining large band gap TiO_2 nanotubes with a narrow band gap semiconductor such as CdTe , and use of nonplanar illumination geometries to improve the absorption of near-band-edge photons. We shall also consider prospects of the next generation of nanotube-array based photoelectrochemical devices.

2. Brief Survey of Efforts to Narrow the Titania Band-Gap by Compositional Doping

The geometry of the high surface area titania nanotube arrays, grown vertically from a substrate, appears ideal for water photolysis allowing facile electrolyte percolation and efficient charge transfer.³⁵ Under band gap illumination by ultraviolet light, TiO_2 nanotube arrays exhibit quantum yields exceeding 80% for water photolysis.³⁰ However, the widespread technological use of titania is impaired by its wide band gap (3.2 eV), which requires ultraviolet irradiation for photocatalytic activation. Because UV light accounts for only a small fraction ($\approx 5\%$) of the sun's energy compared to visible light (45%), any shift in the optical response of titania from the UV to the visible spectral range will have a positive impact on the photocatalytic and photoelectrochemical utility of the material. Modifying the band structure of titania to make it more responsive to visible wavelengths has been an enduring effort, with mixed results. External sensitizers such as organic dyes and polymers have been successfully employed to increase photoconversion efficiencies in photovoltaic cells.³⁶ However, the sensitizers may detach from the TiO_2 surface in aqueous media and these organic sensitizers degrade in corrosive and highly oxidizing environments. For applications such as photoelectrochemical water splitting and photocatalytic degradation of organic compounds, where the photoelectrode is subject to prolonged exposure to an aqueous medium, the external sensitizer approach is not feasible. Historically, compositional doping of the titania has been the approach taken for bandgap engineering of the material. When employing dopants to change the optical response of a material, it is desirable to maintain the integrity of the host material crystal structure while changing its electronic structure. The crystal structure of the material is directly related to the ratio of cation and anion size in the crystal lattice. It appears to be relatively easier to replace Ti^{4+} in titania with any cation than to substitute O^{2-} with any other anion due to the difference in the charge states and ionic radii. Cationic doping of TiO_2 with transition metals such as V and Cr has been extensively studied.^{37–39} While several authors have reported that transition metal ion doping decreases the phototreshold energy of TiO_2 , there is also an increase in thermal instability and a decrease in carrier lifetimes,^{40,41} which limits overall conversion efficiencies.

Asahi et al.'s report⁴² in 2001 of visible light photocatalysis in nitrogen doped TiO_2 incited a surge of interest in anionic doping of TiO_2 . This approach consists of substitution of a nonmetal atom such as nitrogen,^{43–45} carbon,^{46,47} and fluorine⁴⁸ for oxygen. The large number of reports on the effect of anionic doping in TiO_2 differ greatly in the methods used to introduce the dopant, which run the gamut from chemical methods such as sol–gel reaction synthesis,⁴⁹ electrochemical doping⁵⁰ and oxidation of titanium nitride⁵¹ to physical methods such as magnetron cosputtering^{52,53} and ion implantation.⁵⁴ Despite this obvious heterogeneity in method of synthesis, the reports can be broadly classified into those that use anionically doped TiO_2 as free-standing photocatalysts and others which quantify the photoelectrochemical response of an-

ionically doped TiO_2 . Presently, the question of whether anionic doping by nitrogen and/or carbon achieves band gap narrowing in TiO_2 , the extent of any such narrowing, and the utility of the resultant materials, is a matter of much debate in the scientific literature. A large part of the existing literature agrees that anionic doping produces enhancement in the visible activity of free-standing TiO_2 photocatalysts. On the other hand, insofar as the photoelectrochemical response of anionically doped TiO_2 is concerned, the improvement of the visible photocurrent response is at best modest in the bulk of these reports.^{50,53,55,56} Several reports on anionically doped TiO_2 have used extrapolation of diffuse reflectance measurements to demonstrate improved visible response. There are two problems with this technique. First, the widely used practice of determining the band gap of the coating directly from the diffuse reflectance provides only qualitative information about the optical response of the material at visible wavelengths, while quantitative determination of the band gap requires a more detailed calculation involving the thickness, refractive index and surface roughness of the coating, which is typically not attempted in these reports.⁵⁷ Second, use of the diffuse reflectance technique assumes that all light absorbed is attributable solely to electronic transitions between the valence band and the conduction band, an assumption that is often inaccurate. A more reliable method to demonstrate and quantify the visible response consists of measuring the incident photon-to-electron conversion efficiency (IPCE) at different wavelengths by collection of the photocurrent action spectrum of the doped material. The IPCE method has the significant advantage that absorption due to transitions not related to the band gap, such as the d–d transitions that occur in transition-metal-doped oxides, are ignored. We have previously reported carbon incorporation by flame annealing in anodically formed titania nanotube-arrays where we noted the absence of a clear threshold in both the IPCE and the optical absorption spectrum, suggesting the creation of impurity levels by carbon doping deep into the gap rather than a modification of the band gap itself. It has been recently pointed out by Murphy⁵⁸ that in several reports of carbon doped TiO_2 the actual photocurrent values are grossly inconsistent with the IPCE data and that measured visible activity in carbon-doped titania was most likely attributable to oxygen vacancies,⁵⁹ especially when the said carbon doping was performed in a reducing atmosphere. Hoffman and co-workers⁶⁰ found the oxidative power of nitrogen-doped TiO_2 photocatalysts under visible illumination to be close to zero. Hashimoto et al.⁶¹ found that regardless of the stoichiometric amount of nitrogen in N-doped titania the quantum yield values from irradiating with visible light were lower than with UV light. This suggested the formation of an isolated narrow band above the valence band responsible for the visible light response in nitrogen doped TiO_2 . The UV light quantum yields were lowered with increasing nitrogen concentration, indicating that the doping sites could also serve as recombination sites. Batzill et al.⁶² found no evidence of band gap narrowing in nitrogen doped anatase or rutile while Serpone⁶³ has argued that the absorption spectra of nitrogen- and carbon doped TiO_2 in the visible spectral region originate from the formation of oxygen vacancies and the advent of color centers in the doped TiO_2 rather than from any narrowing of the band gap.

In sections 6 and 7 of this feature article, we discuss our results with a strategy different from both conventional cationic doping and anionic doping to improve the visible light response of the ordered nanoarchitectures. Our strategy consists of identifying semiconducting metal oxides with band-gaps smaller than titania whose processing is compatible with TiO_2 . Presently, we have focused on our attention on $\alpha\text{-Fe}_2\text{O}_3$ and copper oxides (CuO and Cu_2O). We formed ternary oxide (Cu-Ti-O and

Fe–Ti–O) nanotube array architectures by depositing cosputtered films of the appropriate metal composition (Cu–Ti and Ti–Fe) on conductive glass substrates, subsequently anodizing them in fluoride ion containing media. In these architectures TiO_2 confers both structural support and chemical stability to the narrow band gap oxide material. We have found that it is not necessary for the two oxides to form a homogeneous solid solution of one in the other; even when the two oxide phases are segregated, the ternary oxide nanotube architecture shows good photoelectrochemical response in the visible, likely due to the lower recombination resulting from the fast capture of photogenerated charge carriers by close-lying solution ions.

3. Characterization Methodology

All subsequent discussions related to improvements in the morphology, illumination geometry, crystallinity, and composition of TiO_2 nanotube arrays as well as photoelectrochemical activity tests share a common characterization methodology which is outlined in this section.

3.1. Morphological and Structural Characterization. The morphologies of all anodized samples were examined using a JEOL JSM-6300 field emission scanning electron microscope (FESEM). In certain instances where more detailed information regarding morphology and/or crystal structure were required, high-resolution transmission electron microscopy (HRTEM) was performed using a JEOL 2010F instrument. Samples were prepared for TEM by scraping the substrate with the tip of a pair of tweezers. Material was allowed to fall onto a copper grid with a lacey carbon film. The crystalline phases were detected and identified by a glancing angle X-ray diffractometer (GAXRD) on a Philips X'pert MRD PRO X-ray diffractometer (Almelo, The Netherlands) as well as TEM. Compositional information was obtained by performing X-ray photoelectron spectroscopy on nanotube array films using a Kratos Axis Ultra spectrometer with an Al anode (Al KR: 1486.6 eV). The anode voltage and current were 14 keV and 20 mA, respectively. Photoelectrons were collected in hybrid mode over an analysis area of about 1.5 mm^2 , with the plane of the sample surface normal to the analyzer entrance. Spectra were charge referenced to C 1s at 285 eV. Optical transmittance measurements of transparent nanotube array films were performed using a Cary UV–vis spectrophotometer.

3.2. Measurement of Photoelectrochemical Properties. Photoelectrochemical properties of the nanotube arrays were investigated using a three-electrode configuration, with the TiO_2 nanotube array photoanode as a working electrode, saturated Ag/AgCl as a reference electrode, and platinum foil as a counter electrode. The samples were mounted on a glass base, and the electrical contacts were taken from the titanium substrate using copper leads and silver epoxy after removing the oxide layer at the titanium surface. All the regions except a 1 cm^2 sample were covered using an insulating epoxy. A 1.0 M KOH solution was used as the electrolyte. A scanning potentiostat (CH Instruments, model CHI 600B) was used to measure dark and illuminated currents at a scan rate of 10–20 mV/s. For measurements performed under ultraviolet illumination, a 50 W metal halide lamp (Exfo Lite) was used as the light source, with optical filters used to restrict the incident light to UV wavelengths between 320 and 400 nm. The incident power was determined as 100 mW cm^{-2} using a thermopile detector (Spectra Physics, CA, USA) after eliminating the light reflection and absorption effects at the Pyrex glass window. For measurements performed under white light illumination, simulated sunlight (AM-1.5G) was used produced by a 500 W Oriel Solar Simulator equipped with AM 1.5 filters whose

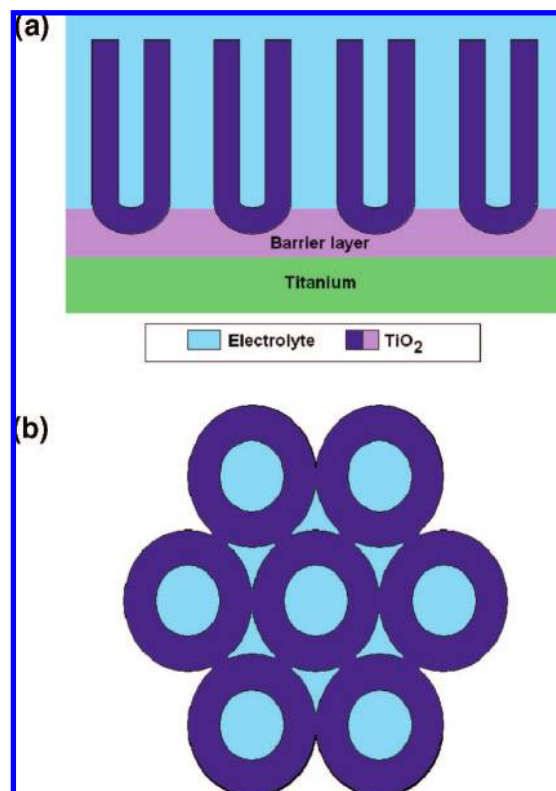


Figure 1. Depiction of the vertically oriented TiO_2 nanotube array architecture showing: (a) cross-section and (b) top-view. Reprinted with permission.³⁵

output was measured using an NREL calibrated standard Silicon solar cell. Figure 2a illustrates the three compartment experimental setup for water photoelectrolysis measurements, with a close up photo of an illuminated nanotube array photoanode from which oxygen is evolved. Figure 2b shows the actual realization of this experimental setup. Incident photon to current conversion efficiency (IPCE) measurements were performed with the spectral irradiance of the light from the 300 W xenon lamp, integrated with a parabolic reflector, passing through an AM 1.5 filter and monochromator determined using an Oriel calibrated silicon photodiode. Hydrogen generation experiments were done at constant voltage bias, determined by the peak position in the photoconversion efficiency curve with respect to the Ag/AgCl electrode. The gaseous photo-products were identified and measured by a SRI 8610C gas chromatograph (GC) equipped with a thermal conductivity detector.

3.3. Theory of Efficiency Measurement. Proper determination of light to chemical energy conversion efficiency of a photoelectrochemical cell is critical in evaluating its performance. In practical photoelectrolysis cells, the photovoltage (at zero current this is termed the open circuit voltage V_{oc}) between the electrodes supplies only a part of the free energy for water splitting. When short circuited under dark condition (no illumination), the Fermi levels of the semiconductor photoelectrode and counter electrode equalize with the redox potential of the electrolyte and the valence band and conduction band are bent up to $E_f - E_{redox}$ where E_f is the Fermi level of the semiconductor and E_{redox} is the potential of the redox couples in the solution.^{64,65} The barrier height represents the upper limit of the open circuit voltage that can be achieved under irradiance. Upon irradiation, say in the case of n-type semiconductors, the conduction band population of electrons increases and the Fermi level shifts up reducing the conduction band bending. The difference between the electrochemical potential of electrons in the semiconductor (Fermi level) and the chemical potential

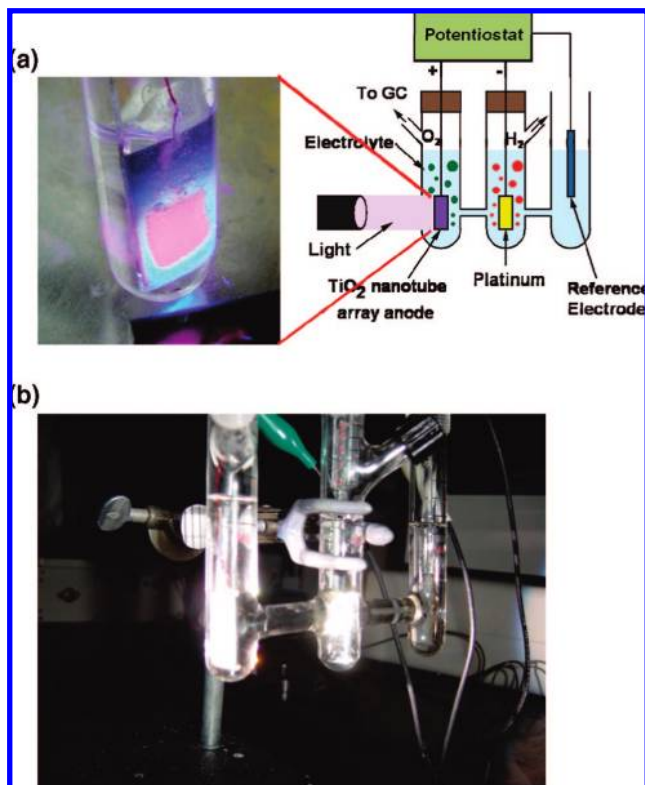


Figure 2. Water-photoelectrolysis system using TiO₂ nanotube array photoanode. (a) Depiction with close-up photo of an illuminated nanotube array photoanode. Reprinted with permission.³⁵ (b) Photo of water-photoelectrolysis under operation.

of electrons in the solution (the redox potential) gives the open circuit voltage V_{oc} . V_{oc} cannot exceed $|E_f - E_{vb}|$ for photoanodes where E_{vb} is the valence band energy. Therefore, the open circuit potential can never be as high as the band gap potential because of the inherent losses due to the entropy change. Hence, higher band gap materials are useful for water splitting as these can supply higher V_{oc} hence the possibility of water splitting without supplying any additional electrical or chemical energy. However, the higher band gap materials cannot effectively utilize solar energy. Therein of course lies the challenge. In practical cases, V_{oc} values up to about 0.9 V are common. The overall efficiency of the cell is reduced when an external electrical bias is applied as discussed later in this section.

The photoconversion efficiency (solar conversion efficiency if sunlight is used) in practical cells is estimated as⁶⁶

$$\varepsilon_0 = \frac{\Delta G^0 R_{H_2}}{P_t} \quad (1)$$

where R_{H_2} is the rate of production (mol/s) of hydrogen in its standard state per unit area of the photoelectrode, ΔG^0 is the standard Gibbs energy = 237.2 kJ/mol at 25 °C and 1 bar, and P_t is the power density (W/m²) of illumination. The numerator and denominator have units of power; hence, the photoconversion efficiency is the ratio of the maximum power output to the power input. Equation 1 is based on the assumption that the free energy ΔG^0 can be completely retrieved in an ideal fuel cell run by the products from the photoelectrolysis cell for which the relation is applied. Instead of the free energy ΔG^0 , the enthalpy (heat) of water splitting ΔH^0 has also been used assuming that the heat of water splitting is completely retrieved

by burning hydrogen.^{67–69} At 25 °C and 1 bar, $\Delta H^0 = 285$ kJ/mol. However, the thermodynamic definition of “efficiency” involves work, and hence, it is appropriate to use ΔG^0 . Using ΔH gives exaggerated values for efficiency.

If I_p is the current density responsible for the generation of hydrogen at the rate of R_{H_2} in eq 1, then under 100% Faradaic conversion (that is, all of the carriers are utilized only for generating hydrogen/oxygen), $R_{H_2} = I_p/nF$, where n , which is the number of moles of electrons used for generating 1 mol of hydrogen, is 2 and F , the Faraday constant, is 96 485 C. Therefore, the voltage corresponding to the Gibbs energy is $V_{rev} = \Delta G^0/nF = 1.229$ V.

$$\varepsilon_0 = \frac{1.229 I_p}{P_t} \quad (2)$$

where the constant is expressed in volts (1.229 V), I_p in A/m², and P_t in W/m².

Spontaneous water splitting upon illumination requires semiconductors with an appropriate band gap, electron affinity, and flat band conditions. The flat band positions shift with pH of the electrolyte. In some cases, the work function of the counter electrode (usually metal) has a value unfavorable for the effective charge transfer from/to the electrolyte species. Hence in many cases an external bias, either electrical or chemical, needs to be applied between the electrodes to effect water splitting. This external bias contribution needs to be subtracted from eq 1, or (1) and (2), to obtain the overall photoconversion efficiency. In the case of an external electrical bias, the efficiency can be defined as

$$\varepsilon_0(\text{efficiency}) = \frac{\text{energy stored as hydrogen} - \text{energy input from power supply}}{\text{light energy input}} \quad (3)$$

$$\varepsilon_0 = \frac{\Delta G^0 R_{H_2} - V_{\text{bias}} I_p}{P_t} \quad (3a)$$

which simplifies to

$$\varepsilon_0 = \frac{(1.229 - V_{\text{bias}}) I_p}{P_t} \quad (3b)$$

As mentioned in the case of relation (2) the constant is expressed in volts and all other parameters are in SI units. The basis of this definition is that a fuel cell run by the products of the photoelectrolysis cell supplies a part of its output to the photoelectrolysis cell as electrical bias.^{70,71} The combined system must have a significant positive energy output to be considered useful.

3.4. Two-Electrode vs Three Electrode Measurements for Efficiency Calculations. Practical photoelectrolysis cells consist of two electrolyte immersed electrodes with the bias voltage applied between the working and counter electrodes;⁷² the overall chemical reaction in such a cell is made of two independent half reactions. To understand the chemical changes at the photoelectrode, in laboratory water photoelectrolysis experiments a three-electrode geometry is used to measure photocurrent. This geometry involves a working electrode (photocathode or photoanode), a counter electrode that is

generally platinum and a reference electrode. The internationally accepted primary reference is the standard hydrogen electrode (SHE) or normal hydrogen electrode (NHE) which has all components at unit activity $[\text{Pt}/\text{H}_2 (a = 1)/\text{H}^+ (a = 1, \text{aqueous})]$. However, using such an electrode is impractical and hence other reference electrodes such as silver–silver chloride ($\text{Ag}/\text{AgCl}/\text{KCl}$) and saturated calomel electrodes (SCE) ($\text{Hg}/\text{Hg}_2\text{Cl}_2/\text{KCl}$) are generally used. Their potentials may then be converted in terms of NHE potential. The potential of an Ag/AgCl electrode is 0.197 V vs NHE and that of saturated calomel electrode is 0.242 V vs NHE.⁷³

Equations 3a and 3b give a thermodynamical measure of efficiency and should be applied, in general, to all cases involving an electrical bias irrespective of the two or three electrode configuration used. Note that in the case of a three-electrode configuration V_{bias} should be measured between the working and counter electrodes.⁷⁴ The reference electrode in the three-electrode geometry does not draw any current and the current flows between the working and counter electrodes. In contrast, several different expressions and methodologies have been used by research groups to find the efficiency,^{75–77} making a direct comparison of reported efficiency values meaningless. We now consider some of these different approaches.

One approach to find efficiency uses the electrical power saved due to the use of light in a photoelectrolysis process compared to an electrolysis process using light-insensitive electrodes⁷⁸

$$\varepsilon_0 = \frac{P_{\text{saved}}}{P_t} = \frac{V_{\text{saved}} I_p}{P_t} \quad (4)$$

The method involves recording the current from a semiconductor photoelectrode (anode or cathode) at various applied potentials and then repeating the experiment by replacing this semiconductor electrode with a metal electrode like platinum. The power saved P_{saved} for a particular current density I , is $V_{\text{saved}} I$ where V_{saved} is the difference between the corresponding voltages for semiconductor and metal cathode. The power saving is maximum when both electrodes operate at a current density (I_{max}) and a voltage corresponding to the maximum power conversion point in the photoelectrolysis process.

Equation 4 assumes the use of a highly catalytic electrode with zero overpotential losses at the electrode or solution–electrode interface, hence highly catalytic metal electrodes with low overpotential losses are required for comparison. V_{saved} is a key parameter in determining efficiency. If a metal with a lower electrocatalytic activity is used, say for example gold, the overpotential losses will be higher and hence a greater negative bias will be required than that needed for a (highly catalytic) platinum electrode. In which case V_{saved} will be higher, and hence, a higher efficiency would be obtained although the increase is not due to qualities of the semiconductor electrode.

An approach similar to this avoids the use of a comparative noble metal electrode and neglects overpotential losses at the electrodes. In this method, the potential applied at the hydrogen (or oxygen) electrode (in a three-electrode configuration) is compared with the potential generated at an ideal fuel cell anode (or cathode). In the case of an n-type semiconductor photoanode

or

$$\varepsilon_0 = \frac{(V_{\text{app}} - V_{\text{H}_2}^0) I_p}{P_t} \quad (5b)$$

(hydrogen evolution using photocathodes)

V_{ox}^0 and $V_{\text{H}_2}^0$ represent, respectively, the standard potentials of oxygen and hydrogen electrodes. V_{ox}^0 takes a value of +0.401 V vs NHE in alkaline electrolytes (pH 14) and +1.229 V vs NHE in acidic electrolytes (pH 0). The corresponding values of $V_{\text{H}_2}^0$ are –0.828 V vs NHE and 0 V vs NHE.

Another form of this definition has sparked much debate in the scientific community.^{57,75,79–83} In this approach V_{app} (or V_{bias}) is taken as the absolute value of the difference between the potential at the working electrode measured with respect to a reference electrode (V_{meas}) and the potential of the photoelectrode under open circuit conditions measured with respect to the same reference electrode in identical conditions (in the same electrolyte solution and under the same illumination). In the case of a semiconductor photoanode where oxygen evolution takes place the efficiency is calculated as

$$\varepsilon_0 = \frac{(V_{\text{rev}}^0 - |V_{\text{app}}|) I_p}{P_t} = \frac{(V_{\text{rev}}^0 - |V_{\text{meas}} - V_{\text{aoc}}|) I_p}{P_t} \quad (6)$$

$V_{\text{rev}}^0 = 1.229$ V is the standard state reversible potential for the water splitting reaction and V_{aoc} is the anode potential measured with respect to the reference electrode at open circuit conditions. The term $V_{\text{meas}} - V_{\text{aoc}}$ arises from the fact that V_{oc} (the open circuit voltage of the cell which may be obtained from V_{aoc}) represents the contribution of light toward the minimum voltage needed for water splitting potential (1.229 V) and that the anode potential measured with respect to the reference electrode V_{meas} has contributions from the open circuit potential and the bias potential applied by the potentiostat (i.e., $V_{\text{meas}} = V_{\text{app}} + V_{\text{aoc}}$). The term $V_{\text{meas}} - V_{\text{aoc}}$ makes relation (6) independent of the electrolyte pH and the type of reference electrode used. Thus the use V_{rev}^0 in relation (6) instead of V_{ox}^0 or $V_{\text{H}_2}^0$ as in the case of relations (5a) or (5b) is justified. Although this approach has received wide attention and is commonly being used, it is suggested that the relation (6) may give exaggerated photoconversion efficiency values. In any case (two or three electrode) the voltage measured between the working and the counter electrodes gives the actual applied bias voltage V_{app} [or V_{bias} in eqs 3a and 3b]. This voltage multiplied by the cell current gives the electrical energy supplied by the electrical power supply. But in practice, where a potentiostat is used to apply an external bias to the photoelectrode, this actual voltage V_{app} (between the working and counter electrodes) may slightly exceed the bias voltage measured as $V_{\text{app}} = V_{\text{meas}} - V_{\text{aoc}}$ with respect to the reference electrode.⁸⁴ Thus the use of the latter term in relation (6) can show a higher efficiency value than when the term V_{app} , measured between the counter and working electrodes, is directly used as in the case of relations (3a) and (3b).

3.5. Quantum Yield Measurement. Steady-state wavelength-specific photocurrents were measured for the nanotube arrays in a two-electrode arrangement at different applied voltages. Incident photon-to-current efficiencies (IPCE) are calculated using the following equation:

$$\varepsilon_0 = \frac{(V_{\text{ox}}^0 - V_{\text{app}}) I_p}{P_t} \quad (5a)$$

(oxygen evolution using photoanodes)

$$\text{IPCE} = \frac{(1240 \text{ eV} \cdot \text{nm})(\text{photocurrent density } \mu\text{A}/\text{cm}^2)}{(\lambda \text{ nm})(\text{irradiance } \mu\text{W}/\text{cm}^2)} \quad (7)$$

Dividing the IPCE by the fraction of incident photons absorbed at each wavelength gives the absorbed photon-to-current efficiency (APCE).⁸⁵ Various factors including nanotube length and composition factor into APCE calculation through the absorbance A , as shown below

$$\text{APCE} = \frac{\text{IPCE}}{1 - 10^{-A}} \quad (8)$$

4. Photochemical Water-Splitting Efficiencies of TiO₂ Nanotube Arrays: Planar Geometries

The titania nanotube array architecture results in a large effective surface area in close proximity with the electrolyte thus enabling diffusive transport of photogenerated holes to oxidizable species in the electrolyte. Minority carriers generated within a “retrieval” length from the material surface, that is a distance from the surface equal to the sum of the depletion layer width and the diffusion length, escape recombination and reach the electrolyte.⁸⁶ The relevant structure sizes of the titania nanotube arrays, i.e., half the wall thickness, are all smaller than 20 nm which is less than the retrieval length of crystalline titania;⁸⁷ hence, bulk recombination is greatly reduced and the quantum yield enhanced.⁸⁷

The morphology of 6 μm long nanotube arrays, 580 $^{\circ}\text{C}$ annealed, is shown in Figures 3 and 4; under UV (320–400 nm, 100 mW/cm²) illumination a photoconversion efficiency of about 12.25% was obtained as shown in Figure 5.³⁰ The photocurrent increases with increasing annealing temperature, attributable to the increased crystallinity of the nanotube-walls with the reduction of the amorphous regions and grain boundaries in turn reducing the number of charge carrier recombination centers, to 675 $^{\circ}\text{C}$, after which it reduces with samples annealed at 700 $^{\circ}\text{C}$ showing a low photocurrent ($\sim 10^{-4}$ A) due to disruption of the nanotube-array architecture. At temperatures near 675 $^{\circ}\text{C}$, the densification of the bottom part of the nanotubes starts isolating the undestroyed nanotubes from the metal electrode reducing the number of charge carriers reaching the electrode.

Figure 6 shows the IPCE of 6 μm nanotube-array samples annealed at 600 $^{\circ}\text{C}$. The incident photon-to-current efficiency (quantum efficiency) was calculated using the relation

$$\eta(\lambda) = \frac{hc}{e} \frac{j_p(\lambda)}{I_0 \lambda} \quad (9)$$

where j_p is the photocurrent density, I_0 is the power density of the light and h , c , e , and λ are respectively Planck's constant, speed of light in vacuum, elementary charge, and wavelength of the incident light. The high quantum efficiency clearly indicates that the incident light is effectively utilized by the nanotube-arrays for charge carrier generation.

Figure 7 shows the hydrogen generated as a function of time (mL), under 320–400 nm illumination, using a 6 μm nanotube array annealed at 600 $^{\circ}\text{C}$. The corresponding hydrogen evolution rate is 76 mL/h \cdot W. The water-splitting reaction was confirmed by the 2:1 ratio of evolved hydrogen to oxygen. Oxygen bubbles evolving from the nanotube-array photoanode do not remain

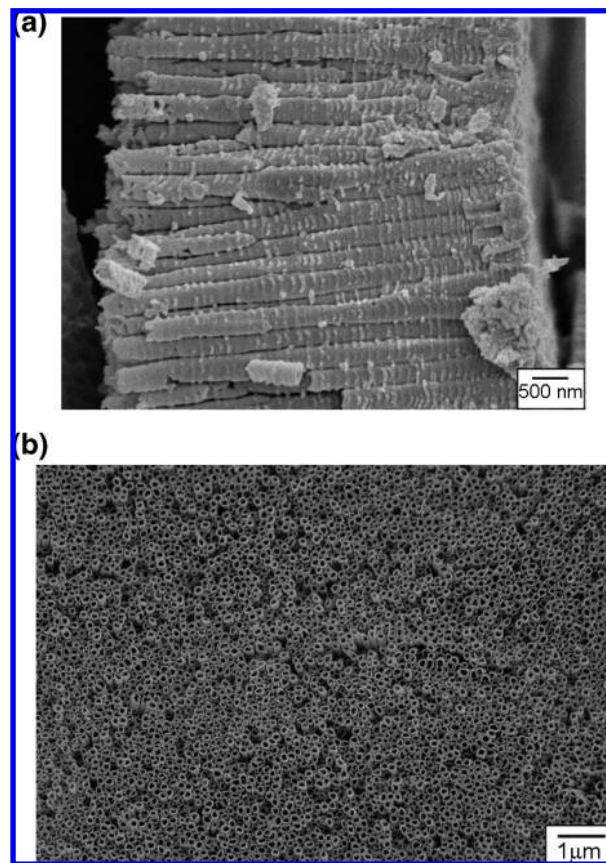


Figure 3. FESEM images of 6 μm nanotube arrays showing: (a) Cross-section and (b) top-view. Reprinted with permission.³⁰

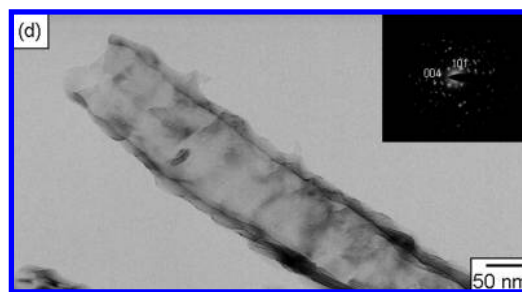


Figure 4. TEM image and diffraction pattern of a single 6 μm nanotube array annealed at 600 $^{\circ}\text{C}$. Reprinted with permission.³⁰

on the sample, hence the output remains stable with time irrespective of the duration of hydrogen production. No degradation has been observed in the samples with exposure to UV/Visible light over a course of a several months.

The roughness factor, i.e., the physical surface area of the film per unit of projected area, measures the internal surface area of the electrode and is of crucial significance in applications such as sensing and catalysis. Assuming an idealized nanotubular structure shown in Figure 8a with inner diameter D , wall thickness W , and tube length L , the purely geometric roughness factor is calculated as^{4,27}

$$1 + \left[\frac{4\pi L(D + W)}{\sqrt{3}(D + 2W)^2} \right] \quad (10)$$

Equation 10 assumes all surfaces of the nanotubes to be perfectly smooth. In reality, the surfaces are not smooth and the actual roughness factor is higher. Figure 8b is a plot of the

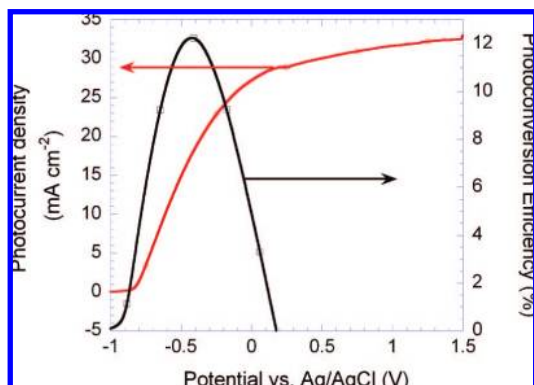


Figure 5. Photocurrent and corresponding photoconversion efficiency generated from 6 μm long nanotube-arrays (in 1 M KOH solution under ultraviolet illumination). Reprinted with permission.³⁰

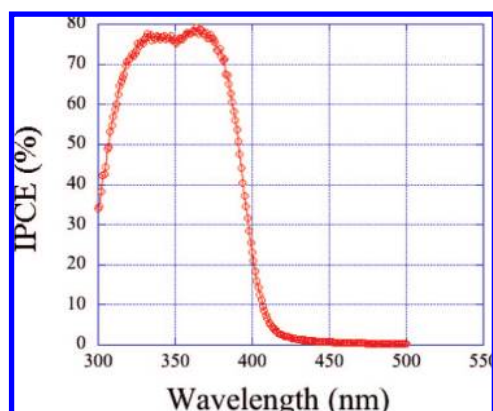


Figure 6. Photoresponse generated from 6 μm long nanotube-arrays subjected to monochromatic illumination at 337 and 365 nm (in 1 M KOH solution). Reprinted with permission.³⁰

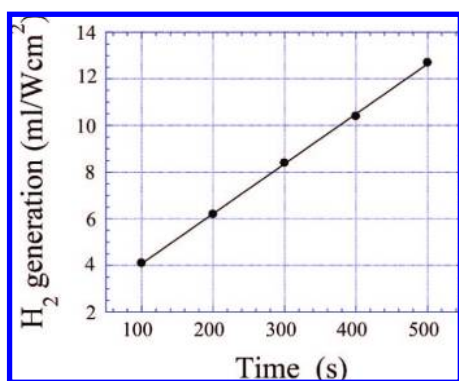


Figure 7. Hydrogen generation as a function of time from 6 μm long nanotube arrays (in 1 M KOH solution under ultraviolet illumination at 100 mW cm⁻²) biased at the point of maximum conversion efficiency. Reprinted with permission.³⁰

calculated geometric roughness factor for nanotubes with three different geometries. The plot shows that higher surface area is more easily obtained with nanotubes of smaller pore size. Although each single nanotube of a smaller pore diameter has a smaller surface area than a nanotube of the same length with a large pore diameter, more of the smaller nanotubes may be packed in an equivalent area. Table 1 displays the roughness factor of nanotubes formed in different electrolytes, determined using dye desorption measurements. The table shows that nanotubes formed in formamide electrolytes have the highest roughness factors per unit length, which also correlates with the high photocurrents and conversion efficiencies obtained with nanotubes formed in this electrolyte.

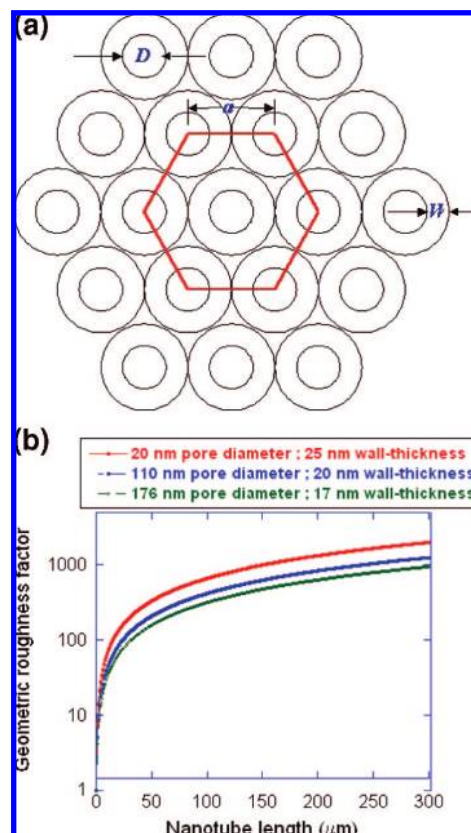


Figure 8. (a) Idealized unit cell of TiO₂ nanotube array with inner diameter D , wall thickness W , and $a = D + W$. (b) Calculated geometric roughness factor as a function of nanotube length. Reprinted with permission.²⁷

Figure 9a shows the measured photocurrent density of nanotube array samples fabricated using a formamide electrolyte, 0.56 g of ammonium fluoride in a solution mixture of 5 mL of deionized water + 95 mL of formamide, at 15 V, 20 V, and 25 V anodization potentials (100 mW/cm², 320–400 nm illumination).²⁷ Prior to photocurrent measurement all samples were annealed at 525 °C for 1 h in oxygen. Figure 9b shows the corresponding photoconversion efficiency of the three nanotube array samples. The use of different anodization voltages resulted in variation of nanotube array length and tube outer diameter: 15 V resulting in a nanotube array 8.2 μm long, 80 nm outer diameter; 20 V resulting in a nanotube array 14.4 μm long, 94 nm outer diameter; 25 V resulting in a nanotube array 16 μm long, 140 nm outer diameter. The 20 V sample, 14.4 μm long 94 nm outer diameter, achieves a photoconversion efficiency of 14.42%. A tradeoff exists between nanotube length and internal surface area. Thus the 15 V nanotubes have a relatively large internal surface area but their optical absorption is limited by their shorter length while the 25 V nanotubes are longer but have less surface area. The maximum conversion efficiency is obtained for nanotubes anodically formed at 20 V. Figure 10a shows the I – V characteristics of 30 μm long 205 nm diameter nanotube arrays fabricated in an electrolyte of 1.2 g of NH₄F in a solution of 5 mL of deionized water + 95 mL of formamide at 35 V. The samples were annealed at 525 and 580 °C for 1 h in oxygen prior to measurement. The 580 °C annealed sample had an open circuit voltage V_{OC} of -0.925 V (vs Ag/AgCl); the 525 °C annealed sample had an open circuit voltage V_{OC} of -0.80 V (vs Ag/AgCl). Figure 10b shows the corresponding photoconversion efficiencies of the two samples. Figure 11a shows the measured photocurrent density of nanotube array

TABLE 1: Nanotube Array Surface Area Determined by Dye Desorption Measurements

electrolyte	anodic potential (V)	inner diameter (nm)	length (μm)	surface dye coverage (nmol cm^{-2})	effective roughness factor	geometric roughness factor
aqueous 0.5% HF	10	22	0.2	5.25	52	38
aqueous 0.5% HF	10–23 (nanocones)		0.4	1.75	17	
aqueous buffered 0.1 M KF (pH~5)	25	110	6.6	50	496	252
0.1 M NH_4F in 1:1 DMF: H_2O	15 porous			30	296	136
0.15 M NH_4F + 5% H_2O in formamide	10	12	3.6	55	546	325
0.15 M NH_4F + 5% H_2O in formamide	15	29	5.4	79	784	390
0.15 M NH_4F + 5% H_2O in formamide	20	70	14.4	181	1797	778
0.22 M NH_4F + 5% H_2O in formamide	35	180	30	277	2750	928
0.27 M NH_4F + 5% H_2O in formamide	20	65	19.6	304	3019	1224
0.3% NH_4F in EG + 1% H_2O	30	45	9	57	566	544
0.3% NH_4F in EG + 1% H_2O	40	70	12	66	655	609
0.3% NH_4F in EG + 1% H_2O	65	135	30	116	1152	1018

samples fabricated in an ethylene glycol electrolyte, 0.25 wt % NH_4F and 1% H_2O at 60 V for 6 h.²⁷ The resulting nanotube array samples were approximately 24 μm in length, with an inner pore diameter of 110 nm and outer diameter of 165 nm. The samples were annealed at 625, 580, and 525 $^{\circ}\text{C}$ for 1 h in oxygen prior to measurement. Figure 11b shows the corresponding photoconversion efficiencies of the two samples.

5. Enhancing Photoconversion Efficiencies by Use of Nonplanar Geometries

5.1. Motivation for the Fabrication of Titania Nanotube Arrays on Curved Surfaces. Limiting optical losses is an important issue for enhancing the efficiency of photovoltaic devices. Significant improvements in device performance can be achieved if the fraction of incident light that is reflected is minimized. In conventional solar cells, in addition to the use

of antireflective coatings on the surface, texturing of the front and rear of the cell enhances scattering within the active layer of the device, promoting total internal reflection and effectively trapping much of the light inside the cell. By increasing the optical path length of light traveling through the cell, the overall light absorption is significantly enhanced.

Nanotube arrays consisting of tubes longer than 1 μm on titanium foil exhibit strong absorption for wavelengths below 375 nm.²¹ Without altering the band gap of the TiO_2 nanotubes, an intriguing route for increasing efficiency is through engineering some sort of light trapping scheme, whereby the incident light must pass through the sample multiple times before escaping, substantially increasing the probability it is absorbed. This could potentially lead to significant enhancements in light absorption at wavelengths near the band edge (375–400 nm). One approach to this end is to change the geometry of the

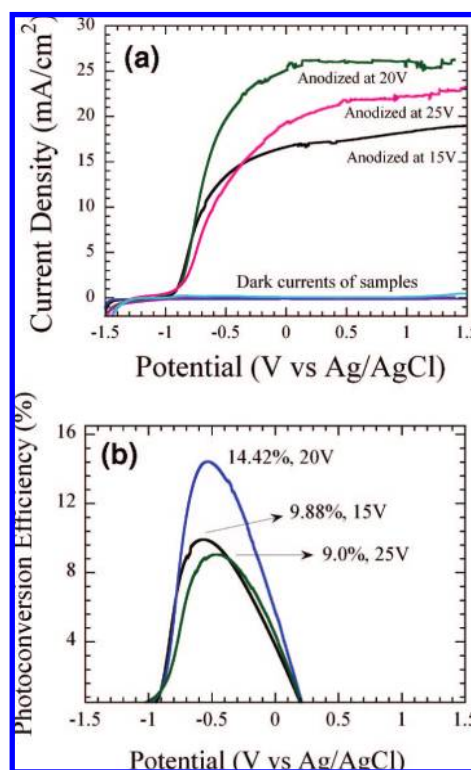


Figure 9. (a) Photocurrent density and (b) corresponding photoconversion efficiency of nanotube array samples fabricated using a formamide electrolyte, our so-called K1 bath of 0.56 g of ammonium fluoride in a solution mixture of 5 mL of deionized water + 95 mL of formamide, at indicated anodization voltages. Prior to photocurrent measurement all samples were annealed at 525 $^{\circ}\text{C}$ for 1 h in oxygen. Reprinted with permission.^{8,27}

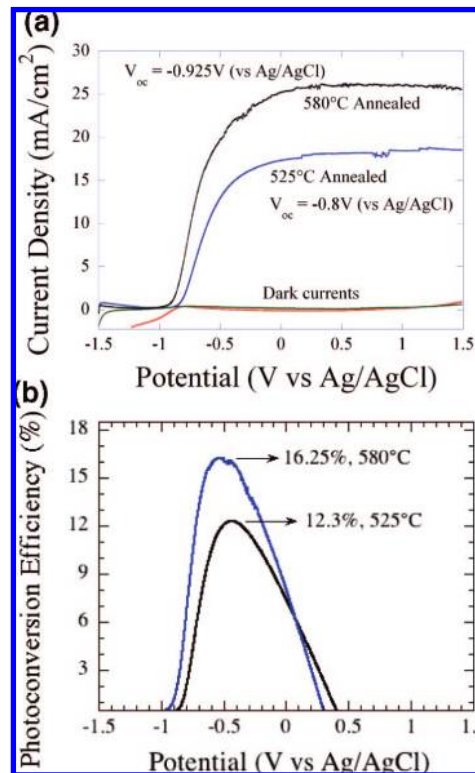


Figure 10. (a) Photocurrent density and (b) corresponding photoconversion efficiency of nanotube array samples fabricated in an electrolyte of 1.2 g of NH_4F in a solution of 5 mL of deionized water + 95 mL of formamide at 35 V. The samples were annealed at indicated temperatures for 1 h in oxygen prior to measurement. The resulting nanotube array samples were 30 μm in length, with an outer diameter of 205 nm. Reprinted with permission.^{8,27}

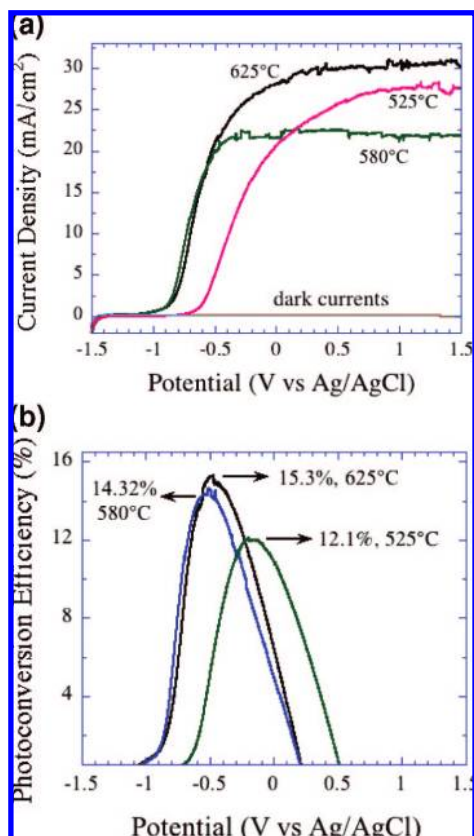


Figure 11. (a) Photocurrent density and (b) corresponding photoconversion efficiency of nanotube array samples fabricated in an ethylene glycol electrolyte, 0.25 wt % NH_4F and 1% H_2O at 60 V for 6 h. The samples were annealed at indicated temperatures for 1 h in oxygen prior to measurement. The resulting nanotube array samples were approximately 24 μm in length, with an inner pore diameter of 110 nm and outer diameter of 160 nm. Reprinted with permission.^{8,27}

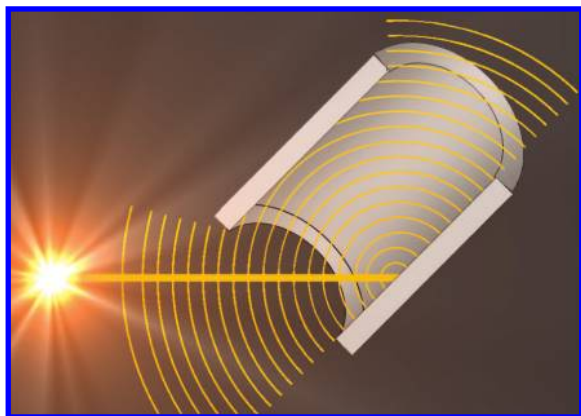


Figure 12. Illustrative drawing showing the principle of using pipe geometry to capture reflected light which would otherwise be lost from a planar surface.

starting titanium material. As illustrated in Figure 12, by restricting the solid angle through which light can be reflected from the surface and leave the device one can imagine that a certain fraction of the reflected light will fall upon another area of the device instead of being lost to free space, and be available again for electron–hole generation. Herein we present methods for trapping reflected light, thereby increasing efficiency, through the use of nonplanar substrate geometries including a macroscopic sized tube (hereafter referred to as a pipe) and a half cylinder (or half pipe). In the case of full pipes, by tilting the axis of the pipe at a 45° angle relative to the incident light one

can ensure multiple internal specular reflections. Only a small fraction of the diffusely reflected light will escape the pipe, while all of the specularly reflected light can, in principle, be recycled. The half pipe is designed as a midway point between a pipe and foil. For the half pipe, a much smaller fraction of the reflected light will fall upon the surface of the sample. For truly diffuse reflected light, depending upon the height of the sample, somewhere near 25–30% of the light can potentially be reabsorbed. For specularly reflected light, if one assumes the incident light is parallel, then roughly 50% will again strike the surface of the sample following the initial reflection.

5.2. Fabrication of Titania Nanotube Arrays on Nonplanar Substrates. The fabrication of TiO_2 nanotube arrays in a potassium fluoride (KF) based electrolyte has been described in detail elsewhere.⁸⁸ Briefly, we prepared a solution containing KF (0.1 M), sodium hydrogen sulfate (1 M), trisodium citrate (0.2 M), and sodium hydroxide (Aldrich, Milwaukee, WI). The sodium hydroxide was added dropwise to adjust solution pH to 4. Three sets of titanium pipes with inner diameters of 1.5, 3.75, and 5.5 mm were used. The anodizations were carried out at an applied bias of 25 V relative to a counter platinum electrode for a duration of 17 h after which they were promptly rinsed and sonicated in deionized water to remove surface debris and residual electrolyte. Fabrication of 6 μm nanotubes in pH 5.0 KF electrolytes leads to the formation of considerable amounts of debris on the surface of the tubes. For a planar geometry, this debris can readily be removed by ultrasonication for a few seconds in water. In the case of pipes, however, the cylindrical geometry effectively shields the inner surface, preventing it from being sufficiently cleaned. For this reason we chose to lower the pH of the electrolyte to 4.0 to prevent any appreciable formation of precipitate at the expense of reducing the length of the resulting nanotubes to 1.4 μm . The nanotubes were crystallized by oxygen anneal at 550 °C for 4 h. Unused areas of the device, back side of the half pipe and the entire outer surface of the full pipe, were masked with nonconductive epoxy.

There are several factors which complicate the nanotube synthesis on nonplanar titanium. It is well-known that in the case of KF based solutions, self-heating during the anodization process can result in the formation of a nanoporous film rather than a nanotube array. If the anodization process begins with the pipes being immersed in the electrolyte at 25 V relative to the counter Platinum electrode, as is typically done, the resultant structure was nanoporous rather than nanotubular in nature. This is believed to be a result of the large initial current generating a large amount of heat in the inner region of the pipe, which, due to potentially limited flow of the electrolyte in and out of the pipe, particularly for larger aspect ratio pipes, was insufficiently dissipated. A continuous oxide fails to form and current levels stay high, exacerbating the heating problem. In order to grow nanotubes the anodization process was modified in the following manner. First, a constant current of 20 mA per cm² was applied until the voltage differential reached 25 V (a process that takes 2–3 min). The source was switched to constant voltage mode, and the subsequent anodization was performed at a constant 25 V.

5.3. Characterization of Nanotube Arrays Formed on Nonplanar Substrates. The main geometrical factor that can influence the overall light scattering and hence absorption is the aspect ratio of the pipe. In order to probe the effect of the aspect ratio on the photoconversion efficiency, we anodized a series of pipes having a fixed diameter of 3.75 mm and varied the length from 6.4 to 16.5 mm. The corresponding aspect ratios increased from 1.7 to 4.4, where the aspect ratio will be defined

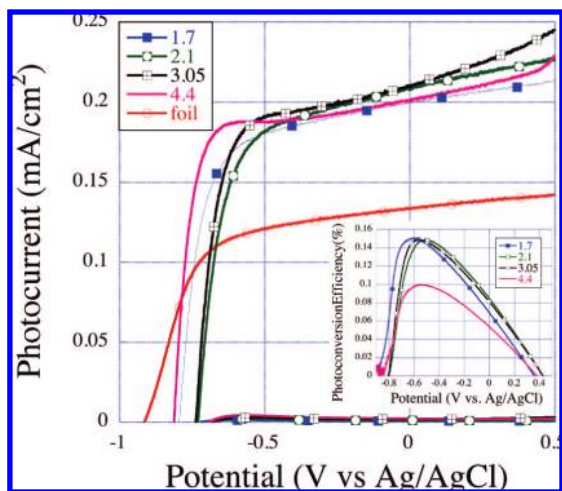


Figure 13. Photo- and dark currents under AM 1.5 illumination for pipes of various aspect ratios coated with TiO₂ nanotubes, and for a flat nanotube array sample. (Inset) Corresponding photoconversion efficiencies.

as the ratio of the length of the pipe to its inner diameter. It should be noted that the minimum aspect ratio of 1.7 was chosen to ensure that all of the specularly reflected light underwent a single reflection prior to exiting the back of the pipe. For this aspect ratio, simple geometric arguments would indicate that the percentage of diffusely scattered light that is recycled after the first scattering event in the full pipe is near 40%. This figure rises to around 55% for the pipe with aspect ratio of 4.4. The specular component of the reflected light continues to travel deeper into the pipe, encountering several reflections before it is either absorbed or exits out of the back opening of the pipe. Due to the roughness of the nanotube array surface the reflected light is expected to be nearly entirely diffuse in nature.

Figure 13 plots the photocurrents as a function of applied bias (vs Ag/AgCl) under AM 1.5 illumination for series of pipes of fixed diameter as well as a planar TiO₂ nanotube array reference sample (denoted as a foil in Figure 13). The calculated photoconversion efficiencies were determined using eq 3b and are given in the inset of Figure 13. There is no change for aspect ratios of 2.1 and 3.05 but a substantial decrease for a pipe of aspect ratio 4.4. This behavior would suggest that the minimum aspect ratio is sufficient to trap most of the light. Further increases in aspect ratio led to poorer performance due to larger dark currents and decreased nanotube quality. It is believed that a high aspect ratio prevents adequate flow of fresh electrolyte to the inside of the pipe during anodization, leading to a poorly defined nanotube array morphology. The best photoconversion efficiency measured for all pipe aspect ratios under AM 1.5 illumination was 0.150%, measured for a pipe of aspect ratio 1.7. This represents a 60% improvement over the efficiency of 0.094% for a flat geometry device. This decrease in conversion efficiency for increased pipe length is not expected, as one would anticipate greater overall absorption as the number of internal reflections is increased. It is worth noting, however, that as the aspect ratio of the nanotubes increases there is a concomitant increase in the dark current. The increase in the dark current can be accounted for by simply considering an increase in sample surface area. If one plots the total dark current for each aspect ratio (Figure 14) then there is a clear trend of increasing dark current with increasing aspect ratio. Further, larger aspect ratio pipes have relatively poorer quality nanotube arrays at their center (Figure 15, panels a and b), likely due to restricted access to fresh electrolyte during anodization. Additionally, no change

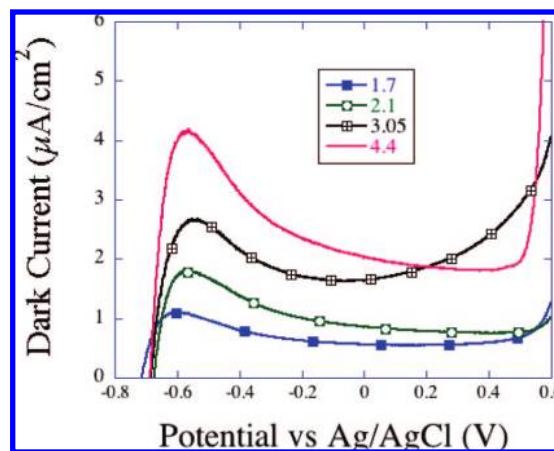


Figure 14. Dark current shown to increase with aspect ratio for four different aspect ratio pipes.

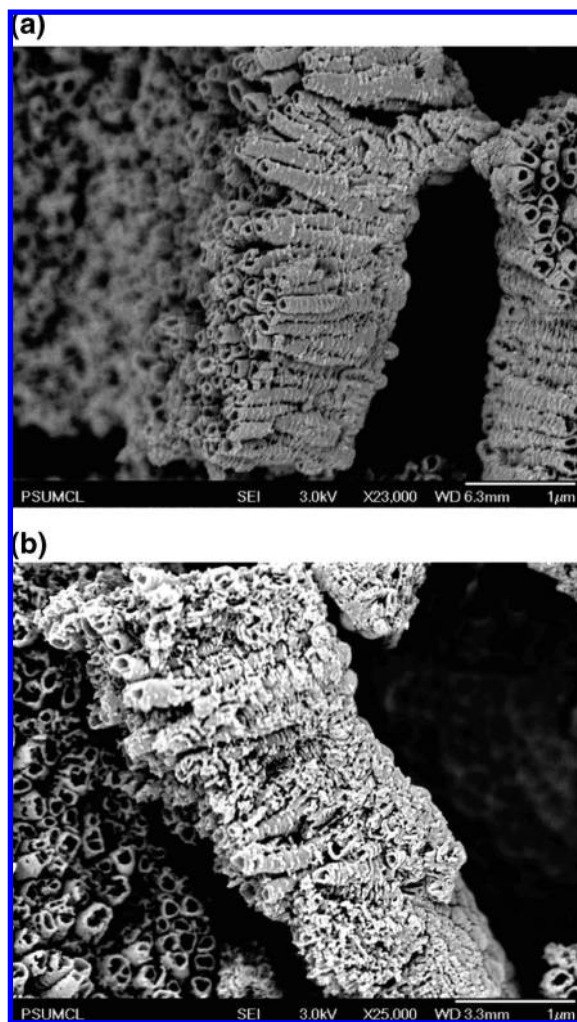


Figure 15. (a) Cross section of a nanotube array taken from the inside of a pipe of aspect ratio 1 and (b) Cross section of a nanotube array taken from the inside of a pipe of aspect ratio 4.

in the photocurrent is observed with an increase in the aspect ratio. This suggests that the amount of light absorption is maximized after a single reflection within the pipe and subsequent increases in aspect ratio simply contribute to a rise in the dark current, thereby lowering the overall photoconversion efficiency.

In the case of anodized half pipes, the underlying titanium acts like a mirror of radius R with the focal point located at a

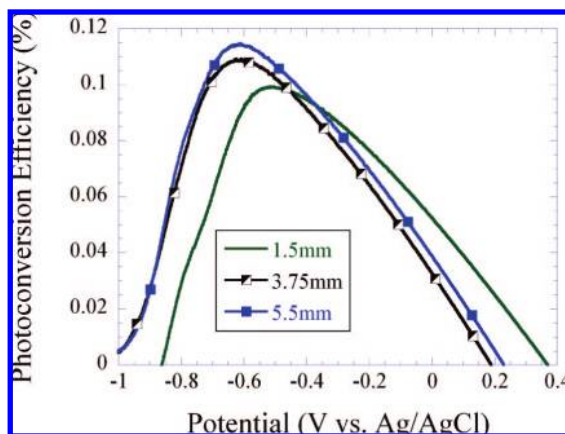


Figure 16. Photoconversion efficiency for half pipes of diameter 1.5–5.5 mm.

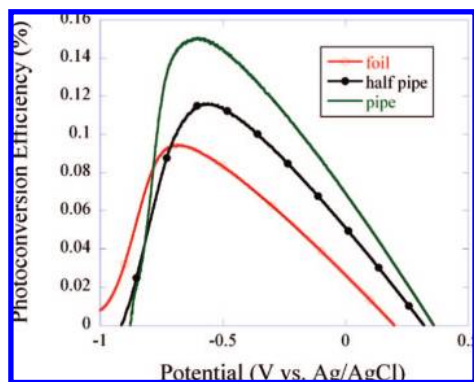


Figure 17. Photocurrent as a function of applied potential for nanotube arrays anodized on a planar foil, a half pipe of 3.75 mm diameter, and a pipe of 3.75 mm diameter and aspect ratio 1.7. Efficiency is seen to increase by 34% over a flat geometry for the half pipe and by 60% for the full pipe.

distance of $R/2$ from the center of the half circle. As a result, approximately 50% of the specularly reflected light is reflected back upon the sample. The finite radius of curvature will cause some of the diffuse reflected light to be recycled. If the aspect ratio for the pipe geometry with maximum efficiency is maintained then, from simple geometrical arguments, the amount of diffuse scattered light that is again incident upon the sample is approximately 30%.

The photo conversion efficiency for half pipes of varying diameters is plotted in Figure 16. It can be seen that the pipe radius has no effect on the overall efficiency of the nanotubes array since the pipe radius does not alter the percentage of diffuse scattered light that is recycled. Increasing the surface area of the half pipe by increasing the radius results in an increase in both the dark and illumination current as all of the surface area is exposed to the incident light and therefore contributes to the photocurrent. It can be seen, however, that the peak efficiency for the half pipe is near 0.126%, which while being greater than that of the planar TiO_2 nanotube array is less than the maximum efficiency of 0.150% achieved for a full pipe of aspect ratio 1.7, suggesting that the capture of the specularly reflected light within the full pipe is indeed beneficial for enhancing the efficiency of the device.

The effect of the geometrical shapes on the overall photo-conversion efficiency for the planar, half pipe, and full pipe of aspect ratio 1.7 are plotted in Figure 17. Both of the alternate geometries show significant enhancements relative to that of the planar nanotube array, as could be anticipated from the total

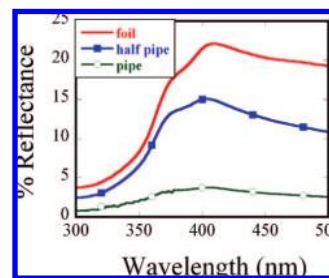


Figure 18. Total reflectance measurements for three geometries. In the case of the pipe only light reflected diffusely out of the near side of the pipe is measured. Light that passes completely through and exits the far side is assumed to be small and not accounted for.

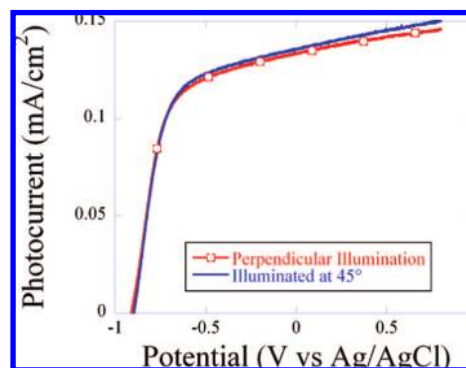


Figure 19. Photocurrent density for a planar geometry nanotube array when illuminated normal to its surface and at a 45° angle to the surface. Current is normalized to account for the fact that effective area of the device is reduced by $1/\sqrt{2}$ when it is angled at 45° .

reflectance measurements shown in Figure 18. To investigate whether the increased absorption is due to the increased optical path length of the nanotube array angled with respect to the incident light, Figure 19 shows the photocurrent of a flat sample under planar illumination and when the sample is tilted 45° relative to the light source. We believe that any gains from an increased optical path length are in this case offset by the fact that a surface which is angled with respect to a light source will reflect more strongly than one which is illuminated along its surface normal. It is possible to grow nanotube arrays on nonplanar surfaces, with tubular geometries offering a 60% increase in efficiency over planar geometries through the recapturing of reflected light that would otherwise be lost.

6. Low-Temperature Crystallization of Titania Nanotubes

The typical TiO_2 nanotube array fabrication sequence forms amorphous nanotubes by anodization followed by an elevated temperatures anneal to induce crystallinity.⁸⁹ Annealing at high temperatures leads to the formation of a thick barrier layer between the tubes and underlying Ti substrate, where recombination losses can occur, which hinders the electron transfer process to the metal electrode (cathode). As discussed by Allam,⁹⁰ low temperature synthetic routes are needed to obtain the full benefits of this unique architecture.⁹¹

6.1. Two-Step Process to Fabricate Crystalline As-Anodized Nanotube Arrays. A schematic of this two-step process is shown in Figure 20.⁹⁰ The first step consists of pretreatment of the Ti foil in H_2O_2 -containing electrolytes, to oxidize the Ti surface, followed by potentiostatic anodization in fluoride-containing media. Two immersion solutions were used (80 $^\circ\text{C}$ for 50–72 h):^{92–94} solution A: 30% H_2O_2 + 5 mM Na_2SO_4 +

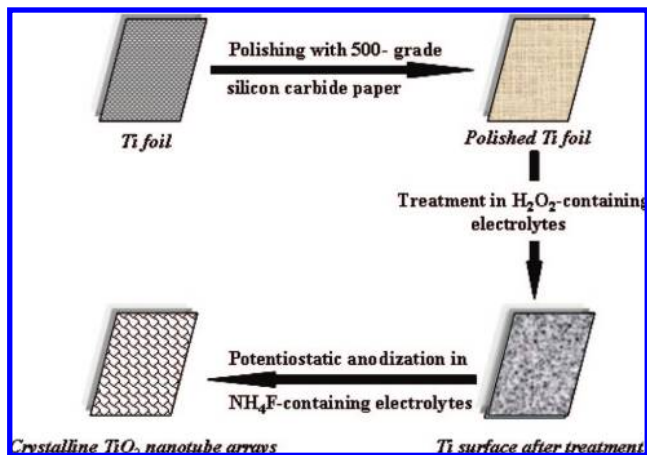


Figure 20. Schematic presentation of the two-step fabrication process used to fabricate crystalline TiO_2 nanotube arrays. Reprinted with permission.⁹⁰

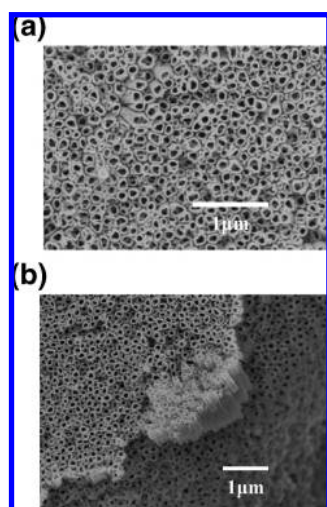


Figure 21. (a) Well-developed nanotube arrays are observed upon anodizing a sample previously treated in solution A in an aqueous electrolyte containing 0.25 M NH_4F + 0.1 M H_3PO_4 + 0.05 M H_2O_2 at 15 V and (b) cross-sectional image of this nanotube array sample. Reprinted with permission.⁹⁰

0.5 M H_3PO_4 ; solution B: 30% H_2O_2 + 5 mM TaCl_5 + 0.5 M H_3PO_4 . Electrolyte NH_4F concentrations ranging from 0.2 to 0.4 M with 0.1 M H_3PO_4 and 0.05 M H_2O_2 were used for anodization of the pretreated films. The as-anodized samples were washed with D.I. water and dried in nitrogen. Steps 1 and 2 of the two-step fabrication process are not symmetrical. Reverse processing, i.e., starting with the fabrication of TiO_2 nanotube arrays via potentiostatic anodization followed by immersion in peroxide containing electrolytes, resulted in destruction of the nanotubular architecture.

6.2. Morphology and Crystallinity of TiO_2 Nanotube Arrays Formed by Two-Step Process. Figure 21 shows FESEM images of a Ti sample previously treated in solution A followed by anodization at 15 V in an aqueous solution containing 0.25 M NH_4F + 0.1 M H_3PO_4 + 0.05 M H_2O_2 . Note that nanotube arrays up to 800 nm can be obtained. Figure 22 shows the GAXRD results for the as-anodized sample shown in Figure 21 indicating that the nanotube arrays are crystallized in pure anatase phase.⁹⁴ Onoda and Yoshikawa reported the fabrication of crystalline porous anatase TiO_2 films via a similar two-step process; annealing of Ti foil at 750–950 °C followed by anodization.⁹⁵ Figure 23a shows a TEM micrograph of the

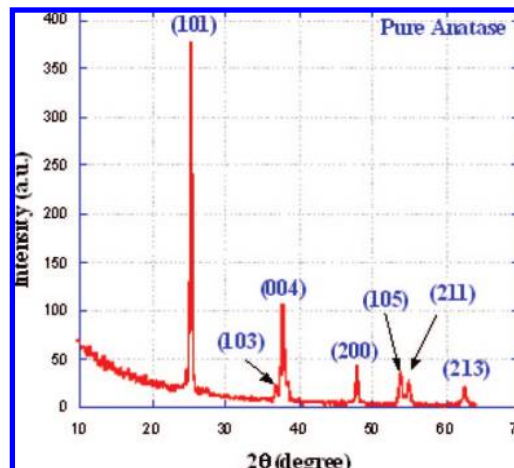


Figure 22. 2° glancing angle X-ray diffraction (GAXRD) pattern of the as-anodized sample shown in Figure 22. Reprinted with permission.⁹⁰

sample indicating the formation of nanotubular architecture. Figure 23b shows the corresponding diffraction pattern which reveals best fit to anatase phase as shown in Figure 23c which gives the intensity from rotationally averaged pattern with expected Bragg lines from anatase.

A sample pretreated in solution B then anodized as above resulted in the formation of TiO_2 nanotube arrays as shown in Figure 24; lengths up to ≈ 900 nm can be obtained. Both GAXRD (Figure 25) and TEM showed the tubes to be crystalline with mixed anatase and rutile phases detected. Figure 26a shows formation of nanotubular structure. Analysis of the TEM diffraction pattern (Figure 26b) and its correlation with the intensity from rotationally averaged pattern with expected Bragg lines (Figure 26c) confirmed the existence of both anatase and rutile.

6.3. Results of Photoelectrochemical Activity Tests for Crystalline As-Anodized Nanotube Arrays. Figure 27 shows measured photocurrent (illuminated less dark) versus voltage characteristics and corresponding photoconversion efficiencies for the TiO_2 nanotube array electrodes under 320–400 nm illumination. The measured photocurrent values for the nanotube arrays composed of a mixture of anatase and rutile are slightly higher than those recorded for pure anatase TiO_2 nanotube architectures. It has been reported that anatase has higher photocatalytic activity than rutile, whereas a mixture of anatase and rutile has higher photocatalytic activity than either anatase or rutile.⁹⁶ The difference in both photocurrent and conversion efficiency between the two samples can be attributed in part to the difference in the relative catalytic activity of their crystalline phases as mentioned above, as well as the difference in nanotube lengths and wall thicknesses (800 and 23 nm for anatase + rutile nanotube arrays and 900 and 18 nm for pure anatase nanotube arrays, respectively). Mor and co-workers reported that the enhanced band bending of the thicker walls decreases surface recombination rates, thus increasing the photocurrent.³

7. Photoelectrochemical Diodes Using Cu–Ti–O Ternary Oxide Nanotube Arrays

7.1. Motivation. CuO is a *p*-type semiconductor with a band gap of 1.2–1.4 eV commonly studied for its photoconductive properties, whereas Cu_2O is a *p*-type semiconductor with a direct band gap of approximately 2.2 eV, which makes it a promising material for the conversion of solar energy.^{18,97,98} CuO and Cu_2O films have traditionally been prepared by thermal oxidation of

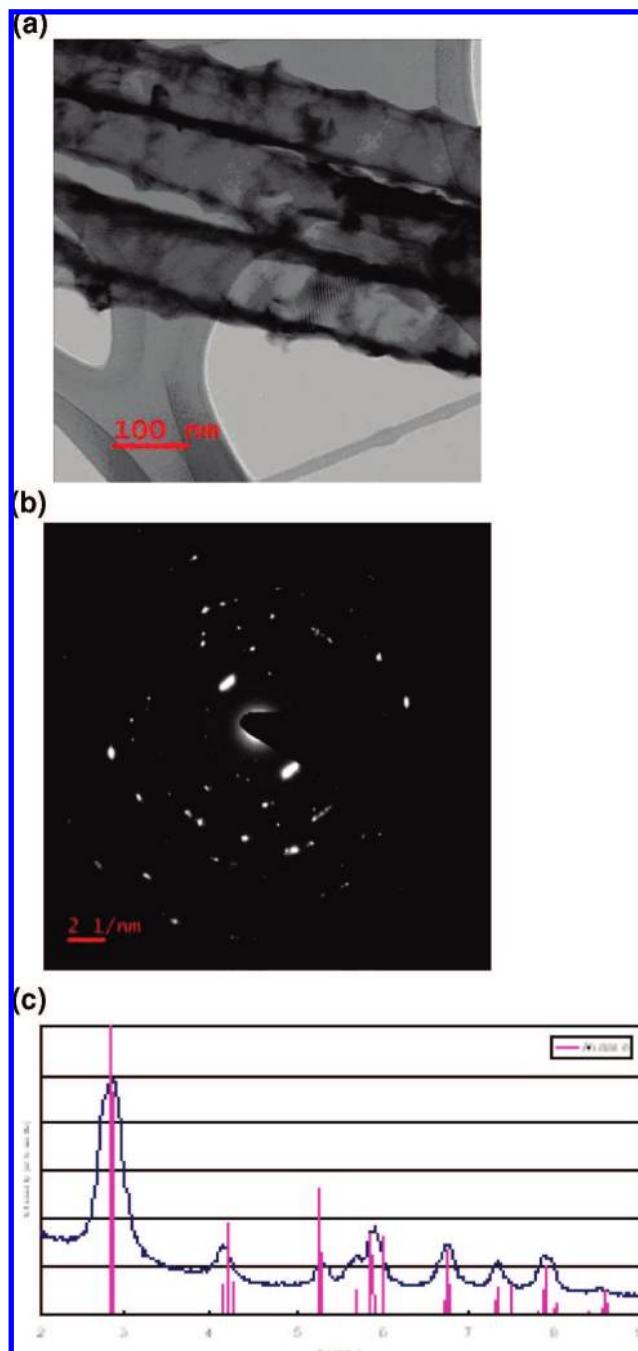


Figure 23. TEM analysis for sample shown in Figure 22: (a) Morphology of the formed architectures, (b) Selected area diffraction pattern from the material and (c) Intensity from rotationally averaged pattern compared with expected Bragg lines from anatase. Reprinted with permission.⁹⁰

copper metal, offering limited control over the resulting material structure.⁹⁹ The abundance of copper and the nontoxicity of copper oxides offer added advantages.¹⁰⁰ While semiconductor materials with bandgaps suitable for capturing a significant fraction of incident solar spectrum energy ($\approx 0.8\text{--}2.4$ eV) typically suffer UV induced photocorrosion,^{101–103} we note that the stability of CuO, Cu₂O, and heterojunctions thereof are significantly altered by the material it is coupled with. For example, Cu₂O heterojunctions with In₂O₃, SnO₂, and ZnO are reported to be unstable while Cu₂O–CdO junctions are relatively stable.^{104,105} Siripala and co-workers reported that depositing a thin layer of TiO₂ on p-type Cu₂O successfully protects the Cu₂O film against photocorrosion,¹⁰⁶ suggesting that TiO₂ may be one

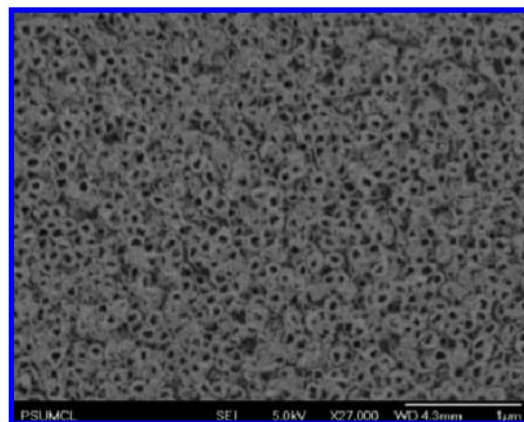


Figure 24. Illustrative FESEM image of a surface achieved upon anodizing the sample that was previously treated in solution B in an aqueous electrolyte containing 0.25 M NH₄F + 0.1 M H₃PO₄ + 0.05 M H₂O₂ at 15V. Reprinted with permission.⁹⁰

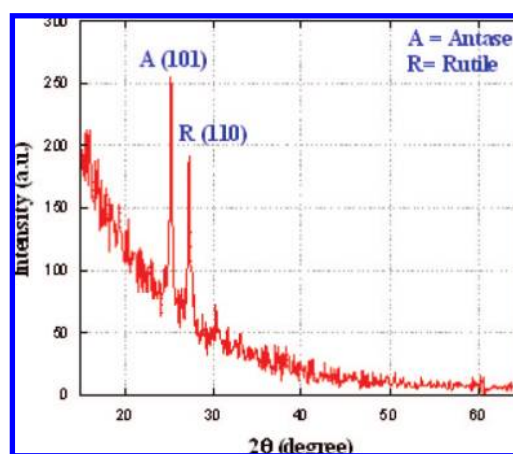


Figure 25. GAXRD pattern of the as-anodized sample shown in Figure 25. Reprinted with permission.⁹⁰

of the best candidates to couple with CuO and/or Cu₂O to enhance photocorrosion stability.

Morphology also affects copper oxide stability, with rapid removal of the photon-generated electrons and holes from the copper oxide significantly improving its stability.^{107,108} Since the properties of nanoarchitected materials are greatly influenced by their shape and dimensional constraints, the synthesis of the copper oxide into ordered one-dimensional (1D) structures such as nanotubes or nanowires could enhance its intrinsic characteristics. Many recent efforts have been directed toward the fabrication of nanostructured CuO to enhance its performance in currently existing applications. To date, well-defined CuO nanostructures with different dimensionalities such as nanoparticles, nanoneedles, nanowires, nanowhiskers, nanoshuttles, nanoleaves, nanorods, nanotubes, and nanoribbons have been obtained successfully by a series of wet chemical routes,^{108,109} electrochemical deposition techniques,¹¹⁰ and vapor-phase processes.¹¹¹ Of these different synthesis techniques, anodic oxidation is distinct in providing a strategy for the top-down growth of self-organized structures with a robust interface to the underlying substrate. As explained in section 4, the vertically oriented n-type TiO₂ nanotube array architecture, achieved by Ti anodization, has been shown to possess large surface area, outstanding charge transfer properties, enhanced light harvesting due to optical scattering and extended electron recombination lifetimes for use in photoelectrochemical cells.^{4,6,27} Despite the excellent light harvesting potential of copper oxide,

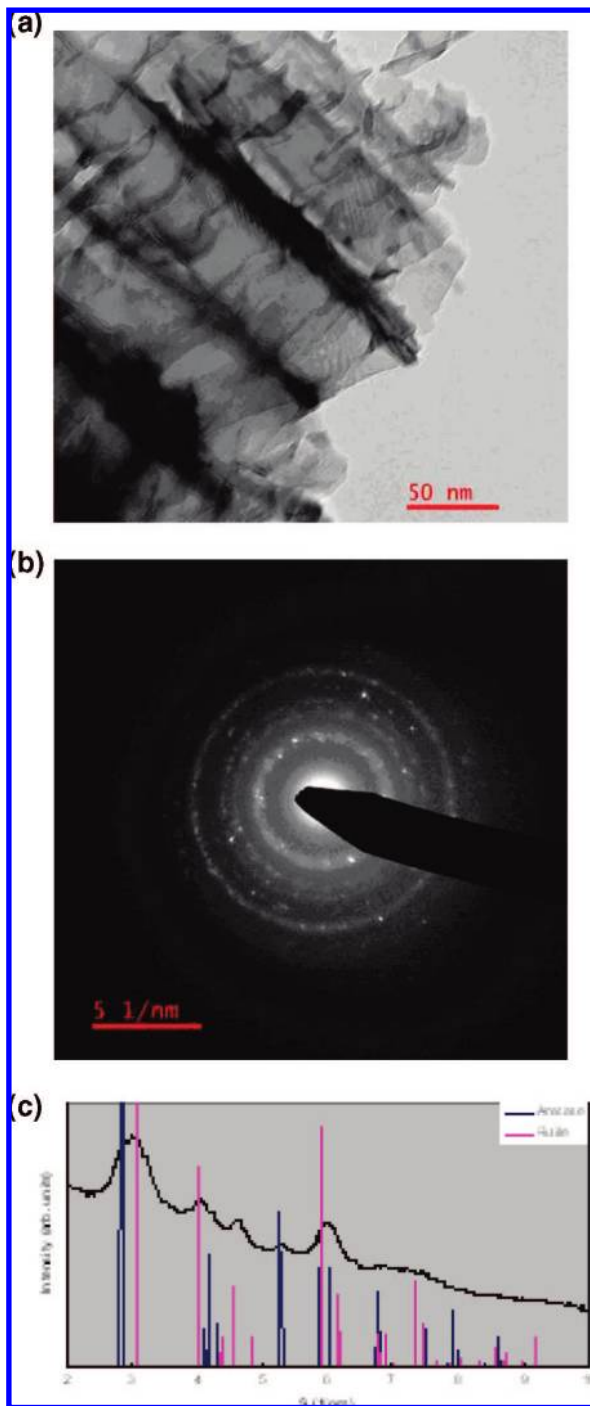


Figure 26. TEM analysis for sample shown in Figure 25 (a) Morphology of the formed architectures, (b) selected area diffraction pattern from the material, and (c) intensity from rotationally averaged pattern compared with expected Bragg lines from anatase and rutile. The material is a mixture of the two phases. Reprinted with permission.⁹⁰

its performance as a photoelectrode for water photoelectrolysis of water is rather poor¹¹² due to the presence of recombination centers in the band gap and its chemical instability. The maximum quantum yields across the entire visible spectrum of CuO based solar photoelectrolyzers is less than 5%¹¹² and that of CuO based undyed regenerative solar cells less than 2%.¹¹³ By incorporating copper oxide inside a TiO₂ nanotube array matrix, we attempted to extend the unique benefits of the nanotube array architecture to the ternary Cu–Ti–O semiconductor system. We reported fabrication of photocorrosion stable

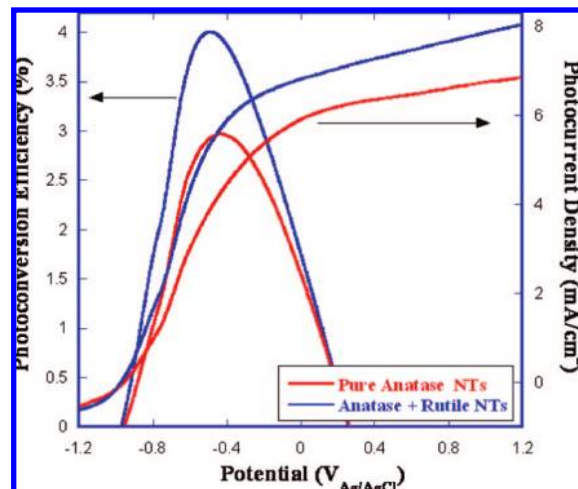


Figure 27. Current–voltage characteristics and photoconversion efficiency for the fabricated crystalline-as-anodized TiO₂ nanotube array photoelectrodes. Reprinted with permission.⁹⁰

p-type Cu–Ti–O nanotube array films by anodization of Cu–Ti films.¹¹⁴ Unlike easily anodized valve metals, the anodization of copper to simultaneously achieve oxidation and with morphological control has proven quite difficult. In this regard, our approach is unique in that we employ Ti as a supporting matrix to provide chemical resistance and mechanical support during the anodic oxidation of copper.

7.2. Fabrication of p-Type Copper Rich Cu–Ti–O Nanotube Arrays. Cu–Ti films of various compositions were deposited by simultaneous cosputtering. Sputtered film thicknesses were determined using a Tencor Profilometer, and the composition by energy dispersive X-ray spectroscopy (Princeton Gamma Tech EDS). The Ti–Cu films were potentiostatically anodized at 30 V in ethylene glycol (anhydrous, 99.8%, Sigma Aldrich) containing 0.25 wt % NH₄F (98% + ACS reagent, Sigma Aldrich) and 1.0 vol % deionized water. The real time variation of the anodization current is similar to that observed for pure Ti films.¹¹⁵ Anodization of the Cu–Ti metal film is stopped just prior to reaching the FTO substrate; hence, in the as-anodized films, a thin discontinuous film of Cu–Ti remains between the Cu–Ti–O nanotube array film and substrate. A summary of film parameters are given in Table 2, with sample numbers denoted by the copper content in the starting metal film.

Crystallization of the as-anodized amorphous Cu–Ti–O films is achieved by annealing. Figure 28 shows the GAXRD spectrum of a sample 60 and sample 74 oxygen annealed at 450 °C for 2 h with a ramp up/down rate of 2 °C/min. The predominant peaks observed in the samples at $2\theta = 36.4^\circ$ and 38.8° correspond to the (111) and (002) reflections of CuO. The residual presence of a Cu₄Ti₃ alloy phase is detected. The formation of Cu–Ti–O films with superior photoelectrochemical properties require a higher degree of crystallization, however two parameters change with annealing, the film crystallization and the resistivity of the 15 Ω/\square FTO layer underlying the Cu–Ti–O films. At elevated temperatures the FTO layer will diffuse into the Cu–Ti–O film, with a corresponding decrease in FTO conductivity, hence optimal sample performance is a tradeoff between crystallization and sheet resistance of the underlying FTO film. Oxygen anneal temperatures greater than 450 °C significantly increase the sheet resistance of the FTO layer, a behavior not as pronounced with vacuum (20 Torr with oxygen background) annealing. Figure 29 shows the GAXRD spectrum of samples 74 annealed in vacuum at 500, 550, and

TABLE 2: Summary of Film Properties Used in Photoelectrochemical Diodes¹¹⁴

sample name	film thickness (nm)	composition (%) determined using EDS	tube length, pore, and wall thickness (nm)	semiconducting behavior of crystallized films	light absorption range
74	1500	74% Cu – 26% Ti	1000, 65, 35	p-type	350–885 nm
60	1000	60% Cu – 40% Ti	850, 65, 35	p-type	350–885 nm
TiO ₂	600	pure Ti	600, 30, 7	n-type	300–400 nm

600 °C. All samples were annealed for 2 h. The predominant peaks observed in the samples at $2\theta = 36.4^\circ$ and 38.8° correspond to the (111) and (002) reflections of CuO.

The samples annealed by both methods do not indicate the formation of Cu₂O. Samples vacuum annealed at 500 and 550 °C show the reflections of Cu₄Ti₃, most likely present in the barrier layer separating the tubes from the FTO substrate; as the annealing temperature is increased to 600 °C oxygen diffuses deeper into the barrier layer converting Cu₄Ti₃ to CuO.

7.3. Photoelectrochemical Properties of p-Type Copper Rich Cu–Ti–O Nanotube Arrays. The optimum band gap of an effective semiconductor for water photoelectrolysis should be in the range of 1.7–2.0 eV, higher than a theoretical minimum water splitting energy of 1.23 eV per photon to compensate for overpotential losses.¹¹⁶ Since the energy needed

to split methanol into H₂ and CO₂ is 0.7 eV,¹¹⁷ and CuO is unstable in aqueous alkaline electrolytes, we initially used a 1:1 water and methanol solution to study the photoelectrochemical properties of the samples. We found that a 5:5:2 methanol:water:diethylamine solution provided the largest photocurrent amplitudes, due to the relatively higher solubility of diethylamine compared to other amines in the methanol–water mixture and increased electron transfer from CuO to the added molecules. Therefore, this solution was used for further study of the photoelectrochemical properties of the Cu–Ti–O films.

Figure 30 shows the global AM 1.5 current versus voltage behavior of a sample 74 annealed in vacuum at 500 °C (2 h) and 550 °C (1 h, 2 h), tested in 5:5:2 methanol/water/DEA solution (pH \approx 8). No significant degradation in the photoreponse of these p–Cu–Ti–O samples was observed in this electrolyte during a continuous 24 h monitoring and under periodic testing over several weeks thereafter. The FTO sheet resistance of the 500 °C annealed sample is 15 Ω/\square . For the 550 °C sample, increasing the anneal duration from 1 to 2 h increased the measured FTO film sheet resistance from 60 Ω/\square to 1.2 k Ω/\square , with a significant drop in the measured photocurrent. For 600 °C vacuum annealed samples the measured sheet resistance is approximately 32 k Ω/\square , with a measured photocurrent of only a few $\mu\text{A}/\text{cm}^2$. Photocathode bias assists in separation of the electron–hole pairs, thereby enhancing photocurrent values. The photocurrent values obtained for this sample in a potential scan are in close agreement with the values obtained by integration of the measured photon flux values ($\mu\text{A}/\text{cm}^2/\text{nm}$) at the three applied bias values of -0.2 , -0.4 , and -0.65 V vs Ag/AgCl, Figure 31. The calculated incident photon to electron conversion efficiency (IPCE) is shown in the inset of Figure 31. For an applied potential of -0.65 V vs Ag/AgCl, we typically see IPCE values of 10–11% in the UV range and 1–7% in the visible range. Thus, the photocurrent action spectra show contribution over the visible light spectrum.

7.4. Self-Biased Heterojunction Photoelectrochemical Diodes. The use of a self-biased pn junction, a so-called photoelectrochemical diode, for solar water-splitting was first reported

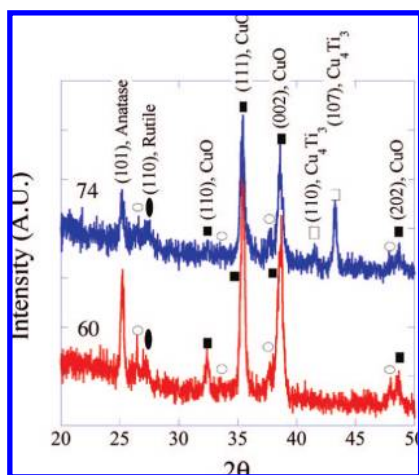


Figure 28. GAXRD patterns of 450 °C, 2 h oxygen annealed Cu–Ti–O samples 60 and 74. The open circles denote SnO₂ peaks. Reprinted with permission.¹¹⁴

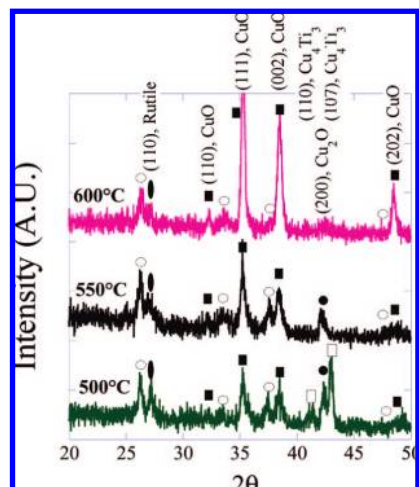


Figure 29. GAXRD patterns of Cu–Ti–O samples 74 vacuum annealed at 500 °C, 550 °C, and 600 °C for two hours. SnO₂ peaks are denoted by open circles. Reprinted with permission.¹¹⁴

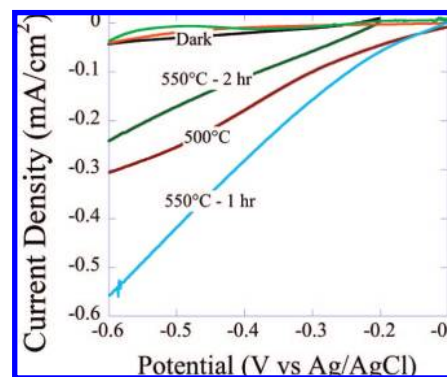


Figure 30. Photocurrent density versus potential for 500 and 550 °C vacuum annealed samples 74 in 5:5:2 methanol:water:diethylamine solution, under dark and global AM 1.5 illumination. Reprinted with permission.¹¹⁴

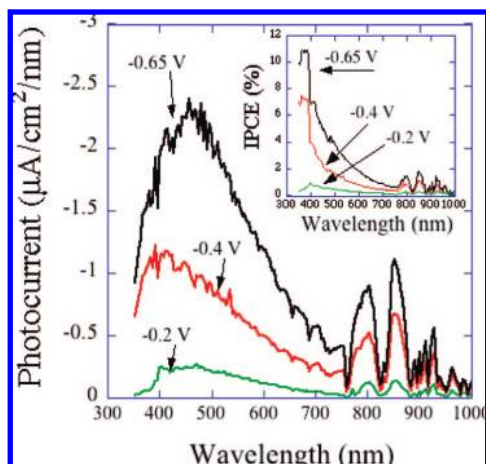


Figure 31. Photoelectron flux dependence of a 550 °C (1 h) vacuum annealed sample 74 at applied bias amplitudes (measured with respect to Ag/AgCl reference electrode) of: -0.2, -0.4, and -0.65 V, tested in a 5:5:2 methanol:water:diethylamine solution under AM 1.5 illumination. Dark currents were nulled before starting the measurements. Inset shows IPCE curves for each applied bias. Reprinted with permission.¹¹⁴

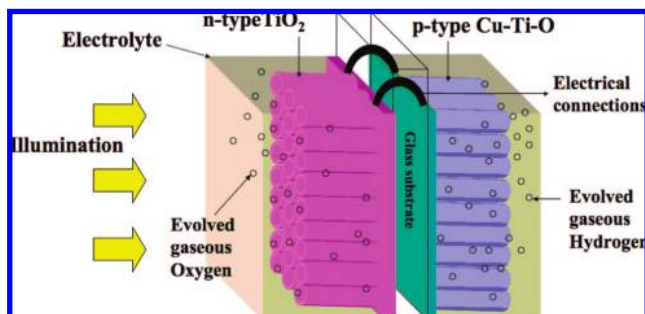


Figure 32. Illustration of photoelectrochemical diode for water splitting comprised of n-type TiO₂ and p-type Cu-Ti-O nanotube array films, with their substrates connected through an ohmic contact. The oxygen evolving TiO₂ side of the diode absorbs UV light, passing the visible light to the hydrogen evolving Cu-Ti-O side. Reprinted with permission.¹¹⁴

by Nozik in 1977,¹¹⁸ motivating subsequent efforts.^{119–123} In a manner analogous to photosynthesis, photoelectrochemical diodes require as input only sunlight for creation of a portable chemical fuel, in this case hydrogen by splitting of the water molecule, with hydrogen evolved from the p-side and oxygen from the n-side of the photoelectrochemical diode. That useful photoelectrochemical diodes have not been realized is largely due to the lack of a suitable p-type semiconductor resistant to photocorrosion.

A schematic of the n-TiO₂:p-Cu-Ti-O coupled photoelectrochemical diode system is shown in Figure 32. The photoresponse of this system under global AM 1.5 illumination is shown in Figure 33. The n-TiO₂ nanotube array film was made by sputtering a Ti film upon a FTO coated glass substrate, then performing an anodization¹¹⁵ to achieve a titania nanotube array structure approximately 600 nm long, 30 nm pore size, with wall thickness of about 7 nm; the initially amorphous sample was oxygen annealed at 450 °C for one hour for crystallization. The p-Cu-Ti-O sample is that of sample 74, 550 °C vacuum annealed for 1 h, nanotube array length 1 μm, pore size ≈65 nm, wall thickness ≈35 nm, see Table 2. The films, atop FTO coated glass substrates, were mounted by use of epoxy into a glass sheet that allowed separate collection of the evolved gases. The TiO₂ nanotube array side of the diode was kept in 1 M

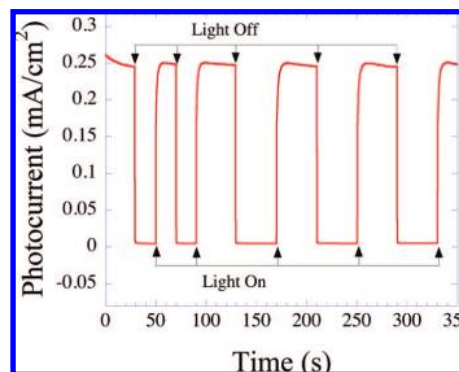


Figure 33. Photocurrent from self-biased photochemical diode comprised of an n-type TiO₂ nanotube array, p-type Cu-Ti-O nanotube array under global AM 1.5 illumination (geometry shown in Figure 33). Light is incident upon the oxygen evolving TiO₂ side of the diode, with the visible portion of the spectrum passing to the Cu-Ti-O side. The n-TiO₂ side of the diode is kept immersed in a 1 M KOH aqueous solution, the p-Cu-Ti-O side is kept in 0.1 M Na₂HPO₄ with a salt bridge linking the two sides solution. Reprinted with permission.¹¹⁴

KOH, and the Cu-Ti-O side kept in 0.1 M Na₂HPO₄ with a salt bridge linking the two sides. Keeping the Cu-Ti-O side in KOH solution resulted in significantly greater photocurrents, ≈20×; however, the performance decayed with time as the CuO turned into copper. The AM 1.5 illumination was incident upon the TiO₂ side of the diode, which absorbs Ultraviolet photons while passing visible light to the Cu-Ti-O side, thus minimizing any UV-assisted photocorrosion of the low bandgap material. A photocurrent density of approximately 0.25 mA/cm² is achieved corresponding to a photoconversion efficiency of 0.30%. After 4 to 5 h of operation, only a minimal amount of photocathode photocorrosion was seen for such samples in 0.1 M Na₂HPO₄ electrolyte.

8. Visible Light Responsive Ti-Fe-O Ternary Oxide Nanotube Arrays

8.1. Benefits of Nanostructuring Hematite. Hematite, or α-Fe₂O₃, is a n-type semiconductor with a ~2.2 eV bandgap¹²⁴ that is sufficiently large for water splitting but small enough to collect a significant fraction, ≈40%, of solar spectrum energy. However iron oxide suffers from low electron mobility, generally in the range of 0.01¹²⁵ to 0.1 cm²/V·s¹²⁶ resulting in rapid electron-hole recombination, and an insufficiently negative flat band potential as needed for spontaneous water splitting.¹²⁷ Therefore α-Fe₂O₃ solar spectrum photoconversion efficiencies reported to date are far from the theoretical maximum value of 12.9% for a material of this band gap.⁷⁴ Due to its visible spectrum bandgap, widespread availability, and nontoxicity iron (III) oxide nanostructures are of considerable interest for achieving efficient, cost-effective and durable photoelectrochemical solar cells. Various techniques have been investigated for the synthesis of iron (III) oxide nanostructures as it has proven to be a promising route to overcome low charge carrier mobility and high bulk recombination losses while offering large surface areas.¹²⁸ For example Duret¹²⁹ demonstrated photocurrents in the mA range under 1.5 a.m. solar illumination from mesoporous hematite thin films consisting of 5–10 nm thick nanoleaflets synthesized via ultrasonic spray pyrolysis. Recently, silicon doped α-Fe₂O₃ photoanodes were reported by Gratzel and co-workers,¹³⁰ while Ingler and Khan recently reported an α-Fe₂O₃ based self-biased photoelectrochemical cell.¹³¹

We first review the synthesis of self-aligned nanoporous iron(III) oxide formed by electrochemical oxidation of a starting

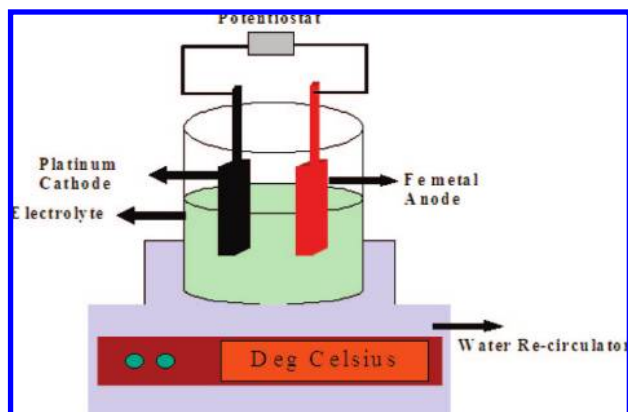


Figure 34. Schematic representation of the anodization setup used to fabricated nanoporous hematite. Reprinted with permission.¹⁹

Fe foil to achieve an amorphous nanoporous film and subsequent conversion to crystalline hematite by annealing.¹⁹ Then, we review our efforts to achieve high solar energy photoelectrochemical properties in a Ti–Fe–O ternary oxide composition, ideally combining the charge transport and photocorrosion properties of the TiO₂ nanotubes with the bandgap of α -Fe₂O₃.¹³²

8.2. Fabrication and Structural Characterization of Self-Aligned Nanoporous Iron(III) Oxide. Pure iron foil (99.9%) samples of 0.25 mm thickness was anodized in a two-electrode system with iron foil as the anode and platinum foil as the counter electrode, see Figure 34. After removal from the anodization bath the samples were thoroughly rinsed with deionized water and isopropyl alcohol, and then blow-dried with 99.99% pure nitrogen.

Electrolytes having lower diffusion coefficients are known to prevent local acidification at the oxide-electrolyte interface.¹³³ Glycerol is a highly viscous solvent where ions diffuse slowly, hence when we began our studies of nanoporous hematite formation we used glycerol as the electrolytic medium. Random self-organized nanopores were obtained in electrolytes under a narrow window of processing conditions, as described by Prakasam.¹⁹ Ethylene glycol is a viscous organic solvent (but with lower viscosity than glycerol) containing two alcoholic hydroxyl groups as opposed to glycerol's three hydroxyl groups. When an electrolyte comprised of 0.3 wt % NH₄F in ethylene glycol was used to anodize Fe foil at a potential of 40 V at 10 °C, a highly ordered nanoporous structure is obtained, see Figure 35, with clearly defined channels similar to those seen in nanoporous alumina.¹³⁴ Using an electrolyte held at 10 °C the pore depth was found to be around 2.5 μ m in 15 min and \sim 3 μ m in one hour, with 180 nm thick oxide barrier layer underneath the nanoporous layer. At 10 °C the structure remained nanoporous for an anodization duration up to \approx 70 min beyond which the pores collapsed. Room temperature anodization in the same electrolyte exhibited similar nanoporous surface, depth \sim 2 μ m in 10 min and 2.2 μ m in 15 min, with the nanoporous structure collapsing for anodization of 30 min duration or beyond. Independent of the anodization bath temperature the resulting pore diameters are \approx 30 nm at 40 V and \approx 60 nm at 60 V.

Owing to the fact that iron forms wires, rods, flakes and ribbons^{135,136} in the process of thermal oxidation, the samples were subjected to relatively brief anneals in a nitrogen atmosphere. We observed that longer annealing periods and higher temperatures resulted in a greater fraction of magnetite and pore filling. Thus a balance between structural stability

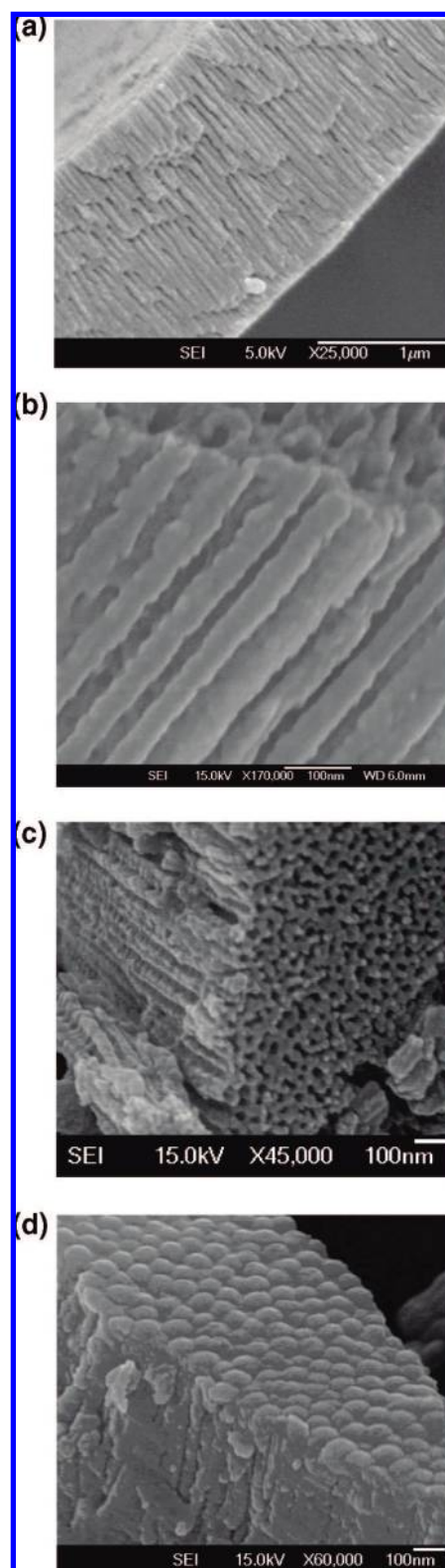


Figure 35. FESEM images of Fe sample anodized in 0.3 wt % NH₄F in ethylene glycol at 40 V, 10 °C for 15 min. Pictures (a–c) are cross-sectional images of a mechanically fractured sample, while (d) shows the underside (barrier layer) of the highly ordered nanoporous Fe₂O₃. Reprinted with permission.¹⁹

and crystallization is achieved by annealing the samples at 400 °C for 30 min, with a ramp rate of 10 °C/min, in nitrogen atmosphere. Figure 36 shows an FESEM image of a sample anodized at 90 V in an electrolyte containing 1% HF + 0.3 wt % NH₄F + 0.2% 0.1 M HNO₃ in glycerol (pH 3) at 10

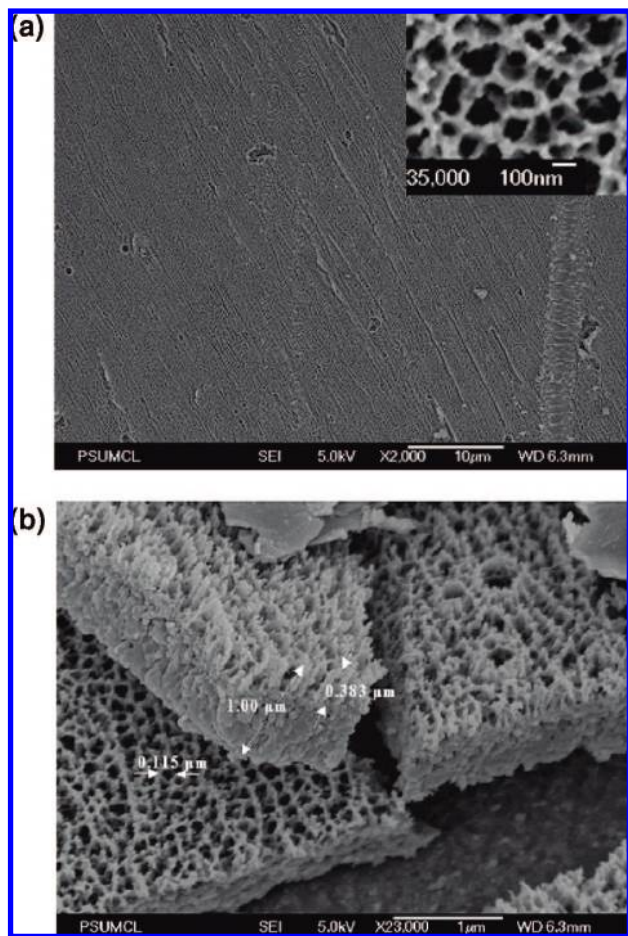


Figure 36. FESEM images of a sample annealed at 400 °C for 30 min showing: (a) the uniformity of the pore formation across the sample (insert shows the pore diameter after annealing); (b) cross sectional image showing the pore depth as 383 nm, pore diameter as about 100 nm, and the barrier oxide thickness as approximately 600 nm. Reprinted with permission.¹⁹

°C and annealed at 400 °C for 30 min. From Figure 36a we see that a crystalline nanoporous structure has been achieved with excellent uniformity. The cross sectional image of Figure 36b shows the extent of the pore depth (~380 nm) and the barrier layer thickness (~600 nm) of the annealed sample.

8.3. Photoelectrochemical Properties of Self-Aligned Nanoporous Iron(III) Oxide. Figure 37 shows the UV–visible absorbance spectrum of an annealed sample; the bandgap was determined from its corresponding reflectance spectrum. The differential reflectance ($dR/d\lambda$) was plotted as a function of bandgap energy and energy corresponding to the peak was extrapolated as the bandgap of the material.¹³⁷ Thus the bandgap was measured to be 2.2 eV, in agreement with the bandgap energy of α -Fe₂O₃ (iron(III) oxide).¹²⁴ Figure 38 shows the current–potential response of an illustrative annealed 90 V sample, 115 nm pore diameter, 400 nm pore depth, with potential measured relative to Ag/AgCl standard electrode under dark and 1.5 a.m. simulated solar illumination. Figure 38a shows the photoelectrochemical response in an electrolyte containing 1 M NaOH; the onset potential is ≈ 0.24 mV. After the measurement of Figure 38a, the sample was rinsed in DI water then measured in an electrolyte containing 0.5 M H₂O₂ (50%) and 1 M NaOH (50%), with the measured current–potential plot given in Figure 38b. The onset potential is -0.37 mV, several hundred mV more negative than in the 1 M NaOH

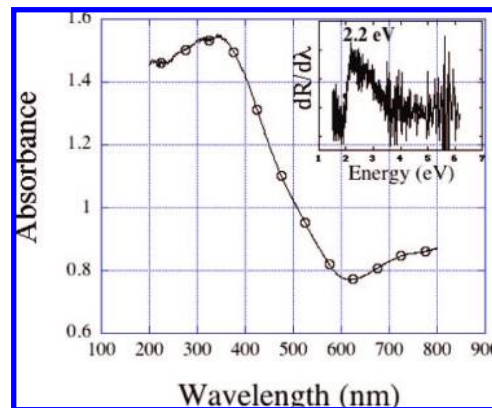


Figure 37. Optical absorption spectra of the Iron (III) Oxide photoanode obtained by diffuse reflectance measurement. The insert shows differential reflectance plotted as a function of energy. The $dR/d\lambda$ peak value corresponds to a bandgap energy of 2.2 eV. Reprinted with permission.¹⁹

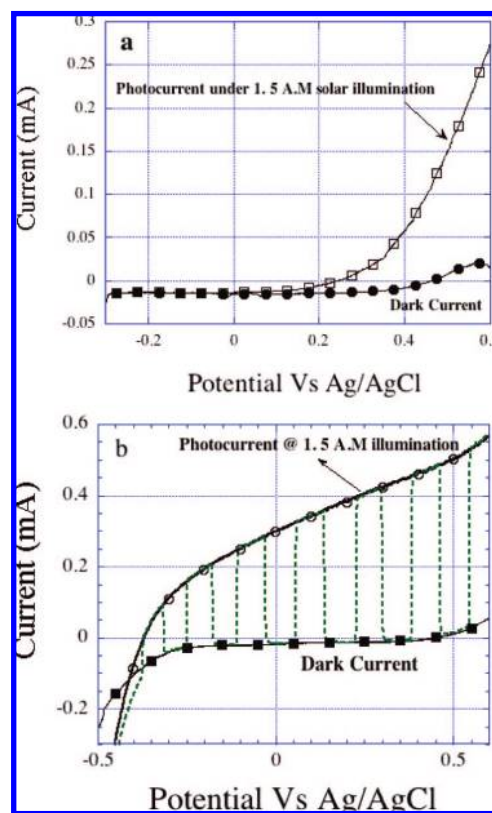


Figure 38. Photocurrent as a function of measured potential for the iron(III) oxide photoanode (anodized in 0.2% 0.1 M HNO₃, 1% HF, and 0.3 wt % NH₄F in glycerol at 10 °C) recorded in (a) 1 M NaOH solution and (b) 0.5 M H₂O₂ + 1 M NaOH solution under 1.5 a.m. simulated solar illumination. Reprinted with permission.¹⁹

solution.¹²⁹ The addition of H₂O₂ enhances the reaction kinetics as the photo oxidation rate of H₂O₂ is much larger than that of water.¹³⁸

8.4. Fabrication and Structural Characterization of Ti–Fe–O Nanotube Array Films. Ti–Fe metal films were deposited on fluorine doped tin oxide (FTO) coated glass substrates by simultaneous cosputtering from titanium and iron targets. The substrate temperature was maintained at 350–400 °C. Details of sputtering conditions, the resulting thickness of the Ti–Fe metal films and their crystallinity are given in Table 3. The metal films of high titanium or high iron concentration are crystalline, with the former a hexagonal titanium lattice and

TABLE 3: Summary of Fe–Ti–O Film Formation Parameters¹³²

sample	Fe target power (W)/ sputter rate (nm/s)	Ti target power (W)/ sputter rate (nm/s)	substrate temp. °C	film thickness (nm)	film composition	crystallinity of metal starting film
69	300/5.5	100/2.5	350	400	69% Fe – 31% Ti	crystalline
44	300/5.5	300/7.0	350	1000	44% Fe – 56% Ti	crystalline
37	250/4.1	300/7.0	350	500	37% Fe – 63% Ti	amorphous
26	200/2.5	300/7.0	350	400	26% Fe – 74% Ti	amorphous
20	150/1.3	300/7.0	400	750	20% Fe – 80% Ti	amorphous
6.6a	100/0.5	300/7.0	400	750	6.6% Fe – 93.4% Ti	crystalline
6.6b	100/0.5	300/7.0	400	1500	6.6% Fe – 93.4% Ti	crystalline
3.5	50/0.25	300/7.0	400	750	3.5% Fe – 96.5% Ti	crystalline

the latter a cubic iron lattice. Films with moderate levels of iron were amorphous. Irrespective of the crystallinity of the starting film, the anodized films were amorphous with a very thin residual metal layer underneath. Distinct nanotube arrays were formed from samples having iron concentrations less than about 70%. Films of higher Fe content, up to 100% Fe, were fabricated and characterized, however since they showed significantly diminished photoelectrochemical properties were not further considered. Ti:Fe metal films in the ratios 31:69, 56:44, 63:37, 74:26, 80:20, 93.4:6.6, and 96.5:3.5, as determined from the relative sputtering rates; sample numbers indicate Fe content. Anodization of the Ti–Fe films was performed at 30 V in ethylene glycol containing 0.3 wt % NH_4F and 2.0 vol % deionized water. Illustrative cross-sectional and bottom-side FESEM images of sample 20 are shown in Figure 39.

As-anodized Ti–Fe–O nanotube films are amorphous, partially crystallized by annealing in oxygen atmosphere at 500

°C for 2 h with a ramp up and down rate of 1 °C/min. GAXRD patterns of the annealed films are seen in Figure 40. All studies on TiO_2 nanotube array films made by anodization have indicated the tubes to be anatase, fixed atop a rutile base.⁸⁹ The Ti–Fe–O samples with low iron concentrations show the presence of anatase phase; sample 3.5 is largely anatase with a dominant (110) plane, and a small amount of rutile. The anatase phase disappears at higher iron concentrations (see the patterns of samples 20 and 37). The presence of the rutile peak is evident in samples 6.6 and 20, which is consistent with the fact that low amounts of iron in titania aid rutile formation.¹³⁹ The predominant (104) plane of $\alpha\text{-Fe}_2\text{O}_3$ coincides with the second intense plane of FTO, used as the conductive layer on the glass substrate, and its subsequent two less intense planes, (110) and (116), appear at $2\theta = 35.6$ and 54.1 respectively. In sample 37 the proportion of rutile increases slightly, and anatase is almost negligible. In general, samples 20 and 37 showed poor crystallinity, sample 44 showed pseudobrookite phase, while sample 69 showed hematite phase. In general, it appears that the presence of iron inside the TiO_2 matrix degrades the crystallization process since the proportion of rutile does not increase with decreasing amounts of anatase, an outcome possibly due to the fixed 500 °C annealing temperature. However higher annealing temperatures spoil the FTO–TiFeO interface, resulting in samples of high series resistance demonstrating essentially nil photoelectrochemical properties.

The crystalline nature of the nanotube walls is critical to applications involving light absorption, electrical carrier generation, and carrier transport therefore the crystalline nature of the nanotube walls were studied using HRTEM. Sample 20, with

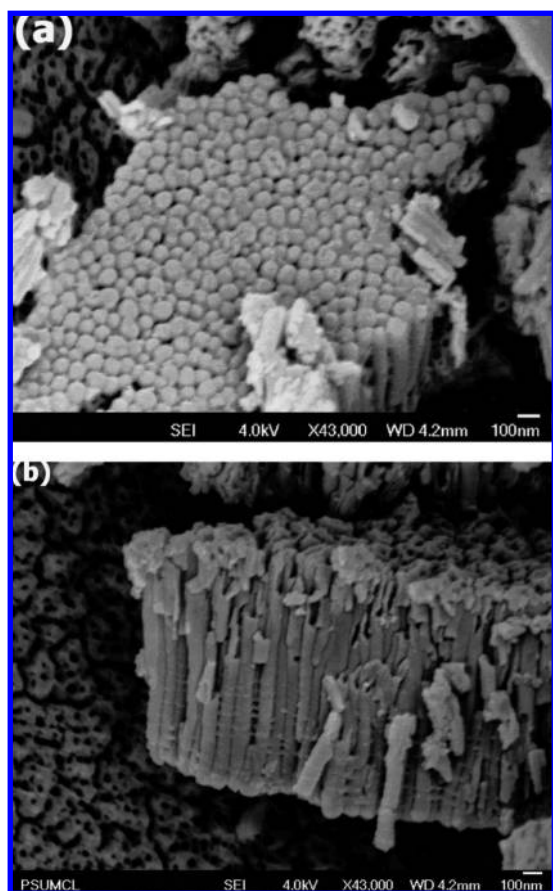


Figure 39. Illustrative FESEM images of Ti–Fe–O nanotube array sample 20, image of tube bottom (a) and lateral view (b). Reprinted with permission.¹³²

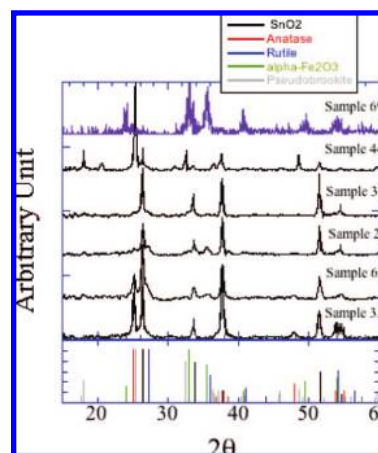


Figure 40. GAXRD patterns of Ti–Fe–O nanotube array samples annealed at 500 °C in dry oxygen for 2 h, see Table 3 for fabrication details. Standard patterns for anatase, rutile, pseudobrookite, $\alpha\text{-Fe}_2\text{O}_3$ (hematite), and tin oxide (substrate) are shown for phase identification. Reprinted with permission.¹³²

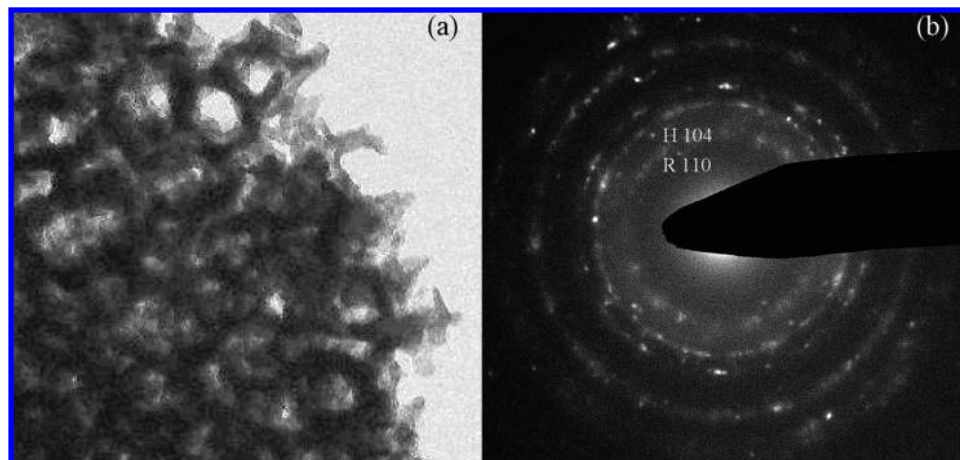


Figure 41. (a) TEM image of sample 20 annealed at 600 °C and (b) selected area diffraction pattern (H, hematite and R, rutile). Reprinted with permission.¹³²

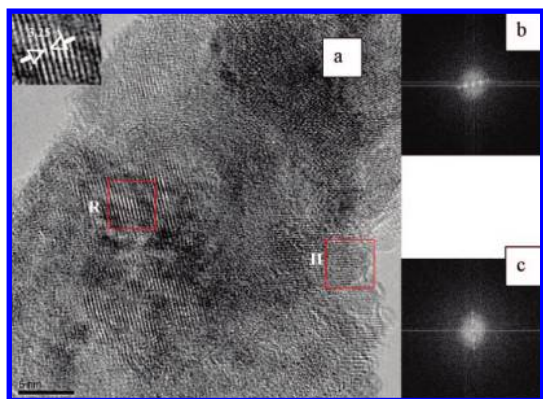


Figure 42. (a) HRTEM image of a nanotube wall (sample 20 annealed at 600 °C) showing rutile (region R) and hematite (region H) crystallites with the lattice image of region R given in the upper-left inset; (b) FFT of region R showing a predominate 110 plane, and (c) FFT of region H showing a predominate 104 plane. Reprinted with permission.¹³²

moderate iron doping was used for the study. TEM studies confirmed the relatively poor crystallinity of samples annealed at 500 °C; hence, further studies were conducted on a sample 20 annealed at 600 °C for 2 h in oxygen. As seen in Figure 39, the nanotube morphology can appear as a column of stacked rings as can be discerned in the TEM image of Figure 41a.^{2,115} A selected area electron diffraction (SAED) pattern from the corresponding region is shown in Figure 41b. Although the pattern shows mainly rutile phase, reflections from hematite phase also can be seen. Figure 42a shows a HRTEM image of a nanotube wall, with the polycrystalline nature evident from the figure. The crystallites have a wide size distribution. The crystallite marked R has a rutile structure the lattice image of which is given in the upper left inset. A fast Fourier transform (FFT) of regions R and H are given in Figure 42, panels b and c, indicating the presence of rutile and hematite phases in the respective regions. To find the distribution of iron within the nanotube walls an energy dispersive X-ray spectroscopy (EDS) line scan was performed via scanning transmission electron microscopy (STEM), see Figure 43. The intensity of both the Ti K α and Fe K α lines are maximum at the center of the wall due to its torus shape. Despite the presence of isolated hematite crystallites, a relatively uniform distribution of iron relative to the titanium can be seen across the wall. It appears that some of the iron goes into the titanium lattice substituting titanium

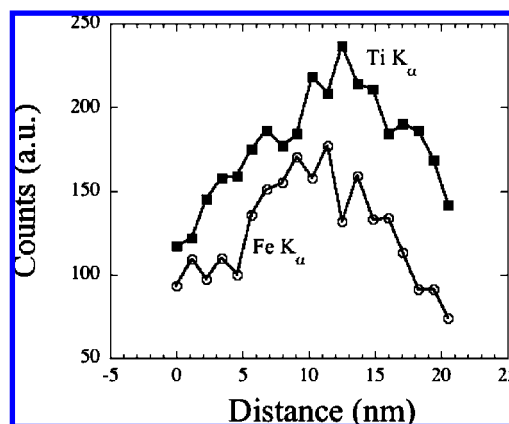


Figure 43. EDS line scan profile across nanotube wall (from region similar to that shown in Figure 42a). Reprinted with permission.¹³²

ions, and the rest either forms hematite crystallites or remains in the amorphous state.

Crystallization of the as-anodized amorphous nanotubes takes place through nucleation and growth.¹³⁹ Hence, a sufficiently high temperature and appropriate duration are needed for the complete transformation of the amorphous phase into crystalline. Removal of the amorphous phase is critical for effective device application, however even after annealing at 600 °C sample 20 showed the presence of amorphous regions. HRTEM studies indicate that rutile and hematite phases are formed in separate events depending upon the temperature and nature of the nucleation sites. In general, the nanotubes of moderate iron concentration consist mainly of rutile phase with hematite crystallites randomly distributed.

8.5. Photoelectrochemical Properties of Ti–Fe–O Nanotube Array Films. Figure 44 shows the absorbance of the annealed samples; as expected the absorbance edge shows a red shift with increasing Fe content. Figure 45 shows current versus voltage characteristics for the nanotubular Ti–Fe–O electrodes under dark and simulated sunlight in 1.0 M NaOH. The electrodes show *n*-type behavior, i.e. positive photocurrents at anodic potentials. The dark current in each case is negligible up to 0.65 V (vs Ag/AgCl) beyond which the dark currents for water oxidation dominate, therefore no photocurrent saturation is observed. A metal-coated glass substrate was placed adjacent to translucent Sample 6.6b, reflecting the transmitted light back into the sample. This method increased the photocurrent from 1.50 to 2.0 mA/cm² at 0.65 V (vs Ag/AgCl). This is a significant

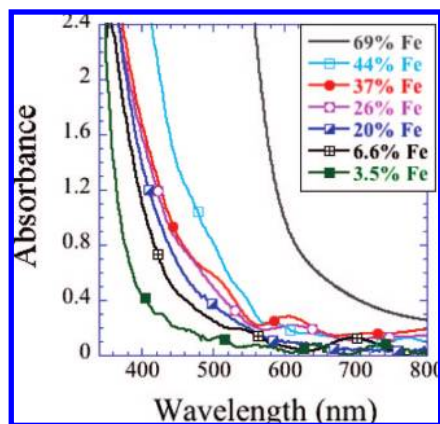


Figure 44. Absorbance spectra of 500 °C annealed Ti-Fe-O nanotube array films, see Table 3. Reprinted with permission.¹³²

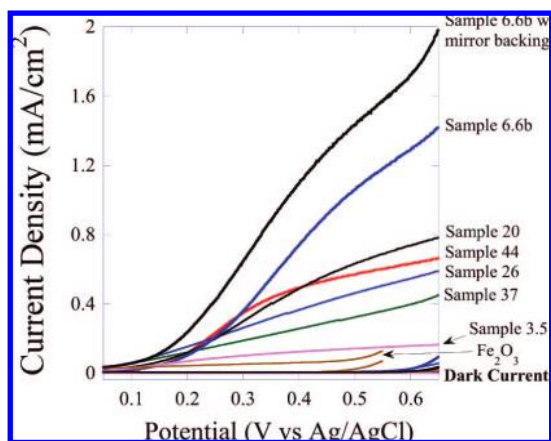


Figure 45. Photocurrent density versus potential in 1 M NaOH solution for annealed Ti-Fe-O nanotube array samples, and α -Fe₂O₃ nanoporous film, under AM 1.5 (100 mW/cm²) illumination. Dark currents are also shown for each sample. Reprinted with permission.¹³²

photocurrent considering the relatively poor film crystallinity, the relatively thick nanotube walls, approximately 22 nm thick-far greater than the ≈ 5 nm minority carrier diffusion length of iron oxide, and relatively thin Fe-Ti-O film thickness resulting in its translucent nature. For comparison the photocurrent of a pure nanoporous α -Fe₂O₃ film 1.5 μ m thick on FTO glass is also shown in Figure 45, prepared by anodic oxidation of an iron film at 30 V in ethylene glycol containing 0.3 wt% NH₄F and 0.5% deionized water. Even though this film strongly absorbs visible light the poor electron mobility results in a maximum photocurrent of approximately 25 μ A/cm² at 0.4V (vs Ag/AgCl). The highest photocurrent is exhibited by Sample 6.6, while the lowest photocurrent is demonstrated by sample 3.5. It appears that minimal levels of Fe³⁺ ions act as trap sites, while significant amounts of Fe³⁺ ions increase the recombination rate of the photogenerated electron-hole pairs.

Recently, we achieved iron oxide nanotube arrays, by anodization of Fe films, through a minor variation on the anodization technique reported by Prakasam and co-workers¹⁹ for fabrication of self-aligned nanoporous iron oxide, see section 8.2. Anodizing iron in an electrolyte comprised of 0.3 wt % NH₄F in ethylene glycol, 40 V, 10 °C, resulted in a highly ordered nanoporous structure,¹⁹ see Figure 35b. While atmospheric moisture does manifest itself in the electrolyte, we find that addition of small amounts of water to the above electrolyte formulation, typically a few percent, e.g. 2%, results in the formation of amorphous iron oxide nanotube arrays up to a few

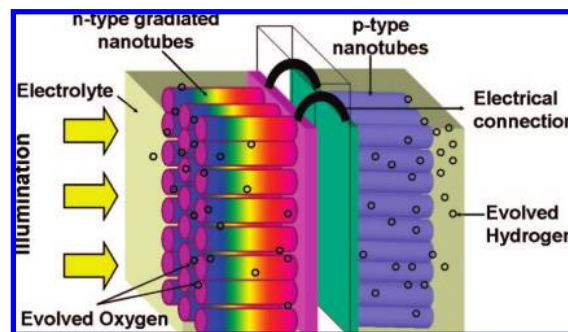


Figure 46. Depiction of the proposed self-biased photoelectrochemical diode consisting of an n-type compositionally graded nanotube array photoanode and a p-type nanotube array cathode.

microns in length. With respect to photo electrochemical application, we are currently optimizing annealing conditions to obtain hematite (α -Fe₂O₃ nanotube arrays, rather than magnetite, and avoid unwanted filling of the nanotube pores due to the oxide growing up from the underlying metal substrate.

9. Compositionally Graded Photochemically Active Ternary Oxide Nanotube Arrays

We propose the construction of compositionally graded ternary oxide nanotube arrays to enable the same photoelectrode to efficiently absorb light over different wavelength-regions of the solar spectrum. An analogous approach has been proposed in the field of solar energy conversion, namely the so-called “rainbow solar cells”.¹⁴⁰ Such solar cells employ the size-quantization effect intrinsic to quantum dots together with an ordered TiO₂ “backbone” for electron transport. By varying the size of the semiconductor quantum dots, the solar cells can be tuned to absorb light of certain wavelengths. Smaller quantum dots absorb shorter wavelengths of light, while larger quantum dots absorb longer wavelengths. Combining different-sized quantum dots on the same photoelectrode allows the construction of solar cells that absorb more light and thereby deliver power at greater efficiencies compared with solar cells made of bulk semiconductors. Additionally, as shown in the case of TiO₂/PbS,¹⁴¹ size quantization drives the energetics to more favorable levels to initiate charge injection from excited PbS into TiO₂ particles.

In Figure 46 we show a hypothetical self-biased photoelectrochemical diode consisting of a compositionally graded n-type nanotube array photoanode and a p-type cathode. As Figure 46 shows, the larger bandgap stoichiometries are closer to the surface and hence the illumination source, providing a window effect with the absorption of high energy photons while allowing optical transmission of lower energy photons which would be absorbed by the smaller band gap nanotube arrays closer to the substrate. A broad swathe of light energy ranging from the absorption edge of the large band gap oxide to the absorption-edge of the smaller band gap oxide would be more efficiently harvested. Ideally, photogenerated holes quickly oxidize solution ions while photogenerated electrons percolate down through the nanotube walls toward the substrate where they are collected. A key design criterion is the appropriate matching of energy levels such that photogenerated electrons easily travel down the conduction band of the compositionally graded nanotube array. Practical realization of such an architecture would require cosputtering a bimetallic film with graded composition, followed by anodization in a suitable electrolyte to form the nanotube arrays and a subsequent thermal anneal to induce crystallinity, a challenge we believe to be tractable.

10. Photoelectrochemical Heterojunctions Of TiO₂ Nanotubes With CdS and CdTe

Filling the TiO₂ nanotube array pores with a semiconductor that has a narrow band gap and an energetically high-lying conduction band is an attractive strategy to improve sunlight harvesting by TiO₂ nanotube arrays. Due to enhanced light absorption and scattering within the nanotubular architecture, the optical path length for absorption is larger than the film thickness.

In traditional planar junction solar cells, efficient collection of charge carriers photogenerated over the entire depth of light absorption is contingent on the semiconductor absorber possessing a long enough minority carrier diffusion length. A vertically oriented array of high aspect-ratio nanotubes circumvents this problem due to the orthogonalization of charge transport and separation intrinsic to the nanotubular architecture.¹⁴² Photogenerated holes have only a short distance to travel before finding a solution ion to oxidize, thus reducing recombination losses. Due to this advantage, TiO₂ nanotube arrays have been previously used by our research group^{6,26–28} and others^{143–145} as substrates for constructing highly efficient dye-sensitized solar cells and polymer/TiO₂ hybrid solar cells.

CdS is a semiconductor with a band gap of 2.5 eV¹⁴⁶ which is commonly used in its n-type form. Since the conduction band of bulk CdS is ca. 0.5 V more negative than that of TiO₂, this coupling of the semiconductors should have a beneficial role in improving charge separation. CdTe is a highly absorbing narrow bandgap semiconductor whose band gap ($E_g = 1.5$ eV) is nearly ideal for terrestrial solar energy conversion.¹⁴⁷ p-type CdTe is commonly used as the absorber layer in planar heterojunction solar cells in conjunction with n-type CdS as the window layer.¹⁴⁷ The planar CdS/CdTe heterojunctions have demonstrated impressive efficiencies of up to 16% in solar cells.^{148,149} Using CdTe, efficiencies as high as 30% are theoretically possible; however, better charge separation and collection are required to approach this limit. Our motivation in pursuing research in CdTe-TiO₂ heterojunctions is 2-fold: to enhance the harvesting of light of TiO₂ nanotubes and to explore the performance of three-dimensional heterojunction photoelectrochemical cells consisting of enormously increased junction area and orthogonalization of the processes of charge generation and separation.¹⁴² Transparent TiO₂ nanotube arrays prepared by the anodization of titanium thin films sputter-deposited onto conductive glass substrates were used for this study. The band alignment between TiO₂ and CdTe is favorable for the transfer of photoexcited electrons from the conduction band (CB) of CdTe into the CB of TiO₂, which is beneficial for reducing the rate of electron–hole recombination in the CdTe layer.¹⁵⁰ Efficient electron injection from the CB of CdTe to that of TiO₂ has been observed by Ernst and co-workers when a thin layer of CdTe was deposited on nanoparticulate TiO₂ electrodes.^{151–153}

10.1. Fabrication and Structural Characterization of CdS Coated Nanotubes. TiO₂ nanotube electrodes, resting upon an underlying Ti metal base, were prepared by anodization of Ti foil samples at 20 V in a HF and acetic acid solution.² These amorphous samples were then crystallized at 480 °C for 6 h in oxygen gas ambient. A CdS film was then deposited upon the crystallized TiO₂ nanotube array by cathodic reduction, using a conventional three-electrode system comprising an Ag/AgCl reference electrode and Cd counter electrode.^{154,155} A mixed solution of saturated elemental sulfur in benzene with 0.6 M CdCl₂ in dimethyl sulfoxide (DMSO) was used as the electrolyte. The solution was bubbled with flowing N₂ for 30 min prior to electro-deposition in order to remove O₂ and any moisture

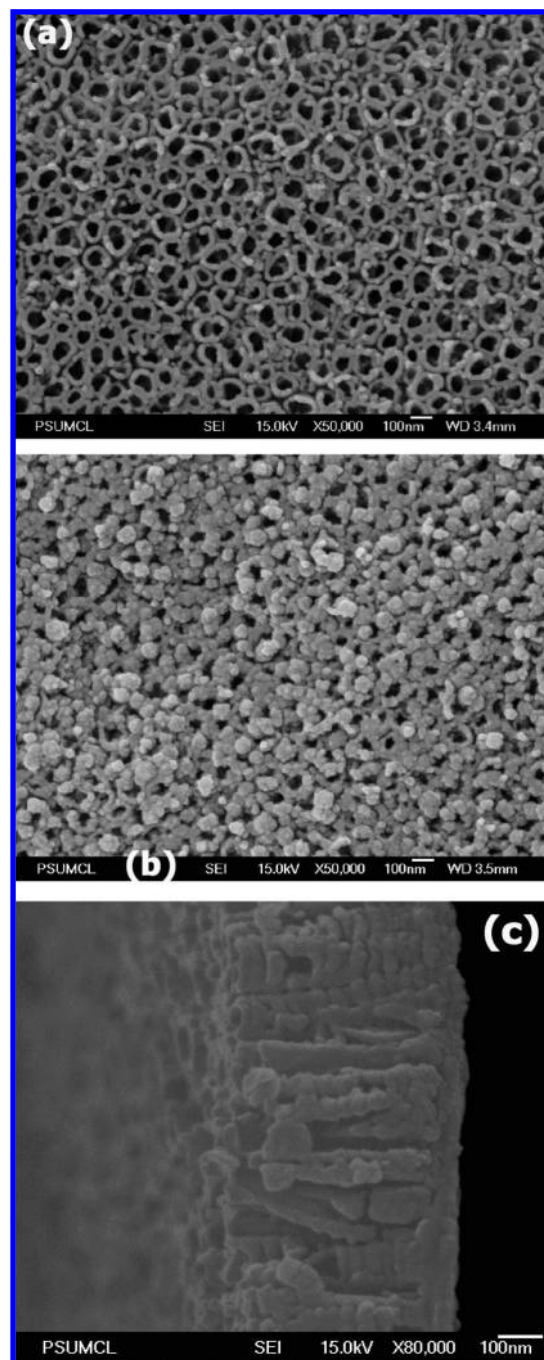


Figure 47. Top surface FESEM view of: (a) TiO₂ nanotube-array electrode and (b) CdS-TiO₂ nanotube-array electrode after CdS electrodeposition at -0.5 V for 30 min. (c) Illustrative cross-sectional image of CdS electrodeposited sample, -0.5 V for 30 min. The barrier layer is to the right, seen as a continuous seam at the edge of the sample. Reprinted with permission.¹⁵⁴

within the solution. The cathodic potential was kept constant at -0.5 V for different deposition times. After electrodeposition the samples were thoroughly rinsed with acetone, methanol and D.I. water. The prepared CdS–TiO₂ electrodes were annealed at 350 and 400 °C for 1 h in a N₂ atmosphere to investigate the influence of annealing on their photoelectrochemical response. It was suggested that, when a cathodic potential is applied to the TiO₂ nanotube electrode, it will reduce sulfur to S²⁻ on the electrode surface, while the applied electric field induces Cd²⁺ to migrate toward the electrode hence under proper conditions CdS will form at the electrode surface.¹⁵⁶ Figure 47a shows an illustrative FE-SEM image, top surface view, of a TiO₂

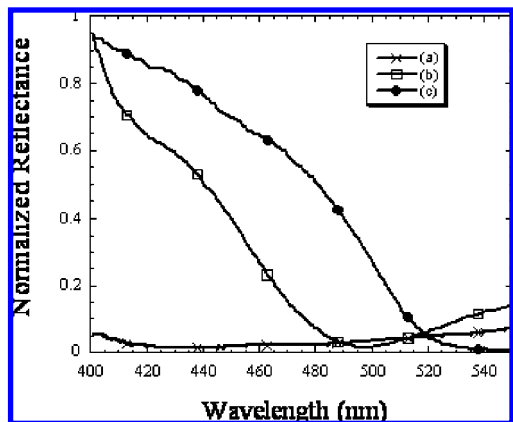


Figure 48. Normalized visible reflectance spectra of CdS-TiO₂ nanotube-array electrodes. (a) TiO₂ nanotube-array electrode; (b) 20 min -0.5 V electro-deposited CdS modified TiO₂ nanotube-array electrode, as fabricated; (c) electrode of (b) after annealing at 350 °C for 60 min in N₂. Reprinted with permission.¹⁵⁴

nanotube-array upon which just a few CdS nanoparticles, ≈ 20 nm diameter, have been deposited (-0.5 V for 5 min). The nanotubes have a length of ≈ 400 nm, and a barrier layer thickness of ≈ 50 nm; the average pore diameter as calculated from the FESEM images was 76 nm with a standard deviation of 15 nm, and wall thickness of 27 nm with a standard deviation of 6 nm. Figure 47b shows the topology after a 30 min (-0.5 V) electrodeposition of the CdS nanoparticles; the TiO₂ nanotubes have been extensively covered with a relatively uniform layer of CdS nanoparticle ‘clumps’ ranging in diameter from 40 to 100 nm. Figure 47c is an illustrative cross-sectional image of CdS electrodeposited sample, -0.5 V for 30 min, that has been freed from the underlying titanium substrate. The barrier layer is to the right, seen as a continuous seam at the edge of the sample. Although it is possible, and indeed likely that some CdS nanoparticles reside within the nanotube arrays we have not been able to detect any through FESEM imaging.¹⁵⁴

10.2. Optical and Photoelectrochemical Characterization of CdS Coated Nanotubes. Figure 48 shows the normalized visible reflectance spectra of a plain TiO₂ nanotube-array electrode, as well as CdS modified TiO₂ nanotube-array electrodes. The reflectance onset was determined by linear extrapolation from the inflection point of the curve toward the baseline. From Figure 48, one can see that deposition of the CdS film atop the TiO₂ nanotube-array electrode has red-shifted the absorption edge into the visible region, with the absorption tail extending to 500 nm; the bandgap calculated from this reflectance edge is about 2.53 eV. After annealing (N₂, 350 °C, 1 h) its absorption behavior has further red-shifted, with the reflectance tail extending to 515 nm, a calculated edge bandgap of 2.41 eV, a typical bandgap value for bulk CdS. The absorption edge corresponds to a nanoparticle size of approximately 10–20 nm.^{157,158} With annealing the CdS particles aggregate, causing the spectrum to red-shift, a behavior previously attributed to the formation of valence-band tail states.¹⁵⁹

The I – V characteristics of CdS-sensitized TiO₂ nanotube electrodes are presented in Figure 49 for an illumination intensity of 1 sun (AM 1.5, 100 mW/cm², light of wavelength below 400 nm was filtered). The measurements were done in 1.0 M Na₂S electrolyte solution, an efficient hole scavenger for CdS in which the electrodes are stable. For the as-prepared CdS–TiO₂ electrode, photocurrent onset occurs at -1.30 V vs Ag/AgCl, a -0.60 V negative shift compared to the plain TiO₂ nanotube-array electrode. In comparison to the plain TiO₂

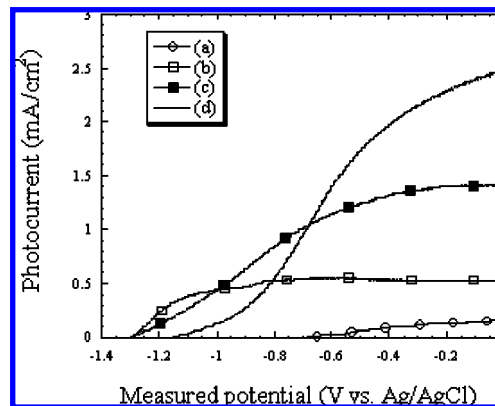


Figure 49. Photocurrent versus voltage in 1 M Na₂S under AM 1.5 (1 sun), 100 mW/cm² illumination: (a) bare TiO₂ nanotube electrode. (b) As-prepared electrodeposited CdS film (-0.5 V, 30 min) upon TiO₂ nanotube-array electrode. (c) CdS–TiO₂ (-0.5 V, 30 min) electrode after annealing at 350 °C in N₂ for 60 min. (d) CdS–TiO₂ (-0.5 V, 30 min) electrode after annealing at 400 °C in N₂ for 60 min. Reprinted with permission.¹⁵⁴

nanotube-array electrode, addition of the CdS film increased the photocurrent from 0.16 to 0.55 mA/cm². The photocurrent response is sensitive to the annealing temperature, as discernible in Figure 49. The sample annealed at 350 °C, trace (c), reaches ≈ 1.42 mA/cm²; the 400 °C annealed sample, trace (d), reaches ≈ 2.51 mA/cm², respectively 9 and 16 times higher than that of bare TiO₂ nanotube array electrode of trace (a). The I – V curves of these samples gradually lose their well-defined photocurrent saturation as the annealing temperature increases. Higher temperature annealing may result in pore blockage due to sintering of the CdS nanoparticles, reducing the area accessible to the hole scavenging electrolyte solution.

10.3. Fabrication of CdTe–TiO₂ Nanotube-Array Heterojunctions. Transparent nanotubes were formed on fluorine doped tin oxide (FTO) glass (Hartford Glass, Hartford, IN) by potentiostatic anodization of 500 nm thick titanium films deposited on conductive glass slides via DC sputtering. After anodization the nanotube array films were crystallized to anatase TiO₂ by annealing at 450 °C in oxygen ambient for 2 h. The resulting nanotubes were transparent (bandgap energy = 3.4 eV) and showed n-type behavior with an average inner pore diameter near 50 nm, wall thickness of ≈ 13 nm, and 250–300 nm in length. A conventional three-electrode setup in an undivided cell was used for cathodic deposition of CdTe films ($3\text{H}^+ + \text{Cd}^{2+} + \text{HTeO}_2^+ + 6\text{e}^- \rightarrow \text{CdTe} + 2\text{H}_2\text{O}$).^{160–163} The reference electrode was an Ag/AgCl electrode in 4 M KCl solution, against which all of the potentials reported here were measured; deposition was carried out potentiostatically at -0.4 V versus the reference electrode. The aqueous deposition solutions consisted of 0.1 M CdSO₄ and 0.1 mM TeO₂ at pH 1.4 (H₂SO₄) and were maintained at 85 °C throughout the deposition. Newly made films were rinsed with DI water and dried under a stream of nitrogen. Annealed films were heated to 300 °C for 45 min, with a ramp of 2 °C/min. Some films were treated with CdCl₂ before annealing by a 120 s immersion in a saturated CdCl₂/methanol solution.

10.4. Photoelectrochemical Properties of CdTe–TiO₂ Nanotube-Array Heterojunctions. Photoelectrochemical properties of CdTe/TiO₂ nanotube-array electrodes were characterized by measuring short-circuit photocurrent using a 0.6 M Na₂S solution with pH adjusted to 12. A UV filter was used to expose the samples only to visible light. This effectively eliminated the photocurrent contribution from the TiO₂ nanotubes and

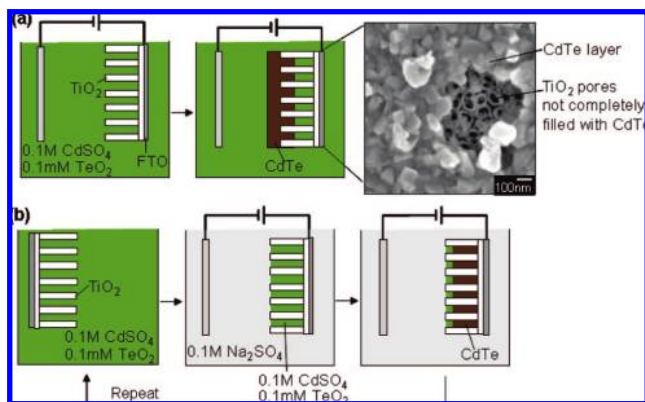


Figure 50. Schematic illustration of (a) a regular deposition method and (b) a newly developed dipping and deposition technique. Reprinted with permission.¹⁷¹

allowed the examination of the photocurrent generated by only the CdTe layer. The photocurrent generated by the TiO₂ nanotubes under the conditions used in this study was less than 1 $\mu\text{A}/\text{cm}^2$. The best photocurrents were obtained from CdTe/TiO₂ electrodes that were subjected to CdCl₂ treatment and a 300 °C thermal anneal. This is expected since the crystallinity of the CdTe layer is significantly improved by annealing the sample at 300 °C for 45 min in air. Furthermore, the CdCl₂ treatment is known for promoting recrystallization and CdTe grain growth during the annealing process as well as passivating defects.^{164–167} This process can effectively passivate defects and increase minority carrier lifetime, thereby improving device characteristics of the CdTe-based solar cells (e.g., open circuit voltage and fill factor).^{167–170} Consequently, the crystallinity of the CdTe films is further improved by dipping the CdTe layer in a methanol solution saturated with CdCl₂ before annealing. In order to make the best use of the nanotubular structures of TiO₂, it is critical that the internal area of each tube is sufficiently covered with CdTe before the entrances can become clogged. The challenge of depositing CdTe in the TiO₂ pores is that the bottom of the pores is no more conductive than the entrance of the pores, whereas diffusion makes deposition at the bottom of the pores less favorable than deposition at the entrance of the pores. This process can result in the deposition of a thick CdTe layer at the entrance of the pores, before a significant portion of the internal area is covered with CdTe, a schematic of which is shown in Figure 50a.

To overcome this problem, we employed a new technique that makes deposition in the pores more favorable than deposition on the surface of the TiO₂ nanotubes (schematic in Figure 50b). In this technique, we fill the pores of the TiO₂ tubes with an electrolyte containing Cd²⁺ and HTeO₂⁺ ions, utilizing capillary forces by dipping TiO₂ tubes in the plating solution and then move the TiO₂ electrode into a new medium that contains only an inert supporting electrolyte without Cd²⁺ and HTeO₂⁺ ions. Immediate electrodeposition in this medium results in deposition of CdTe only within the pores. This procedure can be repeated until a desired amount of CdTe is deposited in the pores.

The optimum amount of CdTe deposited in the TiO₂ pores varies depending on the purpose of forming a CdTe/TiO₂ junction. For building a solid-state solar cell, completely filling the n-type pores with a p-type material is desired to maximize p–n junction areas. However, for building a photoelectrochemical cell relying on the formation of an electrolyte/solid junction for charge separation, incomplete filling is desired so that the electrolyte can penetrate into the pores, increasing the electrolyte/

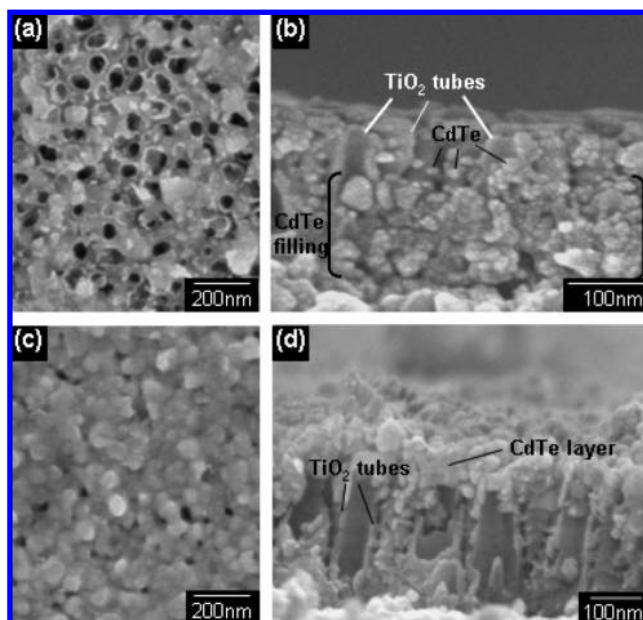


Figure 51. SEM images of CdTe layers deposited on TiO₂ nanotube arrays (a) topview and (b) cross-section of layers by 20 cycles of dipping and deposition (sample I); (c) topview and (d) cross-section of layers obtained by a regular deposition method (sample II). Reprinted with permission.¹⁷¹

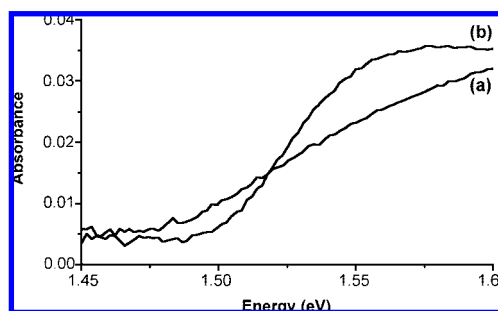


Figure 52. UV–vis spectra of CdTe layers deposited on TiO₂ nanotube arrays using: (a) 20 cycles of dipping and deposition (sample I) and (b) 30 min (sample II). Reprinted with permission.¹⁷¹

electrode junction area. For the photoelectrochemical cell we constructed, a CdTe/TiO₂ junction prepared with 20 cycles of the dipping and deposition method (sample I) was found optimal in achieving the highest photocurrent with a minimum amount of CdTe deposited.¹⁷¹ SEM images of this electrode are shown in Figure 51a,b. The top view SEM image shows the absence of a thick CdTe layer deposited on top of the TiO₂ pores (Figure 51a), indicating that this new method effectively suppresses deposition outside of the pores. The cross sectional SEM image confirms that CdTe is deposited successfully into the TiO₂ pores (Figure 51a). A CdTe layer deposited using a regular method for 30 min (sample II) is also shown for comparison (Figure 51c), which shows the presence of a thick CdTe layer covering the TiO₂ pores. The cross sectional SEM image of sample II shows that the insides of the TiO₂ pores, especially the bottom half of the pores, are not uniformly filled with CdTe (Figure 51d). The advantages of forming a high quality conformal CdTe/TiO₂ junction are evident when XRD patterns and UV–vis spectra of samples I and II are compared. XRD data shows that sample II possessing a thick CdTe layer contains at least four times more CdTe than sample I (not shown here), judging from the intensities of CdTe peaks.¹⁷¹ However, sample I shows a comparable photon absorption to sample II (Figure 52). This

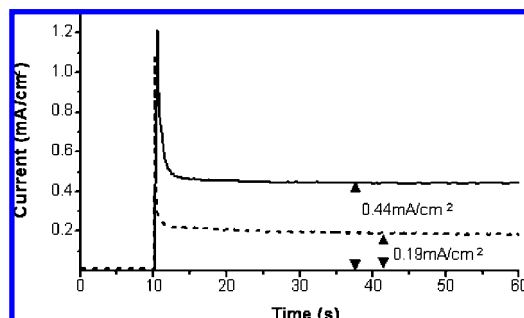


Figure 53. Short-circuit photocurrent measurement under visible light illumination of CdTe layers deposited on TiO₂ nanotube arrays using 20 cycles of dipping and deposition method (—) and a regular deposition method for 30 min (···). Reprinted with permission.¹⁷¹

indicates that the CdTe layer in sample I, forming a high quality conformal coating in the TiO₂ pores, can efficiently increase the path length of light in the CdTe layer while decreasing the actual amount of CdTe loaded. All CdTe/TiO₂ electrodes (with as-deposited, annealed, and annealed after CdCl₂ treatment CdTe layers) commonly generated anodic short-circuit photocurrent, indicating the presence of an upward band bending at the electrode/electrolyte interface. In this case, holes are consumed at the electrode/electrolyte surface to oxidize S²⁻ ions to polysulfide (S_n)²⁻ ions (e.g., S₂²⁻) while electrons are injected into the conduction band of TiO₂, transferred to the counter electrode, and used to reduce water or polysulfide ions to hydrogen or sulfide ions, respectively.¹⁷¹ When CdTe films were deposited directly onto an FTO substrate, it showed a p-type behavior, generating cathodic photocurrent as the photon-generated electrons are predominantly consumed at the CdTe/electrolyte interface.¹⁶³ This suggests that when the TiO₂/CdTe/electrolyte junction is formed the injection of photon-generated electrons from CdTe to TiO₂ becomes more efficient than the transfer of these electrons from CdTe to the species in the electrolyte.¹⁷¹ Another noticeable difference between CdTe/TiO₂ and CdTe electrodes is the photostability of the CdTe layer.¹⁷¹ The photocurrent generated by a CdTe layer deposited directly on an FTO substrate gradually diminishes over time. This is most likely due to photocorrosion, which involves the anodic formation of Te (CdTe + 2OH⁻ + 2p⁺ → HCD₂O⁻ + H⁺ + Te) and/or the cathodic formation of Cd (CdTe + 2e⁻ → Cd + Te²⁻).¹⁷² In contrast, the steady state photocurrent observed by the CdTe/TiO₂ electrode was stable and no sign of photocorrosion was observed.¹⁷¹ We believe that this is because of the more efficient hole consumption at the electrolyte/CdTe junction and electron transfer at the CdTe/TiO₂ junction (from the CB of CdTe to CB of TiO₂) achieved by enhanced electrolyte/CdTe/TiO₂ junction areas, which kinetically suppresses photocorrosion of the CdTe layer.

Photocurrent measurements of samples I and II provide another informative result (Figure 53). Although sample I shows a photon absorption slightly lower than sample II, the steady state photocurrent generated by sample I (0.44 mA/cm²) is significantly higher than that of sample II (0.19 mA/cm²). If we assume that samples I and II generate comparable numbers of electron–hole pairs by photon absorption, this difference in photocurrent is solely due to the reduced electron–hole recombination achieved in sample I, resulting from the formation of a more intimate CdTe/TiO₂ junction by the new deposition technique. This means that thinner and more even CdTe coating on the TiO₂ tubes allows for more efficient electron transfer at the CdTe/TiO₂ junction and hole transfer at the CdTe/electrolyte junction, minimizing electron–hole recombination in the CdTe

layer. This result shows that the advantages of using a three-dimensionally organized junction structure can be maximized only when a high quality conformal junction is created. The dipping and deposition technique used in this study may be used as a general method to form a high quality conformal junction on microporous and mesoporous substrates via electrodeposition when the bottom of the pores and the entrances of the pores are equally conductive.

11. Preparation and Properties of TiO₂ Nanowire Arrays on Transparent Conductive Substrates

11.1. Single-Crystalline 1D Oriented and Aligned Nanoarchitectures. The use of a photoelectrode constructed of 1D crystalline nanowire arrays, aligned perpendicular to the collecting TCO substrate has been demonstrated to improve the charge collection efficiency by promoting faster charge transport and faster ion diffusion at the semiconductor-electrolyte interface.^{173,174} These studies of single crystalline vertically oriented metal oxide nanowires structures to replace the nanoparticulate films have focused primarily on ZnO, where the efficiency was limited to approximately 1% even for films thicker than 20 μm, whereas the ZnO suffered from poor chemical stability.^{173,174} In contrast, TiO₂ is exceptionally stable, but the development of fast-transport photoelectrochemical cells using this material has been limited by the unavailability of aligned single crystalline nanowires on conductive glass. For practical applications, densely packed stable TiO₂ nanowire arrays on TCO glass are greatly demanded and the architecture developed by us fills this void. Our synthetic process is performed at relatively low temperatures hence the conductivity of the TCO glass substrate is unaffected. Yet another unique aspect of our work is that the single-crystal-like TiO₂ nanowires consist of the rutile phase instead of the more common anatase phase.

While wet chemical approaches that allow chemical reactions to occur at low temperature have been widely used to prepare 1D TiO₂,^{175–181} these methods are not available to grow nanowire arrays onto TCO substrate which greatly limit photoelectrochemical application of the TiO₂ nanowires. Herein we present a simple large-scale preparation method for highly crystallized TiO₂ nanowire arrays of up to 8 μm length on TCO glass via a “nonpolar solvent/hydrophilic solid substrate” interfacial reaction under hydrothermal conditions. The as-prepared densely packed nanowires grow vertically oriented from the TCO glass substrate with (001) crystal plan orientated.

11.2. Synthesis of Vertically Oriented Self-Aligned Nanowires on TCO Substrates. Well-cleaned FTO coated glass substrates were loaded into a sealed Teflon reactor (23 mL), containing 10 mL of toluene, 0.5 mL of tetrabutyl titanate, 1 mL of titanium tetrachloride (1 M in toluene), and 1 mL of hydrochloric acid (37 wt %). A reaction temperature of 180 °C is used, with reaction times lasting from 30 min to 48 h. After the reaction the nanowire covered TCO substrates were removed and washed with ethanol thoroughly and then dried in air.

11.3. Morphological and Structural Characterization. Panels a and b in Figure 54 are FESEM top-surface images of a typical as-synthesized nanowire array sample at low and high magnification, respectively, showing a highly uniform and densely packed array of nanowires with flat tetragonal crystallographic planes growing almost perpendicularly from the substrate. From the X-ray diffraction pattern, see Figure 55, the nanowires can be classified as tetragonal rutile (JCPDS file no. 21-1276); the enhanced (002) peak indicates the nanowire is

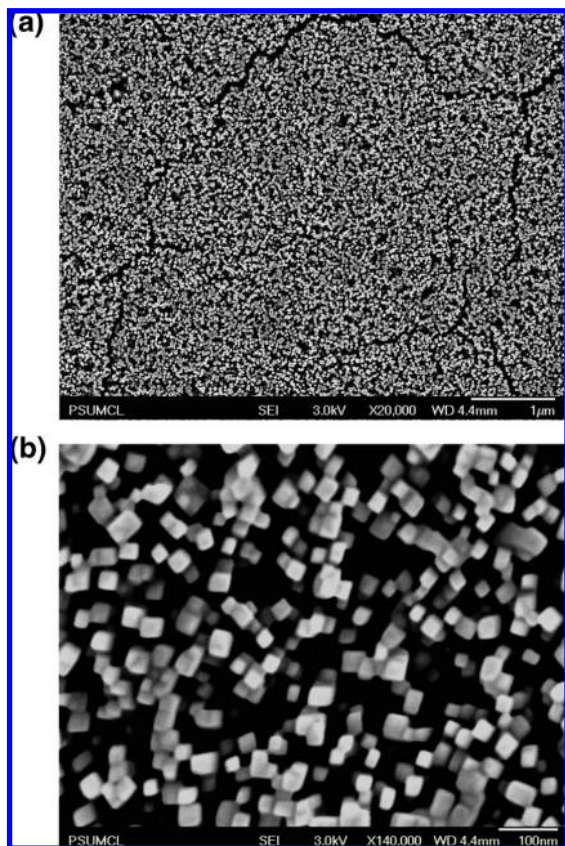


Figure 54. FESEM images of vertically oriented self-organized TiO_2 nanowire array grown on FTO coated glass at 180°C for 24 h: (a and b) Top-view images and (c) cross-sectional FESEM image of the same array, mechanically fractured. Reprinted with permission.¹⁸⁴

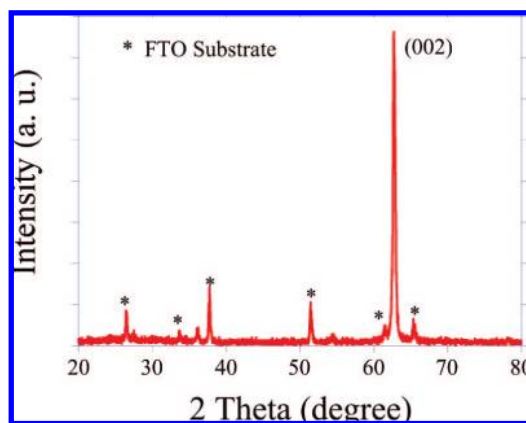


Figure 55. X-ray diffraction pattern of vertically oriented self-organized TiO_2 nanowires on FTO coated glass.¹⁸⁴

well crystallized and grows perpendicular to the substrate. TEM, HRTEM, and selected-area electron diffraction patterns, Figure 56a–c, confirm that the nanowires are single crystalline. The HR-TEM image shows a (110) interplane distance of 0.325 nm; the nanowires grow along the (110) crystal plane with a preferred (001) orientation.

11.4. Photoelectrochemical Properties of TiO_2 Nanowire Arrays. Figure 57 shows the photocurrent density and photoconversion efficiency versus potential of a $2.4\ \mu\text{m}$ long TiO_2 nanowire array electrode, nominal wire width 20 nm, sample size $0.5\ \text{cm}^2$, measured in 1 M KOH electrolyte under 1.5 a.m. solar illumination. The potential was scanned at a rate of 20 mV/s. The light-to-chemical energy conversion efficiency of the nanowires was determined in the two electrode configuration

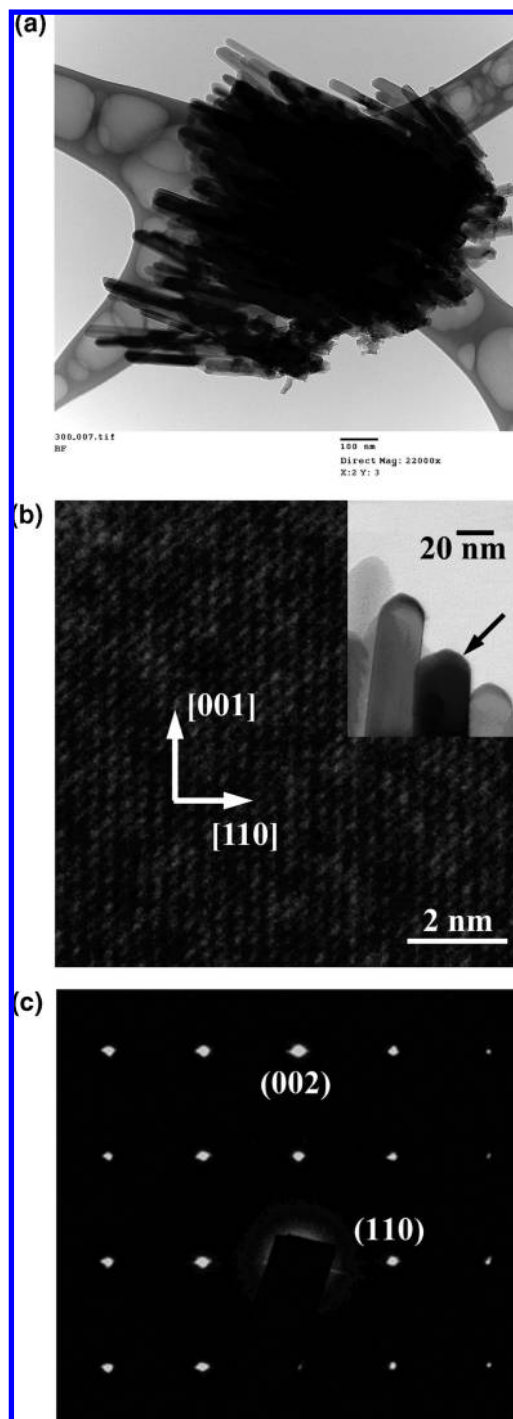


Figure 56. (a) TEM image of vertically oriented self-organized TiO_2 nanowires on FTO coated glass spanning a greater portion of the length of the nanowires (b) HRTEM image and (c) selected-area electron diffraction pattern. Reprinted with permission.¹⁸⁴

with TiO_2 nanowires on FTO glass as the working photoelectrode and platinum foil as a counter electrode; a photoconversion efficiency of 0.75% is obtained. Holes avoid recombination with electrons by oxidizing solution ions at the surface of the nanowires. The maximum distance holes in the rutile nanowires have to travel to reach the surface (the retrieval length) is equal to one-half the lateral dimension of the nanowire, which equates to a relatively short distance of $\sim 10\ \text{nm}$ in our samples. The electron mobility of single crystalline rutile is $\sim 1\ \text{cm}^2\ \text{V}^{-1}\text{s}^{-1}$, over 2 orders of magnitude larger than those for nanoparticulate TiO_2 films.¹⁸² Hence the combination of a short hole retrieval

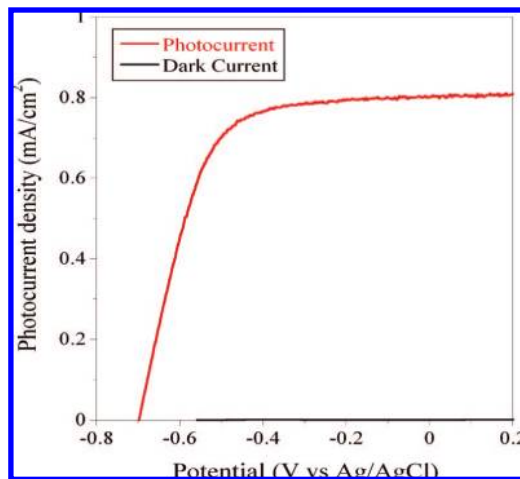


Figure 57. Photocurrent density and photoconversion efficiency of a TiO_2 nanowire array electrode as a function of measured potential [vs Ag/AgCl] in 1 M KOH under AM 1.5 illumination. Reprinted with permission.¹⁸⁴

length and fast electron transport may account for the excellent charge separation. Unlike nanoparticle-based electrodes that need a positive bias between 0.5 to 1 V (vs reference electrode) to completely separate the light generated electron–hole pairs,¹⁸³ the photocurrent of the TiO_2 nanowire array-based electrode increases sharply reaching saturation at -0.25 V indicative of both low series resistance and facile separation of the photo-generated charges.

12. Conclusions

In application to water photolysis, TiO_2 nanotube arrays fabricated on planar substrates demonstrate a quantum yield greater than 80% under ultraviolet illumination. The highest overall photoconversion efficiency of about 16.25% was obtained with a $20\ \mu\text{m}$ long nanotube array (320–400 nm, $100\ \text{mW}/\text{cm}^2$ illumination) annealed at $580\ ^\circ\text{C}$. Nanotube arrays have been successfully fabricated on curved nonplanar substrates such as Ti pipes and half pipes. The improvement in photoconversion efficiency for the pipe geometries appear to arise from the recycling of reflected light. Our data show that while planar samples can be very reflective close to their band edge, i.e., 350–400 nm, the amount of reflected light is greatly reduced

for the nonplanar geometries. This study demonstrates that it is both possible to grow nanotube arrays on nonplanar surfaces, and that these geometries can offer a 60% increase in efficiency over planar geometries through the recapturing of reflected light that would otherwise be lost.

The need for high-temperature crystallization limits nanotube array use with temperature sensitive materials, such as polymers, for applications such as photocatalytic membranes. Therefore, low-temperature synthetic routes, where a high-temperature annealing step for crystallization is not required, are needed to obtain the full benefit of the unique TiO_2 nanotube array architecture. The low-temperature synthesis of anatase and mixed anatase–rutile crystalline TiO_2 nanotube arrays of up to $1.4\ \mu\text{m}$ length using a two-step process has been demonstrated. The two-step process consists of initial treatment of the Ti foil in an oxidizing agent, an electrolyte containing either H_2O_2 or $(\text{NH}_4)_2\text{S}_2\text{O}_8$, followed by potentiostatic anodization of the resulting foil in an NH_4F -containing electrolyte. The crystallinity of the nanotube array films was confirmed using GAXRD and TEM measurements. The as-synthesized crystalline nanotube arrays were successfully tested as photoanodes for water photoelectrolysis, with performances comparable to samples annealed at high temperature.

TiO_2 nanotube arrays form a versatile architectural platform for which exploratory semiconducting systems may be developed for photoelectrochemistry. In particular the introduction of controlled amounts of oxide semiconductors with lower electronic band-gaps than TiO_2 into the TiO_2 nanotube walls offers a path to combine the excellent material strength and photocorrosion stability of TiO_2 with the superior light harvesting abilities of smaller band gap oxides. We have successfully fabricated iron oxide nanotube arrays, and Cu-Ti-O and Fe-Ti-O ternary oxide systems in nanotube array form and employed them for photoelectrochemistry.

Photoelectrochemical diodes, comprised of p-type and n-type semiconductors, are an appealing design as they require no energy input other than sunlight, with oxygen evolved from the n-type side and hydrogen from the p-type side facilitating gas collection. That useful photoelectrochemical diodes have not been realized is largely due to the lack of a suitable p-type semiconductor resistant to photocorrosion. We fabricated photocorrosion stable p-type Cu-Ti-O semiconductor electrodes by anodization of Cu-Ti films. The p- Cu-Ti-O films are in the form of vertically oriented, highly ordered arrays of nanotubes, a material architecture ideally suited for efficient

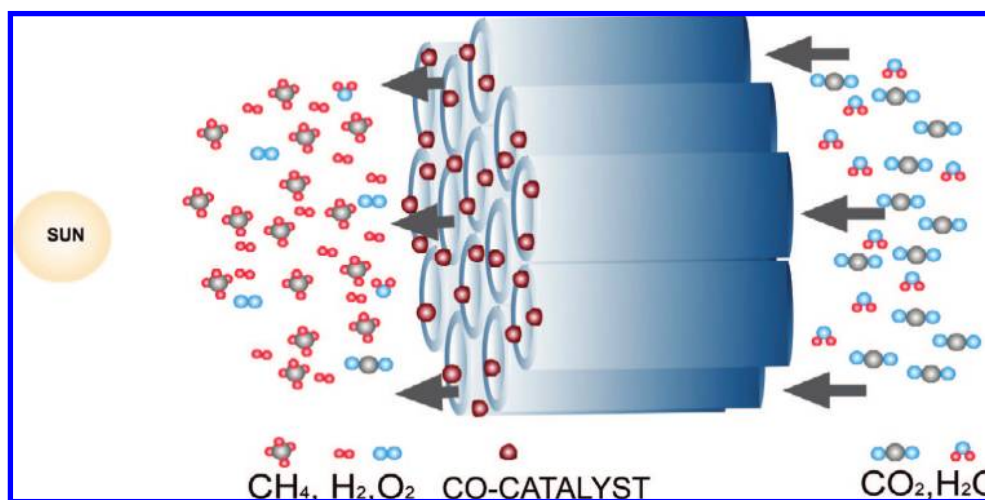


Figure 58. Depiction of TiO_2 nanotube array flow-through membrane, sensitized with appropriate catalysts, for photo catalytic conversion of CO_2 to hydrocarbon fuels.

water photolysis. The photocurrent action spectra show contribution over the visible light spectrum. In a manner analogous to photosynthesis, the p-type Cu–Ti–O nanotube array films are used in combination with n-type TiO₂ nanotube array films to achieve a pn-junction photochemical diode capable of generating a chemical fuel, in this case hydrogen, by water-splitting. Unlike easily anodized valve metals, the anodization of copper to simultaneously achieve oxidation and with morphological control has proven quite difficult. In this regard, our approach is unique in that we employ Ti as a supporting matrix to provide chemical resistance and mechanical support during the anodic oxidation of copper. The visible light absorbing p-type Cu–Ti–O nanotube arrays, used in combination with UV absorbing n-type TiO₂, enables formation of a complete photoelectrocatalytic system, made from earth-abundant elements, in the form of a photoelectrochemical diode for the solar generation of hydrogen by water splitting. The photochemical reactions are powered only by the incident light, with oxygen generated from the n-TiO₂ side of the diode and hydrogen from the p-Cu–Ti–O side. To date we find under global AM 1.5 illumination typical diodes of this design generate photocurrents of ≈ 0.25 mA/cm², with a photoconversion efficiency of 0.30%. The next step is to vary the material compositions to enable the use of a common aqueous electrolyte.

Self-aligned nanoporous iron(III) oxide was synthesized via potentiostatic anodization. Depending upon the anodization conditions, including potential and bath chemistry, the pores range from 50 to 250 nm in diameter, and 300–600 nm in length. The nanoporous films were annealed at 400 °C for 30 min to form crystalline hematite. The annealed nanoporous films demonstrated significant absorbance in the visible range, with a bandgap determined to be 2.2 eV. Under AM 1.5 illumination the photocurrent was measured to be 0.51 mA at 0.6 V vs Ag/AgCl in an electrolyte containing 1 M NaOH and 0.5 M H₂O₂. We also fabricated films comprised of vertically oriented Ti–Fe–O nanotube arrays on FTO coated glass substrates by anodic oxidation of Ti–Fe metal films in an ethylene glycol + NH₄F solvent. Annealing of the initially amorphous films resulted in some of the iron substituting for titanium ions in the titanium lattice, and the rest either forming α -Fe₂O₃ crystallites or remaining in the amorphous state. Low Fe content samples demonstrated anatase phase with annealing, moving to rutile phase as the Fe content in the samples increased. We obtain a photocurrent of 2 mA/cm² under AM 1.5, for iron oxide related materials a value second only to that recently reported by Gratzel of 2.2 mA/cm².¹²⁹ More importantly, should we be able to reduce the nanotube wall thickness to less than the minority carrier diffusion length, ≈ 2 –4 nm, we would expect dramatically improved photocurrents.

A large portion of this article is devoted to ternary oxide semiconducting nanotube arrays, which present one way to improve upon the properties of the basic TiO₂ nanotube array architecture. A second approach involves filling the nanotubes or conformally coating the nanotube walls with a low band gap semiconductor to form a heterojunction. In this regard, we also presented the fabrication and visible-spectrum properties of CdS-modified and CdTe-modified TiO₂ nanotube-array photoelectrodes. Sphere-like CdS nanoparticles, approximately 10 to 20 nm in diameter, were synthesized by electrodeposition from a nonaqueous solution. Longer electrodeposition times resulted in formation of larger CdS nanoparticle clumps, approximately 40–100 nm in diameter. The deposited CdS layer significantly extends the response of the TiO₂ nanotube-array electrodes into the visible region. Compared to a plain TiO₂ nanotube array electrode, photoelectrochemical measurements show that the visible light photocurrent increases by a factor of ≈ 16 with electrodeposition of the CdS layer. A heterojunction CdTe/TiO₂ photoelectrode was prepared by electrochemically filling tubes and tube-to-tube voids of n-type TiO₂ nanotube arrays with

p-type CdTe. Cathodic deposition of CdTe on TiO₂ nanotubes resulted in the formation of a three-dimensionally structured CdTe/TiO₂ junction with significantly enhanced junction areas. The presence of the CdTe/TiO₂ junction created three major differences compared to a CdTe layer directly deposited on FTO. First, while the CdTe layer deposited on FTO shows p-type behavior and generated a cathodic photocurrent, CdTe/TiO₂ electrodes generated an anodic photocurrent, indicating that the upward band bending created at the n-type TiO₂ and p-type CdTe junction prevails over the downward p-type CdTe and electrolyte junction. Second, the photocurrent generated by the CdTe/TiO₂ electrode is significantly higher than the two-dimensional CdTe layer deposited on FTO. This is because the CdTe layer deposited on TiO₂ nanotubes creates significantly higher CdTe/electrolyte junction areas. Third, while the photocurrent generated by the CdTe layer alone is unstable, the CdTe deposited on the TiO₂ tubes generated stable photocurrent. This indicates that photocorrosion in the CdTe layer can be kinetically suppressed by allowing for faster hole consumption at the CdTe/electrolyte junction and facile electron injection from the CdTe layer to the TiO₂ tubes.

We also successfully demonstrated the synthesis of densely packed single crystal TiO₂ nanowires on conductive glass substrates using a low temperature “nonpolar solvent/hydrophilic substrate” interface hydrolysis reaction. The synthesis method is simple, low cost and highly reproducible. The low temperature formation of oriented single crystalline TiO₂ nanowires on conductive glass presents a clear advance in technological capability. We have achieved this advance by employing completely new hydrothermal methods instead of the electrochemical techniques used to fabricate TiO₂ nanotube arrays. The promise of electron transport superhighways, and the resulting applications, appears at hand.

Considering the remarkable success of the 1-D material architecture in applications ranging from hydrogen gas sensing^{24,185} to solar cells^{4–6} to a drug eluting scaffold^{32–34} we believe the future holds considerable promise for the material architecture. Perhaps one of the most exciting new applications of the material architecture is in the photocatalytic reduction of CO₂ to hydrocarbon fuels using nitrogen doped nanotube arrays under outdoor sunlight, as depicted in Figure 58.¹⁸⁶ As reported by Varghese and co-workers,¹⁸⁶ efficient solar conversion of carbon dioxide and water vapor to methane and other hydrocarbons is achieved under outdoor sunlight (clear skies or sky with few clouds at University Park, Pennsylvania, latitude 40°49' W and longitude 77°51' N) using nitrogen doped titania nanotube arrays, with a wall thickness low enough to facilitate effective carrier transfer to the adsorbing species, surface-loaded with nano-dimensional islands of co-catalysts copper and/or platinum. Intermediate reaction products, hydrogen and carbon monoxide, are also detected with their relative concentrations underlying hydrocarbon production rates and dependent upon the nature of the co-catalysts on the nanotube array surface. Using outdoor global AM 1.5 sunlight (quantitative exposures were made for a duration of approximately 2.5 h, only when the sunlight power density was between about 102 and 75 mW/cm²), 100 mW/cm², from water vapor saturated CO₂ a hydrocarbon production rate of 111 ppm cm⁻² h⁻¹, or ≈ 160 μ L/g·h, is obtained when the nanotube array samples are loaded with both Cu and Pt nanoparticles. This rate of CO₂ to hydrocarbon production obtained under outdoor sunlight is at least 20 times higher than previous published reports, which were conducted under laboratory conditions using UV illumination. Considering all products, the total production rate (different hydrocarbons, hydrogen) using the co-catalyst sensitized nanotube array samples is about

273 ppm/(cm² h) indicating the great promise of this material architecture for photocatalytic CO₂ reduction.

Certainly there is great future promise in photoelectrochemical application of the nanotube arrays, in either the ternary oxide form or in combination with a low bandgap material to capture a significantly greater portion of the solar spectrum energy.

Acknowledgment. The authors gratefully acknowledge partial support of this work by the Department of Energy, Basic Energy Science, Grant No. DE-FG02-06ER15772.

References and Notes

- (1) deJongh, P. E.; Vanmaekelbergh, D. Trap-limited electronic transport in assemblies of nanometer-size TiO₂ particles. *Phys. Rev. Lett.* **1996**, *77*, 3427–3430.
- (2) Gong, D.; Grimes, C. A.; Varghese, O. K.; Hu, W. C.; Singh, R. S.; Chen, Z.; Dickey, E. C. Titanium oxide nanotube arrays prepared by anodic oxidation. *J. Mater. Res.* **2001**, *16*, 3331–3334.
- (3) Mor, G. K.; Shankar, K.; Paulose, M.; Varghese, O. K.; Grimes, C. A. Enhanced photocleavage of water using titania nanotube arrays. *Nano Lett.* **2005**, *5*, 191–195.
- (4) Zhu, K.; Neale, N. R.; Miedaner, A.; Frank, A. J. Enhanced charge-collection efficiencies and light scattering in dye-sensitized solar cells using oriented TiO₂ nanotubes arrays. *Nano Lett.* **2007**, *7*, 69–74.
- (5) Mor, G. K.; Shankar, K.; Paulose, M.; Varghese, O. K.; Grimes, C. A. Use of highly-ordered TiO₂ nanotube arrays in dye-sensitized solar cells. *Nano Lett.* **2006**, *6*, 215–218.
- (6) Shankar, K.; Bandara, J.; Paulose, M.; Wietasch, H.; Varghese, O. K.; Mor, G. K.; LaTempa, T. J.; Thelakkat, M.; Grimes, C. A. Highly Efficient Solar Cells using TiO₂ Nanotube Arrays Sensitized with a Donor-Antenna Dye. *Nano Lett.* **2008**, *8*, 1654–1659.
- (7) Shankar, K.; Mor, G. K.; Fitzgerald, A.; Grimes, C. A. Cation Effect on the Electrochemical Formation of Very High Aspect Ratio TiO₂ Nanotube Arrays in Formamide-Water Mixtures. *J. Phys. Chem. C* **2006**, *111*, 21–26.
- (8) Paulose, M.; Shankar, K.; Yoriya, S.; Prakasham, H. E.; Varghese, O. K.; Mor, G. K.; Latempa, T. A.; Fitzgerald, A.; Grimes, C. A. Anodic Growth of Highly Ordered TiO₂ Nanotube Arrays to 134 μm in Length. *J. Phys. Chem. B* **2006**, *110*, 16179–16184.
- (9) Prakasham, H. E.; Shankar, K.; Paulose, M.; Varghese, O. K.; Grimes, C. A. A new benchmark for TiO₂ nanotube array growth by anodization. *J. Phys. Chem. C* **2007**, *111*, 7235–7241.
- (10) Marin, F. I.; Hamstra, M. A.; Vanmaekelbergh, D. Greatly enhanced sub-bandgap photocurrent in porous GaP photoanodes. *J. Electrochem. Soc.* **1996**, *143*, 1137–1142.
- (11) Lutich, A. A.; Gaponenko, S. V.; Gaponenko, N. V.; Molchan, I. S.; Sokol, V. A.; Parkhutik, V. Anisotropic Light Scattering in Nanoporous Materials: A Photon Density of States Effect. *Nano Lett.* **2004**, *4*, 1755–1758.
- (12) Lazarouk, S.; Xie, Z. L.; Chigrinov, V.; Kwok, H. S. Anodic nanoporous titania for electro-optical devices. *Jpn. J. Appl. Phys. Part 1* **2007**, *46*, 4390–4394.
- (13) Likodimos, V.; Stergiopoulos, T.; Falaras, P.; Kunze, J.; Schmuki, P. Phase composition, size, orientation, and antenna effects of self-assembled anodized titania nanotube arrays: A polarized micro-Raman investigation. *J. Phys. Chem. C* **2008**, *112*, 12687–12696.
- (14) Shin, H. W.; Cho, S. Y.; Choi, K. H.; Oh, S. L.; Kim, Y. R. Directional random lasing in dye-TiO₂ doped polymer nanowire array embedded in porous alumina membrane. *Appl. Phys. Lett.* **2006**, *88*, 263112.
- (15) Zwilling, V.; Aucouturier, M.; Darque-Ceretti, E. Anodic oxidation of titanium and TA6V alloy in chromic media. An electrochemical approach. *Electrochim. Acta* **1999**, *45*, 921–929.
- (16) Wang, W. Z.; Varghese, O. K.; Paulose, M.; Grimes, C. A.; Wang, Q. L.; Dickey, E. C. A study on the growth and structure of titania nanotubes. *J. Mater. Res.* **2004**, *19*, 417–422.
- (17) Varghese, O. K.; Kichambre, P. D.; Gong, D.; Ong, K. G.; Dickey, E. C.; Grimes, C. A. Gas sensing characteristics of multi-wall carbon nanotubes. *Sens. Actuators B-Chem.* **2001**, *81*, 32–41.
- (18) Wang, W. Z.; Varghese, O. K.; Ruan, C. M.; Paulose, M.; Grimes, C. A. Synthesis of CuO and Cu₂O crystalline nanowires using Cu(OH)(2) nanowire templates. *J. Mater. Res.* **2003**, *18*, 2756–2759.
- (19) Prakasham, H. E.; Varghese, O. K.; Paulose, M.; Mor, G. K.; Grimes, C. A. Synthesis and photoelectrochemical properties of nanoporous iron (III) oxide by potentiostatic anodization. *Nanotechnology* **2006**, *17*, 4285–4291.
- (20) Mukherjee, N.; Paulose, M.; Varghese, O. K.; Mor, G. K.; Grimes, C. A. Fabrication of nanoporous tungsten oxide by galvanostatic anodization. *J. Mater. Res.* **2003**, *18*, 2296–2299.
- (21) Ong, K. G.; Varghese, O. K.; Mor, G. K.; Grimes, C. A. Numerical simulation of light propagation through highly-ordered titania nanotube arrays: Dimension optimization for improved photoabsorption. *J. Nanosci. Nanotechnol.* **2005**, *5*, 1801–1808.
- (22) Ong, K. G.; Varghese, O. K.; Mor, G. K.; Shankar, K.; Grimes, C. A. Application of finite-difference time domain to dye-sensitized solar cells: The effect of nanotube-array negative electrode dimensions on light absorption. *Solar Energy Mater. Solar Cells* **2007**, *91*, 250–257.
- (23) Varghese, O. K.; Gong, D. W.; Paulose, M.; Ong, K. G.; Dickey, E. C.; Grimes, C. A. Extreme changes in the electrical resistance of titania nanotubes with hydrogen exposure. *Adv. Mater.* **2003**, *15*, 624–627.
- (24) Paulose, M.; Varghese, O. K.; Mor, G. K.; Grimes, C. A.; Ong, K. G. Unprecedented ultra-high hydrogen gas sensitivity in undoped titania nanotubes. *Nanotechnology* **2006**, *17*, 398–402.
- (25) Varghese, O. K.; Gong, D. W.; Paulose, M.; Ong, K. G.; Grimes, C. A. Hydrogen sensing using titania nanotubes. *Sens. Actuators B-Chem.* **2003**, *93*, 338–344.
- (26) Shankar, K.; Mor, G. K.; Prakasham, H. E.; Varghese, O. K.; Grimes, C. A. Self-assembled hybrid polymer-TiO₂ nanotube array heterojunction solar cells. *Langmuir* **2007**, *23*, 12445–12449.
- (27) Shankar, K.; Mor, G. K.; Prakasham, H. E.; Yoriya, S.; Paulose, M.; Varghese, O. K.; Grimes, C. A. Highly-ordered TiO₂ nanotube arrays up to 220 μm in length: use in water photoelectrolysis and dye-sensitized solar cells. *Nanotechnology* **2007**, *18*, 065707.
- (28) Shankar, K.; Mor, G. K.; Paulose, M.; Varghese, O. K.; Grimes, C. A. Effect of device geometry on the performance of TiO₂ nanotube array-organic semiconductor double heterojunction solar cells. *J. Non-Cryst. Solids* **2008**, *354*, 2767–2771.
- (29) Mor, G. K.; Shankar, K.; Paulose, M.; Varghese, O. K.; Grimes, C. A. High efficiency double heterojunction polymer photovoltaic cells using highly ordered TiO₂ nanotube arrays. *Appl. Phys. Lett.* **2007**, *91*, 152111.
- (30) Varghese, O. K.; Paulose, M.; Shankar, K.; Mor, G. K.; Grimes, C. A. Water-photolysis properties of micron-length highly-ordered titania nanotube-arrays. *J. Nanosci. Nanotechnol.* **2005**, *5*, 1158–1165.
- (31) Mor, G. K.; Varghese, O. K.; Paulose, M.; Grimes, C. A. A self-cleaning, room-temperature titania-nanotube hydrogen gas sensor. *Sens. Lett.* **2003**, *1*, 42–46.
- (32) Popat, K. C.; Leoni, L.; Grimes, C. A.; Desai, T. A. Influence of engineered titania nanotubular surfaces on bone cells. *Biomaterials* **2007**, *28*, 3188–3197.
- (33) Popat, K. C.; Eltgroth, M.; LaTempa, T. J.; Grimes, C. A.; Desai, T. A. Decreased Staphylococcus epidermidis adhesion and increased osteoblast functionality on antibiotic-loaded titania nanotubes. *Biomaterials* **2007**, *28*, 4880–4888.
- (34) Popat, K. C.; Eltgroth, M.; LaTempa, T. J.; Grimes, C. A.; Desai, T. A. Titania nanotubes: A novel platform for drug-eluting coatings for medical implants. *Small* **2007**, *3*, 1878–1881.
- (35) Mor, G. K.; Varghese, O. K.; Paulose, M.; Shankar, K.; Grimes, C. A. A review on highly ordered, vertically oriented TiO₂ nanotube arrays: Fabrication, material properties, and solar energy applications. *Solar Energy Mater. Solar Cells* **2006**, *90*, 2011–2075.
- (36) Gratzel, M. Photoelectrochemical cells. *Nature* **2001**, *414*, 338–344.
- (37) Dvoranova, D.; Brezova, V.; Mazur, M.; Malati, M. A. Investigations of metal-doped titanium dioxide photocatalysts. *Appl. Catal. B-Environ.* **2002**, *37*, 91–105.
- (38) Umebayashi, T.; Yamaki, T.; Itoh, H.; Asai, K. Analysis of electronic structures of 3d transition metal-doped TiO₂ based on band calculations. *J. Phys. Chem. Solids* **2002**, *63*, 1909–1920.
- (39) Davydov, L.; Reddy, E. P.; France, P.; Smirniotis, P. G. Transition-metal-substituted titania-loaded MCM-41 as photocatalysts for the degradation of aqueous organics in visible light. *J. Catal.* **2001**, *203*, 157–167.
- (40) Wilke, K.; Breuer, H. D. The influence of transition metal doping on the physical and photocatalytic properties of titania. *J. Photochem. Photobiol. a-Chem.* **1999**, *121*, 49–53.
- (41) Wilke, K.; Breuer, H. D. Transition metal doped titania: Physical properties and photocatalytic behaviour. *Z. Phys. Chem.* **1999**, *213*, 135–140.
- (42) Asahi, R.; Morikawa, T.; Ohwaki, T.; Aoki, K.; Taga, Y. Visible-light photocatalysis in nitrogen-doped titanium oxides. *Science* **2001**, *293*, 269–271.
- (43) Burda, C.; Lou, Y. B.; Chen, X. B.; Samia, A. C. S.; Stout, J.; Gole, J. L. Enhanced nitrogen doping in TiO₂ nanoparticles. *Nano Lett.* **2003**, *3*, 1049–1051.
- (44) Ihara, T.; Miyoshi, M.; Iriyama, Y.; Matsumoto, O.; Sugihara, S. Visible-light-active titanium oxide photocatalyst realized by an oxygen-deficient structure and by nitrogen doping. *Appl. Catal. B-Environ.* **2003**, *42*, 403–409.
- (45) Sakthivel, S.; Kisch, H. Photocatalytic and photoelectrochemical properties of nitrogen-doped titanium dioxide. *ChemPhysChem* **2003**, *4*, 487–490.

- (46) Irie, H.; Watanabe, Y.; Hashimoto, K. Carbon-doped anatase TiO₂ powders as a visible-light sensitive photocatalyst. *Chem. Lett.* **2003**, 32, 772–773.
- (47) Park, J. H.; Kim, S.; Bard, A. J. Novel carbon-doped TiO₂ nanotube arrays with high aspect ratios for efficient solar water splitting. *Nano Lett.* **2006**, 6, 24–28.
- (48) Yamaki, T.; Umebayashi, T.; Sumita, T.; Yamamoto, S.; Maekawa, M.; Kawasuso, A.; Itoh, H. Fluorine-doping in titanium dioxide by ion implantation technique. *Nucl. Instrum. Methods Phys. Res. Sec. B* **2003**, 206, 254–258.
- (49) Sakthivel, S.; Janczarek, M.; Kisch, H. Visible light activity and photoelectrochemical properties of nitrogen-doped TiO₂. *J. Phys. Chem. B* **2004**, 108, 19384–19387.
- (50) Shankar, K.; Tep, K. C.; Mor, G. K.; Grimes, C. A. An electrochemical strategy to incorporate nitrogen in nanostructured TiO₂ thin films: modification of bandgap and photoelectrochemical properties. *J. Phys. D-Appl. Phys.* **2006**, 39, 2361–2366.
- (51) Wu, Z. B.; Dong, F.; Zhao, W. R.; Guo, S. Visible light induced electron transfer process over nitrogen doped TiO₂ nanocrystals prepared by oxidation of titanium nitride. *J. Hazard. Mater.* **2008**, 157, 57–63.
- (52) Lindgren, T.; Lu, J.; Hoel, A.; Granqvist, C. G.; Torres, G. R.; Lindquist, S. E. Photo electrochemical study of sputtered nitrogen-doped titanium dioxide thin films in aqueous electrolyte. *Solar Energy Mater. Solar Cells* **2004**, 84, 145–157.
- (53) Lindgren, T.; Mwabora, J. M.; Avendano, E.; Jonsson, J.; Hoel, A.; Granqvist, C. G.; Lindquist, S. E. Photoelectrochemical and optical properties of nitrogen doped titanium dioxide films prepared by reactive DC magnetron sputtering. *J. Phys. Chem. B* **2003**, 107, 5709–5716.
- (54) Diwald, O.; Thompson, T. L.; Goralski, E. G.; Walck, S. D.; Yates, J. T. The effect of nitrogen ion implantation on the photoactivity of TiO₂ rutile single crystals. *J. Phys. Chem. B* **2004**, 108, 52–57.
- (55) Nakamura, R.; Tanaka, T.; Nakato, Y. Mechanism for visible light responses in anodic photocurrents at N-doped TiO₂ film electrodes. *J. Phys. Chem. B* **2004**, 108, 10617–10620.
- (56) Torres, G. R.; Lindgren, T.; Lu, J.; Granqvist, C. G.; Lindquist, S. E. Photoelectrochemical study of nitrogen-doped titanium dioxide for water oxidation. *J. Phys. Chem. B* **2004**, 108, 5995–6003.
- (57) Murphy, A. B. Band-gap determination from diffuse reflectance measurements of semiconductor films, and application to photoelectrochemical water-splitting. *Solar Energy Mater. Solar Cells* **2007**, 91, 1326–1337.
- (58) Murphy, A. B. Does carbon doping of TiO₂ allow water splitting in visible light? Comments on “Nanotube enhanced photoresponse of carbon modified (CM)-n-TiO₂ for efficient water splitting”. *Solar Energy Mater. Solar Cells* **2008**, 92, 363–367.
- (59) DiValentin, C.; Pacchioni, G.; Selloni, A. Theory of Carbon Doping of Titanium Dioxide. *Chem. Mater.* **2005**, 17, 6656–6665.
- (60) Mrowetz, M.; Balcerski, W.; Colussi, A. J.; Hoffman, M. R. Oxidative power of nitrogen-doped TiO₂ photocatalysts under visible illumination. *J. Phys. Chem. B* **2004**, 108, 17269–17273.
- (61) Irie, H.; Watanabe, Y.; Hashimoto, K. Nitrogen-concentration dependence on photocatalytic activity of TiO_{2-x}N_x powders. *J. Phys. Chem. B* **2003**, 107, 5483–5486.
- (62) Batzill, M.; Morales, E. H.; Diebold, U. Influence of nitrogen doping on the defect formation and surface properties of TiO₂ rutile and anatase. *Phys. Rev. Lett.* **2006**, 96, 026103.
- (63) Serpone, N. Is the band gap of pristine TiO₂ narrowed by anion- and cation-doping of titanium dioxide in second-generation photocatalysts. *J. Phys. Chem. B* **2006**, 110, 24287–24293.
- (64) Bolton, J. R. Solar photoproduction of hydrogen: A review. *Solar Energy* **1996**, 57, 37–50.
- (65) Heller, A. Conversion of Sunlight into Electrical-Power and Photoassisted Electrolysis of Water in Photoelectrochemical Cells. *Acc. Chem. Res.* **1981**, 14, 154–162.
- (66) Varghese, O. K.; Grimes, C. A. Appropriate strategies for determining the photoconversion efficiency of water photo electrolysis cells: A review with examples using titania nanotube array photoanodes. *Solar Energy Mater. Solar Cells* **2008**, 92, 374–384.
- (67) Tomkiewicz, M.; Woodall, J. M. Photoelectrolysis of Water with Semiconductor-Materials. *J. Electrochem. Soc.* **1977**, 124, 1436–1440.
- (68) Nozik, A. J. Photoelectrolysis of Water Using Semiconducting TiO₂ Crystals. *Nature* **1975**, 257, 383–386.
- (69) Wrighton, M. S.; Ginley, D. S.; Wolczanski, P. T.; Ellis, A. B.; Morse, D. L.; Linz, A. Photoassisted Electrolysis of Water by Irradiation of a Titanium-Dioxide Electrode. *Proc. Natl. Acad. Sci. U.S.A.* **1975**, 72, 1518–1522.
- (70) Parkinson, B. On the Efficiency and Stability of Photoelectrochemical Devices. *Acc. Chem. Res.* **1984**, 17, 431–437.
- (71) Murphy, O. J.; Bockris, J. O. M. On the Efficiency of Conversion in Photo-Electrochemical Cells. *J. Electrochem. Soc.* **1982**, 129, C332–C332.
- (72) Fujishima, A.; Kohayakawa, K.; Honda, K. Hydrogen Production under Sunlight with an Electrochemical Photocell. *J. Electrochem. Soc.* **1975**, 122, 1487–1489.
- (73) Bard, A. J.; Faulkner, L. R., *Electrochemical Methods: Fundamentals & Applications*; Wiley: New York, 2001.
- (74) Murphy, A. B.; Barnes, P. R. F.; Randeniya, L. K.; Plumb, I. C.; Grey, I. E.; Horne, M. D.; Glasscock, J. A. Efficiency of solar water splitting using semiconductor electrodes. *Int. J. Hydrogen Energy* **2006**, 31, 1999–2017.
- (75) Khan, S. U. M.; Al-Shahry, M.; Ingler, W. B. Efficient photochemical water splitting by a chemically modified n-TiO₂. *Science* **2002**, 297, 2243–2245.
- (76) Ang, P. G. P.; Sammells, A. F. Hydrogen Evolution at P-InP Photocathodes in Alkaline Electrolyte. *J. Electrochem. Soc.* **1984**, 131, 1462–1464.
- (77) Dohrmann, J. K.; Schaaf, N. S. Energy-Conversion by Photoelectrolysis of Water - Determination of Efficiency by In-situ Photocalorimetry. *J. Phys. Chem.* **1992**, 96, 4558–4563.
- (78) Heller, A. Electrochemical Solar-Cells. *Solar Energy* **1982**, 29, 153–162.
- (79) Aroutiounian, V. M.; Arakelyan, V. M.; Shahnazaryan, G. E. Metal oxide photoelectrodes for hydrogen generation using solar radiation-driven water splitting. *Solar Energy* **2005**, 78, 581–592.
- (80) Fujishima, A. Comment on “Efficient photochemical water splitting by a chemically modified n-TiO₂” - (I). *Science* **2003**, 301, 1673A–1673A.
- (81) Hagglund, C.; Gratzel, M.; Kasemo, B. Comment on “Efficient photochemical water splitting by a chemically modified n-TiO₂” - (II). *Science* **2003**, 301, 1673B.
- (82) Lackner, K. S. Comment on “Efficient photochemical water splitting by a chemically modified n-TiO₂” - (III). *Science* **2003**, 301, 1673C–1673C.
- (83) Khan, S. U. M.; Al-Shahry, M.; Ingler, W. B. Response to comments on “Efficient photochemical water splitting by a chemically modified n-TiO₂”. *Science* **2003**, 301, 1673D.
- (84) Raja, K. S.; Mahajan, V. K.; Misra, M. Determination of photo conversion efficiency of nanotubular titanium oxide photo-electrochemical cell for solar hydrogen generation. *J. Power Sources* **2006**, 159, 1258–1265.
- (85) Heimer, T. A.; Heilweil, E. J.; Bignozzi, C. A.; Meyer, G. J. Electron injection, recombination, and halide oxidation dynamics at dye-sensitized metal oxide interfaces. *J. Phys. Chem. A* **2000**, 104, 4256–4262.
- (86) vandeLagemaat, J.; Plakman, M.; Vanmaekelbergh, D.; Kelly, J. J. Enhancement of the light-to-current conversion efficiency in an n-SiC/solution diode by porous etching. *Appl. Phys. Lett.* **1996**, 69, 2246–2248.
- (87) Lubberhuizen, W. H.; Vanmaekelbergh, D.; Van Faassen, E. Recombination of photogenerated charge carriers in nanoporous gallium phosphide. *J. Porous Mater.* **2000**, 7, 147–152.
- (88) Cai, Q. Y.; Paulose, M.; Varghese, O. K.; Grimes, C. A. The effect of electrolyte composition on the fabrication of self-organized titanium oxide nanotube arrays by anodic oxidation. *J. Mater. Res.* **2005**, 20, 230–236.
- (89) Varghese, O. K.; Gong, D. W.; Paulose, M.; Grimes, C. A.; Dickey, E. C. Crystallization and high-temperature structural stability of titanium oxide nanotube arrays. *J. Mater. Res.* **2003**, 18, 156–165.
- (90) Allam, N. K.; Shankar, K.; Grimes, C. A. A General Method for the Anodic Formation of Crystalline Metal Oxide Nanotube Arrays Without the use of Thermal Annealing. *Adv. Mater.* **2008**, 20, 3942–3946.
- (91) Kondo, J. N.; Domen, K. Crystallization of mesoporous metal oxides. *Chem. Mater.* **2008**, 20, 835–847.
- (92) Wang, X. X.; Hayakawa, S.; Tsuru, K.; Osaka, A. Improvement of bioactivity of H₂O₂/TaCl₅-treated titanium after subsequent heat treatments. *J. Biomed. Mater. Res.* **2000**, 52, 171–176.
- (93) Miao, Z.; Xu, D. S.; Ouyang, J. H.; Guo, G. L.; Zhao, X. S.; Tang, Y. Q. Electrochemically induced sol-gel preparation of single-crystalline TiO₂ nanowires. *Nano Lett.* **2002**, 2, 717–720.
- (94) Wu, J. M. Low-temperature preparation of titania nanorods through direct oxidation of titanium with hydrogen peroxide. *J. Cryst. Growth* **2004**, 269, 347–355.
- (95) Onoda, K.; Yoshikawa, S. Effect of pre-nitridation treatment on the formation of anatase TiO₂ films by anodization. *Ceram. Int.* **2008**, 34, 1453–1457.
- (96) Linsebigler, A. L.; Lu, G. Q.; Yates, J. T. Photocatalysis on TiO₂ Surfaces - Principles, Mechanisms, and Selected Results. *Chem. Rev.* **1995**, 95, 735–758.
- (97) Ghijsen, J.; Tjeng, L. H.; van Elp, J.; Eskes, H.; Westerink, J.; Sawatzky, G. A.; Czyzyk, M. T. Electronic structure of Cu₂O and CuO. *Phys. Rev. B* **1988**, 38, 11322.
- (98) Briskman, R. N. A Study of Electrodeposited Cuprous-Oxide Photovoltaic Cells. *Solar Energy Mater. Solar Cells* **1992**, 27, 361–368.
- (99) Musa, A. O.; Akomolafe, T.; Carter, M. J. Production of cuprous oxide, a solar cell material, by thermal oxidation and a study of its physical and electrical properties. *Solar Energy Mater. Solar Cells* **1998**, 51, 305–316.

- (100) Georgieva, V.; Ristov, M. Electrodeposited cuprous oxide on indium tin oxide for solar applications. *Solar Energy Mater. Solar Cells* **2002**, *73*, 67–73.
- (101) de Jongh, P. E.; Vanmaekelbergh, D.; Kelly, J. J. Cu₂O: a catalyst for the photochemical decomposition of water. *Chem. Commun.* **1999**, 1069–1070.
- (102) Hardee, K. L.; Bard, A. J. Semiconductor Electrodes 0.10. Photoelectrochemical Behavior of Several Polycrystalline Metal-Oxide Electrodes in Aqueous-Solutions. *J. Electrochem. Soc.* **1977**, *124*, 215–224.
- (103) Hara, M.; Kondo, T.; Komoda, M.; Ikeda, S.; Shinohara, K.; Tanaka, A.; Kondo, J. N.; Domen, K. Cu₂O as a photocatalyst for overall water splitting under visible light irradiation. *Chem. Commun.* **1998**, 357–358.
- (104) Papadimitriou, L.; Economou, N. A.; Trivich, D. Heterojunction Solar-Cells on Cuprous-Oxide. *Solar Cells* **1981**, *3*, 73–80.
- (105) Herion, J.; Niekisch, E. A.; Scharl, G. Investigation of Metal-Oxide Cuprous-Oxide Heterojunction Solar-Cells. *Solar Energy Mater.* **1980**, *4*, 101–112.
- (106) Siripala, W.; Ivanovskaya, A.; Jaramillo, T. F.; Baeck, S. H.; McFarland, E. W. A Cu₂O/TiO₂ heterojunction thin film cathode for photoelectrocatalysis. *Solar Energy Mater. Solar Cells* **2003**, *77*, 229–237.
- (107) Rakhshani, A. E. Preparation, Characteristics and Photovoltaic Properties of Cuprous-Oxide - a Review. *Solid-State Electron.* **1986**, *29*, 7–17.
- (108) Rai, B. P. Cu₂O Solar-Cells - a Review. *Solar Cells* **1988**, *25*, 265–272.
- (109) Liu, J.; Huang, X.; Li, Y.; Sulieman, K. M.; He, X.; Sun, F. Self-Assembled CuO Monocrystalline Nanoarchitectures with Controlled Dimensionality and Morphology. *Cryst. Growth Des.* **2006**, *6*, 1690–1696.
- (110) Oh, J.; Tak, Y.; Lee, Y. Electrodeposition of Cu₂O nanowires using nanoporous alumina template. *Electrochem. Solid State Lett.* **2004**, *7*, C27–C30.
- (111) Jiang, X. C.; Herricks, T.; Xia, Y. N. CuO nanowires can be synthesized by heating copper substrates in air. *Nano Lett.* **2002**, *2*, 1333–1338.
- (112) Koffyberg, F. P.; Benko, F. A. A Photo-Electrochemical Determination of the Position of the Conduction and Valence Band Edges of P-Type CuO. *J. Appl. Phys.* **1982**, *53*, 1173–1177.
- (113) Sumikura, S.; Mori, S.; Shimizu, S.; Usami, H.; Suzuki, E. Photoelectrochemical characteristics of cells with dyed and undyed nanoporous p-type semiconductor CuO electrodes. *J. Photochem. Photobiol. A-Chem.* **2008**, *194*, 143–147.
- (114) Mor, G. K.; Varghese, O. K.; Wilke, R. H. T.; Sharma, S.; Shankar, K.; Latempa, T. J.; Choi, K. S.; Grimes, C. A. p-type Cu-Ti-O nanotube arrays and their use in self-biased heterojunction photoelectrochemical diodes for hydrogen generation. *Nano Lett.* **2008**, *8*, 1906–1911.
- (115) Mor, G. K.; Varghese, O. K.; Paulose, M.; Grimes, C. A. Transparent highly ordered TiO₂ nanotube arrays via anodization of titanium thin films. *Adv. Funct. Mater.* **2005**, *15*, 1291–1296.
- (116) Tomkiewicz, M.; Fay, H. Photoelectrolysis of Water with Semiconductors. *Appl. Phys.* **1979**, *18*, 1–28.
- (117) Choi, H. J.; Kang, M. Hydrogen production from methanol/water decomposition in a liquid photosystem using the anatase structure of Cu loaded TiO₂. *Int. J. Hydrogen Energy* **2007**, *32*, 3841–3848.
- (118) Nozik, A. J. Photochemical Diodes. *Appl. Phys. Lett.* **1977**, *30*, 567–569.
- (119) Nozik, A. J.; Memming, R. Physical chemistry of semiconductor-liquid interfaces. *J. Phys. Chem.* **1996**, *100*, 13061–13078.
- (120) de Tacconi, N. R.; Chenthamarakshan, C. R.; Rajeshwar, K.; Tacconi, E. J. Selenium-modified titanium dioxide photochemical diode/electrolyte junctions: Photocatalytic and electrochemical preparation, characterization, and model simulations. *J. Phys. Chem. B* **2005**, *109*, 11953–11960.
- (121) Frank, A. J.; Honda, K. Oxygen and Hydrogen Generation from Water on Polymer-Protected CdS Photo-Anodes. *J. Electroanal. Chem.* **1983**, *150*, 673–678.
- (122) Frank, A. J.; Honda, K. Visible-Light Induced Water Cleavage and Stabilization of N-Type CdS to Photocorrosion with Surface Attached Polypyrrole Catalyst Coating. *J. Phys. Chem.* **1982**, *86*, 1933–1935.
- (123) Honda, K.; Frank, A. J. Polymer-Catalyst-Modified Cadmium-Sulfide Photochemical Diodes in the Photolysis of Water. *J. Phys. Chem.* **1984**, *88*, 5577–5582.
- (124) Bjorksten, U.; Moser, J.; Gratzel, M. Photoelectrochemical Studies on Nanocrystalline Hematite Films. *Chem. Mater.* **1994**, *6*, 858–863.
- (125) Morin, F. J. Electrical Properties of Alpha-Fe₂O₃. *Phys. Rev.* **1954**, *93*, 1195–1199.
- (126) Gardner, R. F. G.; Tanner, D. W.; Sweett, F. Electrical Properties of Alpha Ferric Oxide; Ferric Oxide of High Purity. *J. Phys. Chem. Solids* **1963**, *24*, 1183–1186.
- (127) Sato, N. *Electrochemistry at Metal and Semiconductor Electrodes*; Elsevier: Amsterdam, 1998.
- (128) Beermann, N.; Vayssieres, L.; Lindquist, S. E.; Hagfeldt, A. Photoelectrochemical studies of oriented nanorod thin films of hematite. *J. Electrochem. Soc.* **2000**, *147*, 2456–2461.
- (129) Duret, A.; Gratzel, M. Visible light-induced water oxidation on mesoscopic alpha-Fe₂O₃ films made by ultrasonic spray pyrolysis. *J. Phys. Chem. B* **2005**, *109*, 17184–17191.
- (130) Cesar, I.; Kay, A.; Martinez, J. A. G.; Gratzel, M. Translucent thin film Fe₂O₃ photoanodes for efficient water splitting by sunlight: Nanostructure-directing effect of Si-doping. *J. Am. Chem. Soc.* **2006**, *128*, 4582–4583.
- (131) Ingler, W. B.; Khan, S. U. M. A self-driven p/n-Fe₂O₃ tandem photoelectrochemical cell for water splitting. *Electrochem. Solid State Lett.* **2006**, *9*, G144–G146.
- (132) Mor, G. K.; Prakasam, H. E.; Varghese, O. K.; Shankar, K.; Grimes, C. A. Vertically oriented Ti-Fe-O nanotube array films: Toward a useful material architecture for solar spectrum water photoelectrolysis. *Nano Lett.* **2007**, *7*, 2356–2364.
- (133) Macak, J. M.; Tsuchiya, H.; Taveira, L.; Aldabergero, S.; Schmuki, P. Smooth anodic TiO₂ nanotubes. *Angew. Chem.-Int. Ed.* **2005**, *44*, 7463–7465.
- (134) Gong, D. W.; Yadavalli, V.; Paulose, M.; Pishko, M.; Grimes, C. A. Controlled molecular release using nanoporous alumina capsules. *Biomed. Microdevices* **2003**, *5*, 75–80.
- (135) Zong, B. Y.; Wu, Y. H.; Han, G. C.; Yang, B. J.; Luo, P.; Wang, L.; Qiu, J. J.; Li, K. B. Synthesis of iron oxide nanostructures by annealing electrodeposited Fe-based films. *Chem. Mater.* **2005**, *17*, 1515–1520.
- (136) Wen, X. G.; Wang, S. H.; Ding, Y.; Wang, Z. L.; Yang, S. H. Controlled growth of large-area, uniform, vertically aligned arrays of alpha-Fe₂O₃ nanobelts and nanowires. *J. Phys. Chem. B* **2005**, *109*, 215–220.
- (137) Santhanam, K. S. V.; Sharon, M. *Photoelectrochemical Solar Cells* Elsevier: Amsterdam, 1988.
- (138) Itoh, K.; Bockris, J. O. Stacked Thin-Film Photoelectrode Using Iron-Oxide. *J. Appl. Phys.* **1984**, *56*, 874–876.
- (139) Gennari, F. C.; Pasquevich, D. M. Kinetics of the anatase rutile transformation in TiO₂ in the presence of Fe₂O₃. *J. Mater. Sci.* **1998**, *33*, 1571–1578.
- (140) Kongkanand, A.; Tvrdy, K.; Takechi, K.; Kuno, M.; Kamat, P. V. Quantum Dot Solar Cells. Tuning Photoresponse through Size and Shape Control of CdSe-TiO₂ Architecture. *J. Am. Chem. Soc.* **2008**, *130*, 4007–4015.
- (141) Vogel, R.; Hoyer, P.; Weller, H. Quantum-Sized Pbs, Cds, Ag₂S, Sb₂S₃, and Bi₂S₃ Particles as Sensitizers for Various Nanoporous Wide-Bandgap Semiconductors. *J. Phys. Chem.* **1994**, *98*, 3183–3188.
- (142) Spurgeon, J. M.; Atwater, H. A.; Lewis, N. S. A Comparison Between the Behavior of Nanorod Array and Planar Cd(Se, Te) Photoelectrodes. *J. Phys. Chem. C* **2008**, *112*, 6186–6193.
- (143) Xie, Z. B.; Adams, S.; Blackwood, D. J.; Wang, J. The effects of anodization parameters on titania nanotube arrays and dye sensitized solar cells. *Nanotechnology* **2008**, *19*, 405701.
- (144) Kuang, D.; Brillet, J.; Chen, P.; Takata, M.; Uchida, S.; Miura, H.; Sumioka, K.; Zakeeruddin, S. M.; Gratzel, M. Application of highly ordered TiO₂ nanotube arrays in flexible dye-sensitized solar cells. *ACS Nano* **2008**, *2*, 1113–1116.
- (145) Zhu, K.; Vinzant, T. B.; Neale, N. R.; Frank, A. J. Removing structural disorder from oriented TiO₂ nanotube arrays: Reducing the dimensionality of transport and recombination in dye-sensitized solar cells. *Nano Lett.* **2007**, *7*, 3739–3746.
- (146) Ortuño-López, M. B.; Sotelo-Lerma, M.; Mendoza-Galván, A.; Ramírez-Bon, R. Optical band gap tuning and study of strain in CdS thin films. *Vacuum* **2004**, *76*, 181–184.
- (147) *Handbook of Photovoltaic Science and Engineering*; John Wiley & Sons: New York, 2003.
- (148) Aramoto, T.; Kumazawa, S.; Higuchi, H.; Arita, T.; Shibutani, S.; Nishio, T.; Nakajima, J.; Tsuji, M.; Hanafusa, A.; Hibino, T.; Omura, K.; Ohyama, H.; Murozono, M. 16.0% efficient thin-film CdS/CdTe solar cells. *Jpn. J. Appl. Phys. Part 1* **1997**, *36*, 6304–6305.
- (149) Britt, J.; Ferekides, C. Thin-Film CdS/CdTe Solar-Cell with 15.8-Percent Efficiency. *Appl. Phys. Lett.* **1993**, *62*, 2851–2852.
- (150) Tiefenbacher, S.; Pettenkofer, C.; Jaegermann, W. Ultrahigh vacuum preparation and characterization of TiO₂/CdTe interfaces: Electrical properties and implications for solar cells. *J. Appl. Phys.* **2002**, *91*, 1984–1987.
- (151) Ernst, K.; Belaidi, A.; Konenkamp, R. Solar cell with extremely thin absorber on highly structured substrate. *Semicond. Sci. Technol.* **2003**, *18*, 475–479.
- (152) Ernst, K.; Engelhardt, R.; Ellmer, K.; Kelch, C.; Muffler, H. J.; Lux-Steiner, M. C.; Konenkamp, R. Contacts to a solar cell with extremely thin CdTe absorber. *Thin Solid Films* **2001**, *387*, 26–28.
- (153) Ernst, K.; Sieber, I.; Neumann-Spallart, M.; Lux-Steiner, M. C.; Konenkamp, R. Characterization of II-VI compounds on porous substrates. *Thin Solid Films* **2000**, *361*, 213–217.
- (154) Chen, S. G.; Paulose, M.; Ruan, C.; Mor, G. K.; Varghese, O. K.; Kouzoudis, D.; Grimes, C. A. Electrochemically synthesized CdS nano-

particle-modified TiO₂ nanotube-array photoelectrodes: Preparation, characterization, and application to photoelectrochemical cells. *J. Photochem. Photobiol. A-Chem.* **2006**, *177*, 177–184.

(155) Lincot, D. Electrodeposition of semiconductors. *Thin Solid Films* **2005**, *487*, 40–48.

(156) *Handbook of Semiconductor Electrodeposition*; Marcek Dekker: New York, 1996.

(157) Sant, P. A.; Kamat, P. V. Interparticle electron transfer between size-quantized CdS and TiO₂ semiconductor nanoclusters. *Phys. Chem. Chem. Phys.* **2002**, *4*, 198–203.

(158) Henglein, A. Small-Particle Research - Physicochemical Properties of Extremely Small Colloidal Metal and Semiconductor Particles. *Chem. Rev.* **1989**, *89*, 1861–1873.

(159) Kokai, J.; Rakhshani, A. E. Photocurrent spectroscopy of solution-grown CdS films annealed in CdCl₂ vapour. *J. Phys. D-Appl. Phys.* **2004**, *37*, 1970–1975.

(160) Panicker, M. P. R.; Knaster, M.; Kroger, F. A. Cathodic Deposition of CdTe from Aqueous-Electrolytes. *J. Electrochem. Soc.* **1978**, *125*, 566–572.

(161) Duffy, N. W.; Peter, L. M.; Wang, R. L.; Lane, D. W.; Rogers, K. D. Electrodeposition and characterization of CdTe films for solar cell applications. *Electrochim. Acta* **2000**, *45*, 3355–3365.

(162) Lepiller, C.; Lincot, D. New facets of CdTe electrodeposition in acidic solutions with higher tellurium concentrations. *J. Electrochem. Soc.* **2004**, *151*, C348–C357.

(163) Guo, Y. P.; Deng, X. N. Electrodeposition of CdTe Thin-Films and Their Photoelectrochemical Behavior. *Solar Energy Mater. Solar Cells* **1993**, *29*, 115–122.

(164) Qi, B.; Kim, D. W.; Williamson, D. L.; Trefny, J. U. Effects of postdeposition heat-treatment on morphology and microstructure of CdTe grown by electrodeposition. *J. Electrochem. Soc.* **1996**, *143*, 517–523.

(165) Saraie, J.; Kitagawa, M.; Ishida, M.; Tanaka, T. Liquid-Phase Epitaxial-Growth of CdTe in CdTe-CdCl₂ System. *J. Cryst. Growth* **1978**, *43*, 13–16.

(166) Levi, D. H.; Moutinho, H. R.; Hasoon, F. S.; Keyes, B. M.; Ahrenkiel, R. K.; AlJassim, M.; Kazmerski, L. L.; Birkmire, R. W. Micro through nanostructure investigations of polycrystalline CdTe: Correlations with processing and electronic structures. *Solar Energy Mater. Solar Cells* **1996**, *41–2*, 381–393.

(167) Durose, K.; Edwards, P. R.; Halliday, D. P. Materials aspects of CdTe/CdS solar cells. *J. Cryst. Growth* **1999**, *197*, 733–742.

(168) Beach, J. D.; McCandless, B. E. Materials challenges for CdTe and CuInSe₂ photovoltaics. *MRS Bull.* **2007**, *32*, 225–229.

(169) Kampmann, A.; Lincot, D. Photoelectrochemical study of thin film semiconductor heterostructures: Junction formation processes in CdS vertical bar CdTe solar cells. *J. Electroanal. Chem.* **1996**, *418*, 73–81.

(170) Moutinho, H. R.; Al-Jassim, M. M.; Levi, D. H.; Dippo, P. C.; Kazmerski, L. L. Effects of CdCl₂ treatment on the recrystallization and electro-optical properties of CdTe thin films. *J. Vac. Sci. Technol. A* **1998**, *16*, 1251–1257.

(171) Seabold, J. A.; Shankar, K.; Wilke, R. H. T.; Paulose, M.; Varghese, O. K.; Grimes, C. A.; Choi, K.-S. Photoelectrochemical Properties of Heterojunction CdTe/TiO₂ Electrodes Constructed Using Highly Ordered TiO₂ Nanotube Arrays. *Chem. Mater.* **2008**, *20*, 5266–5273.

(172) Elsirafy, A. A.; Eldessouki, M. S.; Elbasiouny, M. S. CdTe Semiconductor Electrochemical-Behavior - Scope of Application as an Analytical Sensor. *J. Electrochem. Soc.* **1987**, *134*, 221–226.

(173) Baxter, J. B.; Aydil, E. S. Nanowire-based dye-sensitized solar cells. *Appl. Phys. Lett.* **2005**, *86*, 053114.

(174) Law, M.; Greene, L. E.; Johnson, J. C.; Saykally, R.; Yang, P. D. Nanowire dye-sensitized solar cells. *Nat. Mater.* **2005**, *4*, 455–459.

(175) Chen, X.; Mao, S. S. Titanium dioxide nanomaterials: Synthesis, properties, modifications, and applications. *Chem. Rev.* **2007**, *107*, 2891–2959.

(176) Cheng, H. M.; Ma, J. M.; Zhao, Z. G.; Qi, L. M. Hydrothermal Preparation of Uniform Nanosize Rutile and Anatase Particles. *Chem. Mater.* **1995**, *7*, 663–671.

(177) Zhang, Q. H.; Gao, L. Preparation of oxide nanocrystals with tunable morphologies by the moderate hydrothermal method: Insights from rutile TiO₂. *Langmuir* **2003**, *19*, 967–971.

(178) Cozzoli, P. D.; Kornowski, A.; Weller, H. Low-temperature synthesis of soluble and processable organic-capped anatase TiO₂ nanorods. *J. Am. Chem. Soc.* **2003**, *125*, 14539–14548.

(179) Adachi, M.; Murata, Y.; Takao, J.; Jiu, J. T.; Sakamoto, M.; Wang, F. M. Highly efficient dye-sensitized solar cells with a titania thin-film electrode composed of a network structure of single-crystal-like TiO₂ nanowires made by the “oriented attachment” mechanism. *J. Am. Chem. Soc.* **2004**, *126*, 14943–14949.

(180) Hosono, E.; Fujihara, S.; Kakiuchi, K.; Imai, H. Growth of submicrometer-scale rectangular parallelepiped rutile TiO₂ films in aqueous TiCl₃ solutions under hydrothermal conditions. *J. Am. Chem. Soc.* **2004**, *126*, 7790–7791.

(181) Feng, X. J.; Zhai, J.; Jiang, L. The fabrication and switchable superhydrophobicity of TiO₂ nanorod films. *Angew. Chem.-Int. Ed.* **2005**, *44*, 5115–5118.

(182) Hendry, E.; Koeberg, M.; O'Regan, B.; Bonn, M. Local field effects on electron transport in nanostructured TiO₂ revealed by terahertz spectroscopy. *Nano Lett.* **2006**, *6*, 755–759.

(183) Oliva, F. Y.; Avallé, L. B.; Santos, E.; Camara, O. R. Photoelectrochemical characterization of nanocrystalline TiO₂ films on titanium substrates. *J. Photochem. Photobiol. A-Chem.* **2002**, *146*, 175–188.

(184) Feng, X.; Shankar, K.; Varghese, O. K.; Paulose, M.; Latempa, T. J.; Grimes, C. A. Vertically Aligned Single-Crystal TiO₂ Nanowires: Synthesis and Applications. *Nano Lett.* **2008**, *8*, 3781–3786.

(185) Varghese, O. K.; Yang, X.; Kendig, J.; Paulose, M.; Zeng, K.; Palmer, C.; Ong, K. G.; Grimes, C. A. A Transcutaneous Hydrogen Sensor: From Design to Application. *Sensor Lett.* **2006**, *4*, 120–128.

(186) Varghese, O. K.; Paulose, M.; LaTempa, T. J.; Grimes, C. A. High-Rate Solar Photocatalytic Conversion of CO₂ and Water Vapor to Hydrocarbon Fuels. *Nano Lett.* **2009**, *9*, 731–737.

JP809385X